Electron– and positron–molecule scattering: development of the molecular convergent close-coupling method

2017 J. Phys. B: At. Mol. Opt. Phys. 50 123001

(http://iopscience.iop.org/0953-4075/50/12/123001)

IOP Publishing Journal of Physics B: Atomic, Molecular and Optical Physics
J. Phys. B: At. Mol. Opt. Phys. **50** (2017) 123001 (35pp) https://doi.org/10.1088/1361-6455/aa6e74

Tutorial

Electron– and positron–molecule scattering: development of the molecular convergent close-coupling method

Mark C Zammit[1,2], Dmitry V Fursa[2], Jeremy S Savage[2] and Igor Bray[2]

[1] Theoretical Division, Los Alamos National Laboratory, Los Alamos, NM 87545, United States of America
[2] Curtin Institute for Computation and Department of Physics, Astronomy and Medical Radiation Sciences, Curtin University, Perth, Western Australia 6102, Australia

E-mail: mzammit@lanl.gov

Received 25 January 2016, revised 29 March 2017
Accepted for publication 21 April 2017
Published 22 May 2017

Abstract

Starting from first principles, this tutorial describes the development of the adiabatic-nuclei convergent close-coupling (CCC) method and its application to electron and (single-centre) positron scattering from diatomic molecules. We give full details of the single-centre expansion CCC method, namely the formulation of the molecular target structure; solving the momentum-space coupled-channel Lippmann–Schwinger equation; deriving adiabatic-nuclei cross sections and calculating *V*-matrix elements. Selected results are presented for electron and positron scattering from molecular hydrogen H_2 and electron scattering from the vibrationally excited molecular hydrogen ion H_2^+ and its isotopologues (D_2^+, T_2^+, HD^+, HT^+ and TD^+). Convergence in both the close-coupling (target state) and projectile partial-wave expansions of fixed-nuclei electron– and positron–molecule scattering calculations is demonstrated over a broad energy-range and discussed in detail. In general, the CCC results are in good agreement with experiments.

Keywords: electron scattering, positron scattering, excitation, ionisation, molecular hydrogen

(Some figures may appear in colour only in the online journal)

1. Introduction

Chemical reactions are the underlying processes that govern medicine, industry, nature and life. The very foundation of chemistry is the individual collisions between photons, electrons, ions, atoms and molecules. By studying particular scattering processes, resulting collision data can be used to determine the collective many body-effects of a media. Calculations of ion stage abundance, energy deposition/transport and reactivity are just some of the properties that are required to advance science and technology. Examples that rely on electron or positron collision data include electric lighting, fusion technology [1–4], materials research [5], climate science [6], astrophysics [7–9], lasers, radiotherapy [10–16] and positron emission tomography scans to detect cancers and mental diseases [16, 17].

Although collision physics is of technological and scientific interest, there are currently no accurate, efficient, and comprehensive scattering models readily available. Theoretical models, however, are seen as the most likely route to providing the detailed and comprehensive collision data sets required, while experiments provide sensitive tests of theory.

1.1. Molecular scattering processes

Theoretical formulations of electron and positron collisions with molecules are often based on techniques developed for electron–atom scattering. Molecules, however, have the complexity

of multi-centre potentials which leads to absence of spherical symmetry. In addition the rotational and vibrational degrees of freedom add to the complexity of scattering processes. *Ab initio* theoretical treatments of positron scattering are even more difficult than electron scattering. This is due to the strong electron–positron correlations and the additional channel of positronium (Ps) formation. In approximate order of lowest threshold energy, some of the important electron/positron–molecule/molecular–ion scattering processes include:

elastic scattering

$$e^{\pm} + AB(n, v, J) \rightarrow e^{\pm} + AB(n, v, J), \quad (1)$$

dissociative recombination (of molecular ions)

$$e^{-} + AB^{+}(n, v, J) \rightarrow AB^{**} \rightarrow A + B, \quad (2)$$

rotational excitation

$$e^{\pm} + AB(n, v, J) \rightarrow e^{\pm} + AB(n, v, J'), \quad (3)$$

vibrational excitation

$$e^{\pm} + AB(n, v, J) \rightarrow e^{\pm} + AB(n, v', J'), \quad (4)$$

resonant dissociative excitation (DE) (of molecular ions)

$$e^{-} + AB^{+}(n, v, J) \rightarrow AB^{**} \rightarrow e^{-} + A^{+} + B, \quad (5)$$

$$\rightarrow e^{-} + A + B^{+}, \quad (6)$$

dissociative attachment

$$e^{-} + AB(n, v, J) \rightarrow A^{-} + B, \quad (7)$$

$$\rightarrow A + B^{-}, \quad (8)$$

positronium (Ps) formation

$$e^{+} + AB(n, v, J) \rightarrow Ps + AB^{+}, \quad (9)$$

electronic excitation

$$e^{\pm} + AB(n, v, J) \rightarrow e^{\pm} + AB(n', v', J'), \quad (10)$$

dissociation (usually by electronic excitation)

$$e^{\pm} + AB(n, v, J) \rightarrow e^{\pm} + AB^{*} \rightarrow e^{\pm} + A + B, \quad (11)$$

DE (of molecular ions)

$$e^{\pm} + AB^{+}(n, v, J) \rightarrow e^{\pm} + AB^{+*} \rightarrow e^{\pm} + A^{+} + B, \quad (12)$$

$$\rightarrow e^{\pm} + A + B^{+}, \quad (13)$$

single-ionisation

$$e^{\pm} + AB(n, v, J) \rightarrow e^{\pm} + e^{-} + AB^{+}, \quad (14)$$

dissociative ionisation (DI) (of neutral and ionic molecules)

$$e^{\pm} + AB(n, v, J) \rightarrow e^{\pm} + e^{-} + A^{+} + B, \quad (15)$$

$$\rightarrow e^{\pm} + e^{-} + A + B^{+}, \quad (16)$$

$$e^{\pm} + AB^{+}(n, v, J) \rightarrow e^{\pm} + e^{-} + A^{+} + B^{+}, \quad (17)$$

Here n, v, J are the molecule's electronic, vibrational and rotational state respectively, and v' and J' in (4) and (10) indicate that these processes can also lead to simultaneous rotational and vibrational excitation. AB^{*} indicates an excited state of AB and AB^{**} is either a doubly excited or autoionising Rydberg state of AB with the respective dissociative asymptotic conditions. In some cases resonances drive rotational excitations (3), vibrational excitations (4), rearrangement processes (2), (7) and (8) and dissociation processes (5), (6) and (11) [18–20].

1.2. Overview of theoretical methods

Theoretical methods for electron and positron scattering from atoms and molecules can be classified into two categories: perturbative and non-perturbative. Perturbative methods are generally only accurate in the high-energy region (impact-energy higher than ten times ionisation threshold). Some of the most actively used quantum mechanical perturbative methods include the distorted-wave Born approximation [21, 22] and the independent-atom model screening-corrected additivity rule [23–25]. General scaling laws of the first-order plane-wave Born results for neutral atoms and molecules remarkably produces accurate dipole-allowed excitation and ionisation cross sections from a few eV above threshold to high energies [26–28]. For ions a similar scaling law has been applied to the Coulomb Born cross sections with equivalent success [28–30]. Here however, we are only interested in non-perturbative methods, which in principle are applicable for all transitions and at all energies.

Non-perturbative methods are based on solving the Schrödinger equation using either grid based techniques or a close-coupling expansion. In principle non-perturbative methods can calculate accurate results across the entire energy region. The low-energy region (from 0 eV to ionisation threshold) for molecules is the most difficult to describe, where coupling projectile, electronic, and nuclei motion can be important in order to describe the rotational, vibrational, electronic, dissociative and rearrangement scattering processes. To date completely *ab initio* electronic-rovibrational close-coupling calculations have not been performed. This method would be complicated to implement and calculations would require immense computing resources. Rotational [31], vibrational [32] and rovibrational [33] close-coupling methods have been applied to a range of molecules by utilising phenomenological potentials. These methods solve the nuclei close-coupling problem and can only calculate accurate results for nuclei excitations (not rearrangement or electronic excitations) in the low-energy region. The different types of scattering formulations to treat projectile, electronic, and nuclei motion are summarised in [31, 34, 35] and references therein. The multi-channel quantum defect theory [36] is the only *ab initio* method (utilising several approximations) that describes and can extract results of all processes (including rearrangement) in the low-energy region. This method however is limited to molecular ions and utilises several scattering formulations (that depend on the projectile and nuclei scattering region).

Here we limit ourselves to the discussion of the adiabatic-nuclei formulation (also known as the adiabatic-nuclei vibration approximation), which in principle can be utilised to calculate a comprehensive set of cross sections (elastic scattering, rotational, vibrational, and electronic excitations, ionisation, resonance and dissociative processes) [32, 35, 37, 38]. This formulation relies

on the Born–Oppenheimer approximation of the total scattering wave function and is based on the body-frame fixed-nuclei formulation, which fixes the internuclear separation R and orientation of the molecule $\hat{\boldsymbol{R}}$ throughout the collision. It is currently the most actively utilised electron– and positron–molecule scattering formulation. Non-perturbative methods that rely on the adiabatic-nuclei formulation include the Schwinger multichannel (SMC) [39], Kohn variational [40], R-matrix (RM) [20], molecular RM with pseudostates (RMPS) [20], time-dependent close-coupling (TDCC) [41] and molecular convergent close-coupling (CCC) [42] methods. With this formulation these methods essentially solve the fixed-nuclei (electronic motion) Schrödinger equation as opposed to the nuclei close-coupling methods mentioned above. The adiabatic-nuclei (and fixed-nuclei) approximation greatly reduce the complexity and computational resources required to solve the scattering problem and will be discussed further in section 2. The SMC, Kohn variational, RM, RMPS and molecular CCC methods utilise a fixed-nuclei close-coupling expansion to solve the scattering equations, while the TDCC method solves the fixed-nuclei time-dependent Schrödinger equation using a grid based technique. In principle these methods should all yield the same results if a convergent scattering and target model is utilised in the calculations. In the low-energy region these methods have had considerable success calculating elastic scattering within the fixed-nuclei approximation. However, only in some cases the rotational, vibrational, and electronic excitation cross sections have been accurately calculated.

The situation is very different in the intermediate-energy region (from ionisation threshold to ten times ionisation threshold), where elastic scattering, electronic excitation, and ionisation processes are dominant. The close-coupling approximation was originally developed as a low-energy approximation, which expanded the total scattering wave function over the set of bound target states. In the past few decades the target continuum has been included in the expansion via the use of positive energy pseudostates (obtained from diagonalisation of the target), which provide a discretised representation of the target continuum. This technique allowed the close-coupling method to be generalised to describe the entire projectile energy range. In these calculations total ionisation cross sections (TICSs) are calculated by summing discrete excitation cross sections of positive energy pseudostates.

Our experience from electron–atom scattering shows us that inter-channel coupling between the discrete spectrum and continuum is essential in order to obtain converged elastic, excitation and ionisation cross sections [43, 44]. Within the close-coupling approach these can be achieved by using a near-complete expansion of both the discrete and continuum spectrum of the target. In addition to treating the scattering dynamics accurately, one must have sufficiently accurate target states in order to obtain accurate cross sections. For example the complete account of polarisation effects in the scattering calculations predetermines the accuracy of the elastic scattering cross section, while the optical oscillator strength of a dipole-allowed transition predetermines its high energy cross section. The accuracy of the target states can be checked by calculating the target state energy, and optical oscillator strengths in both the length and velocity gauges. However, convergence in the scattering cross sections can be obtained with inaccurate target states. Hence performing scattering calculations with different target models allows one to estimate the underlying uncertainty in the cross sections with respect to the accuracy of the target states [45].

Even in the fixed-nuclei approximation, accurate close-coupling calculations are very large and computationally expensive. This is primarily due to the lack of spherical symmetry in the scattering system, where scattering equations need to couple all partial waves of orbital angular momentum (however, for homonuclear diatomic molecules total parity is conserved). This has limited the progress of non-perturbative methods. To date the SMC method has not calculated ionisation cross sections but it has been capable of calculating electronic excitation cross sections in the intermediate-energy region by utilising the projection operator approach [46, 47]. However our studies of electron– and positron–H_2 scattering [48–50] indicate that these calculations are not convergent with respect to the number of target states included in the calculations. The RMPS method has calculated TICSs just above threshold for several targets [51–53], however in some cases (electron scattering from H_2 and H_3^+) these calculations were severely affected by pseudoresonances [53]. For electron–H_2 scattering, our calculations [48] indicate that the RMPS and RM excitation cross sections exhibit pseudoresonance behaviour due to a lack of convergence. The CCC and TDCC methods are currently the only non-perturbative methods suited for accurately calculating TICSs across the entire intermediate-energy region. However, the TDCC method (a one-electron target model) has not calculated excitation cross sections for molecular targets thus far, as calculations are computationally too expensive.

The molecular CCC method is based on the atomic CCC method, which for the interested reader was extensively reviewed in [43, 44, 54, 55]. The present tutorial is organised as follows: section 2 describes the fundamental concepts of electron–molecule scattering, the connection between body- and laboratory-frames of reference and the Born–Oppenheimer and adiabatic-nuclei approximations. Section 3 details the formulation of the molecular target states for H_2^+ and H_2 within the Born–Oppenheimer approximation. Sections 4 and 5 describe in detail the molecular CCC method and the orientationally averaged analytic Born subtraction (ABS) method, respectively. In section 6 convergence studies are discussed and convergence is demonstrated for the CCC fixed-nuclei calculations of electron–H_2^+ scattering. Sections 7 and 8 present the application of the adiabatic-nuclei CCC method to electron scattering from vibrationally excited H_2^+ and its isotopologues (D_2^+, T_2^+, HD^+, HT^+ and DT^+), and positron scattering from vibrationally excited H_2. In section 9 the fixed-nuclei CCC results are presented for electron scattering from H_2, and finally in section 10, the tutorial and results of the molecular CCC method's application to electron and positron scattering from H_2, H_2^+ and its isotopologues are summarised, and the future research directions of this project

is also outlined. In the appendices, the orientationally averaged differential and integrated cross sections are derived, analytic properties of the Laguerre basis functions are given, and V-matrix elements of electron/positron scattering from H_2^+ and electron/positron scattering from H_2 are presented.

2. General theory

In this tutorial a non-relativistic scattering approach is used to derive the adiabatic-nuclei molecular CCC method. The formulation here is time-independent and assumes an electron or positron projectile. We do not describe rearrangement processes e.g. resonant DE (of molecular ions), dissociative attachment, recombination and explicit Ps formation. All equations are in atomic units and for the brevity of notation we have dropped the dependence of the nuclei spin, unless explicitly stated otherwise.

The objective of scattering theory is to calculate scattering observables (i.e. cross sections). The spin-resolved differential cross section (DCS) for a transition $i \to f$ has the form

$$\frac{\mathrm{d}\sigma^{\mathcal{S}}_{f,i}}{\mathrm{d}\Omega} = \frac{q_f}{q_i}\,|F^{\mathcal{S}}_{f,i}(\boldsymbol{q}_f, \boldsymbol{q}_i)|^2, \tag{18}$$

where $\mathcal{S}$ is the total electronic spin of the system, $\boldsymbol{q}$ is the projectile linear momentum vector, $F^{\mathcal{S}}_{f,i}(\boldsymbol{q}_f, \boldsymbol{q}_i)$ is the scattering amplitude, which has the general form

$$\begin{aligned} F^{\mathcal{S}}_{f,i}(\boldsymbol{q}_f, \boldsymbol{q}_i) &= -(2\pi)^2 \langle \boldsymbol{q}_f^{(-)} \bar{\Phi}_f | V | \bar{\Psi}_i^{\mathcal{S}(+)} \rangle \\ &= -(2\pi)^2 \langle \boldsymbol{q}_f^{(-)} \bar{\Phi}_f | T^{\mathcal{S}} | \bar{\Phi}_i \boldsymbol{q}_i^{(+)} \rangle, \end{aligned} \tag{19}$$

and $|\boldsymbol{q}^{(\pm)}\rangle$ represents the momentum space normalised projectile plane-wave (for a neutral target) or Coulomb-wave (for an ionic target). Here the incoming and outgoing spherical-wave boundary conditions are denoted by superscripts $^{(-)}$ and $^{(+)}$ respectively and V is the sum of all interaction potentials between the projectile and the target. $\bar{\Psi}_i^{\mathcal{S}(+)}(\mathbf{x}_0, \mathbf{x}, \boldsymbol{R})$ is the total scattering wave function and $\bar{\Phi}_n(\mathbf{x}, \boldsymbol{R})$ are the molecular states, where $\mathbf{x}_0$ and $\mathbf{x}$ represent the spatial and spin coordinates of the projectile and all target electrons respectively, and the vector $\boldsymbol{R}$ represents the spatial coordinates of the nuclei. We use the 'bar' notation to indicate variables which combine nuclear and electronic motion. It will be removed when they are decoupled. The (electronic) spin-averaged DCS (and similarly for the integrated cross section) is given by

$$\frac{\mathrm{d}\sigma_{f,i}}{\mathrm{d}\Omega} = \sum_{\mathcal{S}} \frac{2\mathcal{S}+1}{2(2s_i+1)} \frac{\mathrm{d}\sigma^{\mathcal{S}}_{f,i}}{\mathrm{d}\Omega}, \tag{20}$$

where s_i is the initial spin of the electronic target state.

The goal of theory is to solve for $F^{\mathcal{S}}_{f,i}(\boldsymbol{q}_f, \boldsymbol{q}_i)$ and $\bar{\Psi}_i^{\mathcal{S}(+)}(\mathbf{x}_0, \mathbf{x}, \boldsymbol{R})$. Different theoretical methods reflect different approaches used to solve the scattering system Schrödinger equation

$$(E^{(+)} - H)|\bar{\Psi}_i^{\mathcal{S}(+)}\rangle = 0, \tag{21}$$

where E and H are the total energy and Hamiltonian of the scattering system. For a projectile with charge z_0 ($z_0 = -1$ for the charge of an electron or $z_0 = 1$ for the charge of a positron), the non-relativistic Hamiltonian H is defined as

$$\begin{aligned} H = &-\frac{1}{2}\sum_{i=0}^{N_\mathrm{e}} \nabla_i^2 + \sum_{i=0}^{N_\mathrm{e}}\sum_{j=1}^{N_\mathrm{n}} \frac{z_i Z_j}{|\boldsymbol{r}_i - \boldsymbol{R}_j|} + \sum_{j>i=0}^{N_\mathrm{e}} \frac{z_i z_j}{|\boldsymbol{r}_i - \boldsymbol{r}_j|} \\ &- \sum_{i=1}^{N_\mathrm{n}} \frac{1}{2M_i} \nabla_i^2 + \sum_{j>i=1}^{N_\mathrm{n}} \frac{Z_i Z_j}{|\boldsymbol{R}_i - \boldsymbol{R}_j|}, \end{aligned} \tag{22}$$

where the target molecule has N_e electrons (with charge $z_i = -1$, for $i \geqslant 1$), N_n nuclei with charge Z and mass M. The vector $\boldsymbol{r}$ represents the spatial coordinates of the projectile/target electrons. Further details of the molecular Hamiltonian and its transformations are given in [56, 57].

The total scattering wave function with the correct outgoing boundary conditions can be expressed via a close-coupling expansion, which expands $\bar{\Psi}_i^{\mathcal{S}(+)}(\mathbf{x}_0, \mathbf{x}, \boldsymbol{R})$ in terms of all asymptotic channels. For electron scattering the close-coupling expansion has the form

$$\bar{\Psi}_i^{\mathcal{S}(+)}(\mathbf{x}_0, \mathbf{x}, \boldsymbol{R}) = \mathcal{A} \sum_n f_{n,i}^{\mathcal{S}(+)}(\mathbf{x}_0) \bar{\Phi}_n(\mathbf{x}, \boldsymbol{R}), \tag{23}$$

where $\mathcal{A}$ is the antisymmetrisation operator

$$\mathcal{A} = 1 - \sum_{i=1}^{N_\mathrm{e}} P_{0i}, \tag{24}$$

P_{0i} is the space and spin exchange operator, $f_{n,i}^{\mathcal{S}(+)}(\mathbf{x}_0)$ is the multichannel function and for positron scattering $\mathcal{A}$ is not required, i.e. $\mathcal{A} = 1$ in equation (23).

As mentioned above in section 1.2, even for the simplest diatomic molecule H_2^+ a complete electronic-rovibrational close-coupling calculation (23) is currently computationally unfeasible. This is primarily due to the large number of energetically finely spaced rotational and vibrational states, and an inability to treat very large scattering calculations in an efficient and numerically stable way. As summarised in [31, 34, 35], several methods have been applied to reduce the computational resources required to solve the electron–molecule scattering problem. One commonly used approach to reduce the size of the computation is to apply the Born–Oppenheimer approximation to the total scattering wave function [34, 35]. This approach is utilised by electronic close-coupling methods.

2.1. Born–Oppenheimer approximation

In the non-relativistic approximation molecular states $\bar{\Phi}_n(\mathbf{x}, \boldsymbol{R}) \equiv \bar{\Phi}_{nvJm_J}(\mathbf{x}, \boldsymbol{R})$ used in the close-coupling expansion (23) are characterised by their electronic state n, vibrational quantum number v, rotational quantum number J and rotational angular projection m_J.

The Born–Oppenheimer approximation (ansatz)

$$\bar{\Phi}_{nvJm_J}(\mathbf{x}, \boldsymbol{R}) \approx \Phi_n(\mathbf{x}; \boldsymbol{R}) \Xi_{nvJm_J}(\boldsymbol{R}), \tag{25}$$

separates the electronic $\boldsymbol{r}$ and nuclear $\boldsymbol{R}$ coordinates so that the electronic wave functions $\Phi_n(\mathbf{x}; \boldsymbol{R})$ depends parametrically on $\boldsymbol{R}$. The nuclear wave function $\Xi_{nvJm_J}(\boldsymbol{R})$ can also be written as a product of the vibrational $\nu_{nvJ}(R)$ and

rotational $R_{nJm_J}(\hat{\boldsymbol{R}})$ wave functions

$$\Xi_{n\nu Jm_J}(\boldsymbol{R}) = \nu_{n\nu J}(R) R_{nJm_J}(\hat{\boldsymbol{R}}). \tag{26}$$

In the Born–Oppenheimer approximation the electronic and nuclei motion are not coupled. The Born–Oppenheimer approximation (25) relies on the property that in a molecule the electrons are very light compared to the heavy nuclei and are moving much more rapidly, hence the nuclei respond to the average distribution of the electron density. See [56] for the details of including the electron–nuclei coupling (non-adiabatic method) and approximating the electron–nuclei coupling (adiabatic approximation).

2.2. Adiabatic-nuclei approximation

From a classical point of view if the collision time t_c is much less than the molecule's vibrational period τ_v ($\approx 10^{-14}$ s) and rotational period τ_R ($> \approx 10^{-12}$ s) [35], the total scattering wave function should be well represented within the Born–Oppenheimer approximation

$$\bar{\Psi}_i^{\mathcal{S}(+)}(\mathbf{x}_0, \mathbf{x}, \boldsymbol{R}) \approx \Psi_i^{\mathcal{S}(+)}(\mathbf{x}_0, \mathbf{x}; \boldsymbol{R}) \Xi_{i\nu_i J_i m_{J_i}}(\boldsymbol{R}). \tag{27}$$

In this approximation the projectile and target electrons do not couple with the nuclei motion and hence the nuclei are fixed at a chosen distance R and orientation $\hat{\boldsymbol{R}}$ throughout the collision.

Substituting Born–Oppenheimer molecular states (25) and $\bar{\Psi}_i^{\mathcal{S}(+)}(\mathbf{x}_0, \mathbf{x}, \boldsymbol{R})$ equation (27) into the scattering amplitude (19), we obtain the adiabatic-nuclei scattering amplitude for a transition $i\nu_i J_i m_{J_i} \rightarrow f\nu_f J_f m_{J_f}$

$$\begin{aligned} &F^{\mathcal{S}}_{f\nu_f J_f m_{J_f}, i\nu_i J_i m_{J_i}}(\boldsymbol{q}_f, \boldsymbol{q}_i) \\ &\quad = -(2\pi)^2 \langle \boldsymbol{q}_f^{(-)} \Xi_{f\nu_f J_f m_{J_f}} \Phi_f | V | \Psi_i^{\mathcal{S}(+)} \Xi_{i\nu_i J_i m_{J_i}} \rangle \\ &\quad = -(2\pi)^2 \langle \nu_{f\nu_f J_f} R_{fJ_f m_{J_f}} | T^{\mathcal{S}}_{f,i}(\boldsymbol{q}_f, \boldsymbol{q}_i; \boldsymbol{R}) | R_{iJ_i m_{J_i}} \nu_{i\nu_i J_i} \rangle, \end{aligned} \tag{28}$$

where the fixed-nuclei T-matrix $T^{\mathcal{S}}_{f,i}(\boldsymbol{q}_f, \boldsymbol{q}_i; \boldsymbol{R})$

$$T^{\mathcal{S}}_{f,i}(\boldsymbol{q}_f, \boldsymbol{q}_i; \boldsymbol{R}) = \langle \boldsymbol{q}_f^{(-)} \Phi_f | V | \Psi_i^{\mathcal{S}(+)} \rangle \equiv \langle \boldsymbol{q}_f^{(-)} \Phi_f | T^{\mathcal{S}} | \Phi_i \boldsymbol{q}_i^{(+)} \rangle. \tag{29}$$

Similarly to the close-coupling expansion of $\bar{\Psi}_i^{\mathcal{S}(+)}(\mathbf{x}_0, \mathbf{x}, \boldsymbol{R})$ in equation (23), the fixed-nuclei total scattering wave function $\Psi_i^{\mathcal{S}(+)}(\mathbf{x}_0, \mathbf{x}; \boldsymbol{R})$ can be expressed as an expansion over the electronic target states only

$$\Psi_i^{\mathcal{S}(+)}(\mathbf{x}_0, \mathbf{x}; \boldsymbol{R}) = \mathcal{A} \sum_n f^{\mathcal{S}(+)}_{n,i}(\mathbf{x}_0; \boldsymbol{R}) \Phi_n(\mathbf{x}; \boldsymbol{R}), \tag{30}$$

where it is important to note that in this approach only electronic states (and motion) are coupled and for positron scattering $\mathcal{A}$ is not required, i.e. $\mathcal{A} = 1$ in equation (30).

Non-rigid (vibrating) linear molecules behave like symmetric-top molecules [56]. However, the rotational wave function takes a different form depending on the Hund's coupling case chosen, which is an idealised situation of describing the total molecular wave function [56]. In these cases the rotational wave function is usually taken as a linear combination of normalised symmetric-top functions

$$R_{nJm_J}(\hat{\boldsymbol{R}}) = \sqrt{\frac{(2J_n + 1)}{8\pi^2}} D^{J*}_{m_J, m_n}(\hat{\boldsymbol{R}}), \tag{31}$$

where m_J is the angular momentum projection of J and m_n is the orbital angular momentum projection of the electronic state.

In the rigid (non-vibrating) rotor approximation the rotational wave function is given by

$$R_{nJm_J}(\hat{\boldsymbol{R}}) = Y_{Jm_J}(\hat{\boldsymbol{R}}), \tag{32}$$

which is spherically symmetric for $J = 0$. Some studies utilise the rigid rotor approximation to formulate the DCS [31, 58].

Substituting an appropriate rotational wave function (for the molecular target) into the scattering amplitude (28), the integration over $\hat{\boldsymbol{R}}$ (in the laboratory frame of reference) can be carried out analytically for a partial-wave form of the T-matrix. Then the DCS (18) resolved for the transition $i\nu_i J_i m_{J_i} \rightarrow f\nu_f J_f m_{J_f}$ can be formulated [35].

2.3. Body- and laboratory-frame formulation and transformation

The adiabatic-nuclei scattering amplitude (28) looks like it requires data of the T-matrix for many orientations $\hat{\boldsymbol{R}}$ of the molecule. However analytic integration over $\hat{\boldsymbol{R}}$ can be carried out by utilising the rotation matrices. This method requires the three-dimensional T-matrix $T^{\mathcal{S}}_{f,i}(\boldsymbol{q}_f, \boldsymbol{q}_i; \boldsymbol{R})$ to be expressed in partial-wave form and to be calculated for a single arbitrary orientation of the molecule. The frame of reference and single orientation of the molecule are chosen as the most convenient. This frame of reference is known as the body-frame and equations formulated in this frame are labelled by superscript $^{(\mathrm{b})}$ (i.e. in the body-frame $T^{\mathcal{S}}_{f,i}(\boldsymbol{q}_f^{(\mathrm{b})}, \boldsymbol{q}_i^{(\mathrm{b})}; R)$).

For homonuclear diatomic molecules the body-frame of reference is conveniently chosen to have the origin set halfway between the nuclei and to align the internuclear axis with the z-axis. Physically, however, the molecule is oriented in the laboratory (lab)-frame of reference (denoted by superscript $^{(\mathrm{lab})}$) $\hat{\boldsymbol{R}}^{(\mathrm{lab})}$ and the projectile-particle's initial momentum vector $\hat{\boldsymbol{q}}_i$ is aligned along the lab-frame z-axis (i.e. $\hat{\boldsymbol{q}}_i^{(\mathrm{lab})} = \hat{\boldsymbol{z}}^{(\mathrm{lab})}$). Note that the rotational wave functions (31) and (32) are formulated in the lab-frame of reference.

To carry out the integration over $\hat{\boldsymbol{R}}^{(\mathrm{lab})}$ analytically in equation (28), and to save on computational resources in the calculation of the three-dimensional body-frame fixed-nuclei T-matrix $T^{\mathcal{S}}_{f,i}(\boldsymbol{q}_f^{(\mathrm{b})}, \boldsymbol{q}_i^{(\mathrm{b})}; R)$, the projectile partial-wave expansion is utilised. This allows us to express $T^{\mathcal{S}}_{f,i}(\boldsymbol{q}_f^{(\mathrm{b})}, \boldsymbol{q}_i^{(\mathrm{b})}; R)$ in partial-wave form, which for convenience can be written as

$$\begin{aligned} -(2\pi)^2 T^{\mathcal{S}}_{f,i}(\boldsymbol{q}_f^{(\mathrm{b})}, \boldsymbol{q}_i^{(\mathrm{b})}; R) = &\sum_{\substack{L_f, L_i \\ M_f, M_i}} A^{\mathcal{S}(\mathrm{b})}_{fL_f M_f, iL_i M_i}(R) \\ &\times Y_{L_f M_f}(\hat{\boldsymbol{q}}_f^{(\mathrm{b})}) Y^*_{L_i M_i}(\hat{\boldsymbol{q}}_i^{(\mathrm{b})}), \end{aligned} \tag{33}$$

where L and M are the projectile orbital angular momentum and orbital angular projection respectively, and $A^{\mathcal{S}(\mathrm{b})}_{fL_fM_f,iL_iM_i}$ contains the body-frame partial-wave fixed-nuclei T-matrix elements and is defined below in equation (96). Following the definition of equation (19), the left-hand side of equation (33) can be defined as the fixed-nuclei body-frame scattering amplitude for the transition $i \rightarrow f$, where $F^{\mathcal{S}}_{f,i}(\boldsymbol{q}^{(\mathrm{b})}_f, \boldsymbol{q}^{(\mathrm{b})}_i; R) \equiv -(2\pi)^2 T^{\mathcal{S}}_{f,i}(\boldsymbol{q}^{(\mathrm{b})}_f, \boldsymbol{q}^{(\mathrm{b})}_i; R)$.

To transform $T^{\mathcal{S}}_{f,i}(\boldsymbol{q}^{(\mathrm{b})}_f, \boldsymbol{q}^{(\mathrm{b})}_i; R)$ to the lab-frame of reference, we rotate the lab-frame coordinate system (space-fixed frame) so as to align $\hat{\boldsymbol{z}}^{(\mathrm{lab})}$ to the body-frame z-axis $\hat{\boldsymbol{z}}^{(\mathrm{b})}$, noting that $\hat{\boldsymbol{z}}^{(\mathrm{b})}$ is aligned along the lab-frame internuclear axis $\hat{\boldsymbol{R}}^{(\mathrm{lab})}$. Hence by utilising the Wigner-D rotation matrices $D^L_{\kappa,M}(\boldsymbol{\beta})$ defined in [59], a rotation by angles $\hat{\boldsymbol{R}}^{(\mathrm{lab})} \equiv (\theta_{\hat{\boldsymbol{R}}}, \phi_{\hat{\boldsymbol{R}}})$ will align $\hat{\boldsymbol{z}}^{(\mathrm{lab})}$ with the $\hat{\boldsymbol{R}}^{(\mathrm{lab})}$ and bring $T^{\mathcal{S}}_{f,i}(\boldsymbol{q}^{(\mathrm{b})}_f, \boldsymbol{q}^{(\mathrm{b})}_i; R)$ into the lab-frame (i.e. $T^{\mathcal{S}}_{f,i}(\boldsymbol{q}^{(\mathrm{lab})}_f, \boldsymbol{q}^{(\mathrm{lab})}_i; R)$), with a connection to the body-frame. For our application we have the following definition

$$Y_{LM}(\hat{\boldsymbol{q}}^{(\mathrm{b})}) = \sum_{\kappa} D^L_{\kappa,M}(\hat{\boldsymbol{R}}^{(\mathrm{lab})}) Y_{L\kappa}(\hat{\boldsymbol{q}}^{(\mathrm{lab})}), \tag{34}$$

where the Euler angles $\boldsymbol{\beta}$ are chosen such that $\boldsymbol{\beta} = (\phi_{\hat{\boldsymbol{R}}}, \theta_{\hat{\boldsymbol{R}}}, 0) = \hat{\boldsymbol{R}}^{(\mathrm{lab})}$ [34, 56]. Utilising this definition and noting that the lab-frame incident projectile-momentum is aligned along the z-axis, the lab-frame T-matrix can be expressed such that

$$\begin{aligned} -(2\pi)^2 T^{\mathcal{S}}_{f,i}(\boldsymbol{q}^{(\mathrm{lab})}_f, \boldsymbol{q}^{(\mathrm{lab})}_i; R) &= \sum_{\substack{L_f,L_i \\ M_f,M_i}} A^{\mathcal{S}(\mathrm{b})}_{fL_fM_f,iL_iM_i}(R) \\ &\times \frac{\hat{L}_i}{\sqrt{4\pi}} \sum_{\kappa} D^{L_f}_{\kappa,M_f}(\hat{\boldsymbol{R}}^{(\mathrm{lab})}) D^{L_i*}_{0,M_i}(\hat{\boldsymbol{R}}^{(\mathrm{lab})}) Y_{L_f\kappa}(\hat{\boldsymbol{q}}^{(\mathrm{lab})}_f), \end{aligned} \tag{35}$$

and the scattering amplitude of equation (28) can be expressed as

$$\begin{aligned} &F^{\mathcal{S}}_{fv_f J_f m_{J_f},iv_i J_i m_{J_i}}(\boldsymbol{q}^{(\mathrm{lab})}_f, \boldsymbol{q}^{(\mathrm{lab})}_i) \\ &= \sum_{\substack{L_f,L_i \\ M_f,M_i}} \frac{\hat{L}_i}{\sqrt{4\pi}} \langle \nu_{fv_f J_f} | A^{\mathcal{S}(\mathrm{b})}_{fL_fM_f,iL_iM_i} | \nu_{iv_i J_i} \rangle_R \\ &\times \langle R_{fJ_f m_{J_f}} | \sum_{\kappa} D^{L_f}_{\kappa,M_f} D^{L_i*}_{0,M_i} | R_{iJ_i m_{J_i}} \rangle_{\hat{\boldsymbol{R}}^{(\mathrm{lab})}} Y_{L_f\kappa}(\hat{\boldsymbol{q}}^{(\mathrm{lab})}_f), \end{aligned} \tag{36}$$

where $\hat{L} = \sqrt{(2L+1)}$.

2.4. Orientation averaging and cross sections

In the classical orientation averaging procedure the target diatomic molecule has equal probability of being oriented in an arbitrary direction and scattering cross sections are calculated by averaging over all orientations of the molecule [47, 60–62]. Referring to appendix A, the classical orientation averaging formula of the cross sections can be obtained by substituting the rigid rotor rotational wave functions (32) into lab-frame scattering amplitude (36) and summing transitions over all final rotational states J_f, for a molecule initially in the ground rotational state $J_i = 0$. Hence in the classical orientation averaging procedure the DCS is resolved for the transition $iv_i \rightarrow fv_f$, where the molecule is in the $J_i = 0$ state and transitions are summed over J_f analytically. In this procedure (referring to equation (36)) the lab-frame scattering amplitude is usually expressed as

$$\begin{aligned} F^{\mathcal{S}}_{fv_f,iv_i}(\boldsymbol{q}^{(\mathrm{lab})}_f, \boldsymbol{q}^{(\mathrm{lab})}_i, \hat{\boldsymbol{R}}^{(\mathrm{lab})}) &= \sum_{\substack{L_f,L_i \\ M_f,M_i}} \frac{\hat{L}_i}{\sqrt{4\pi}} \\ &\times \langle \nu_{fv_f} | A^{\mathcal{S}(\mathrm{b})}_{fL_fM_f,iL_iM_i} | \nu_{iv_i} \rangle_R \sum_{\kappa} D^{L_f}_{\kappa,M_f}(\hat{\boldsymbol{R}}^{(\mathrm{lab})}) \\ &\times D^{L_i*}_{0,M_i}(\hat{\boldsymbol{R}}^{(\mathrm{lab})}) Y_{L_f\kappa}(\hat{\boldsymbol{q}}^{(\mathrm{lab})}_f). \end{aligned} \tag{37}$$

We note that vibrational wave functions $\nu_{nv_nJ_n}(R)$ have a very minor dependence on J and we assume that they are independent of J and write them as ν_{nv_n}. To obtain orientationally averaged DCS, $F^{\mathcal{S}}_{fv_f,iv_i}(\boldsymbol{q}^{(\mathrm{lab})}_f, \boldsymbol{q}^{(\mathrm{lab})}_i, \hat{\boldsymbol{R}}^{(\mathrm{lab})})$ is substituted into the DCS equation (18) and averaged over all orientations of the molecule

$$\frac{\mathrm{d}\sigma^{\mathcal{S}}_{fv_f,iv_i}}{\mathrm{d}\Omega^{(\mathrm{lab})}} = \frac{q_f}{q_i} \frac{1}{4\pi} \int |F^{\mathcal{S}}_{fv_f,iv_i}(\boldsymbol{q}^{(\mathrm{lab})}_f, \boldsymbol{q}^{(\mathrm{lab})}_i, \hat{\boldsymbol{R}}^{(\mathrm{lab})})|^2 \mathrm{d}\Omega_{R^{(\mathrm{lab})}}. \tag{38}$$

The orientationally averaged DCS (38) is evaluated in appendix A and the final form is

$$\begin{aligned} \frac{\mathrm{d}\sigma^{\mathcal{S}}_{fv_f,iv_i}}{\mathrm{d}\Omega^{(\mathrm{lab})}} &= \frac{q_f}{q_i} \frac{1}{(4\pi)^2} \sum_{\substack{L_f,L_i \\ M_f,M_i}} \sum_{\substack{L'_f,L'_i \\ M'_f,M'_i}} (-1)^{M'_i+M'_f} \hat{L}_i \hat{L}'_i \hat{L}_f \hat{L}'_f \\ &\times \langle \nu_{fv_f} | A^{\mathcal{S}(\mathrm{b})}_{fL_fM_f,iL_iM_i} | \nu_{iv_i} \rangle_R \langle \nu^*_{fv_f} | A^{\mathcal{S}(\mathrm{b})*}_{fL'_fM'_f,iL'_iM'_i} | \nu^*_{iv_i} \rangle_{R'} \\ &\times \sum_j (2j+1)^{-1} C^{j0}_{L_i0,L'_i0} C^{jM'_i-M_i}_{L_i-M_i,L'_iM'_i} C^{jM_f-M'_f}_{L_fM_f,L'_f-M'_f} \\ &\times C^{j0}_{L_f0,L'_f0} P_j(\cos(\theta^{(\mathrm{lab})})) \delta_{M_i-M'_i,M_f-M'_f}, \end{aligned} \tag{39}$$

where $C^{lm}_{l_1m_1,l_2m_2}$ and P_j denote Clebsch–Gordan coefficients and Legendre polynomials, respecitvely.

The integrated cross sections are calculated by integrating the DCS in equation (39) over all final angles. Orientationally averaged integrated cross sections have the final form

$$\sigma^{\mathcal{S}}_{fv_f,iv_i} = \frac{q_f}{q_i} \frac{1}{4\pi} \sum_{\substack{L_f,L_i \\ M_f,M_i}} |\langle \nu_{fv_f} | A^{\mathcal{S}(\mathrm{b})}_{fL_fM_f,iL_iM_i} | \nu_{iv_i} \rangle_R|^2. \tag{40}$$

Some experiments measure cross sections that are summed over all final vibrational levels and are resolved for the transition $iv_i \rightarrow f$. The closure property of the vibrational wave functions

$$\sum\!\!\!\!\!\!\int_{v_f} \nu^*_{fv_f}(R) \nu_{fv_f}(R') = \frac{1}{R'^2} \delta(R - R'), \tag{41}$$

can be utilised to sum integrated cross sections in equation (40) over all final vibrational states

$$\sigma^{\mathcal{S}}_{f,iv_i} = \sum\!\!\!\!\!\!\int_{v_f} \sigma^{\mathcal{S}}_{fv_f,iv_i} = \frac{q_f}{q_i}\frac{1}{4\pi}\sum_{\substack{L_f,L_i\\M_f,M_i}} \langle \nu_{iv_i}|A^{\mathcal{S}(\mathrm{b})}_{fL_fM_f,iL_iM_i}|^2|\nu_{iv_i}\rangle_R. \quad (42)$$

For convenience the integrated cross section in equation (42) can be expressed in the alternative form

$$\sigma^{\mathcal{S}}_{f,iv_i} = \langle \nu_{iv_i}|\sigma^{\mathcal{S}}_{f,i}|\nu_{iv_i}\rangle_R, \quad (43)$$

where $\sigma^{\mathcal{S}}_{f,i}(R)$ is the fixed-nuclei integrated cross section at the internuclear distance R

$$\sigma^{\mathcal{S}}_{f,i}(R) = \frac{q_f}{q_i}\frac{1}{4\pi}\sum_{\substack{L_f,L_i\\M_f,M_i}} |A^{\mathcal{S}(\mathrm{b})}_{fL_fM_f,iL_iM_i}(R)|^2. \quad (44)$$

Scattering calculations performed in the 'fixed-nuclei' approximation generally refer to calculations being performed at one internuclear distance R. Because the probability density function of the vibrational ground state ($v = 0$) is approximately a Gaussian function, a common approximation is to replace the integration in equation (43) with a fixed-nuclei cross section (44) chosen at an appropriate value of $R = R_c$. This value R_c is generally chosen as the equilibrium distance $R = R_0$, which is localised at the position near the peak of the vibrational ground state wave function and hence is seen as a good approximation of scattering from the vibrational ground state. In this approximation equation (43) becomes

$$\sigma^{\mathcal{S}}_{f,iv_i=0} \approx \sigma^{\mathcal{S}}_{f,i}(R_0) = \frac{q_f}{q_i}\frac{1}{4\pi}\sum_{\substack{L_f,L_i\\M_f,M_i}} |A^{\mathcal{S}(\mathrm{b})}_{fL_fM_f,iL_iM_i}(R_0)|^2. \quad (45)$$

As shown in previous publications [63, 64] and explicitly in section 8 and [49], by choosing R_c to be the mean internuclear distance R_m of the ground vibrational wave function, the fixed-nuclei approximation more accurately approximates equation (42), compared to choosing R_c as the equilibrium distance R_0.

3. Molecular target structure

In the molecular CCC method target states are constructed utilising the Born–Oppenheimer approximation and electronic target states are formulated within the body-frame, where the origin is set at the geometrical centre of the nuclei (as described above in section 2.3).

3.1. H_2^+ electronic target states

The H_2^+ target electronic Hamiltonian H_T^{Elec} in the Born–Oppenheimer approximation describes an electron in the Coulomb potential of two protons that are fixed at a distance R and is defined as

$$H_T^{\mathrm{Elec}} = H_1^{\mathrm{Elec}} + 1/R, \quad (46)$$

where $1/R$ is the internuclear Coulomb repulsion term. The one-electron (or positron) electronic Hamiltonian H_i^{Elec} for homonuclear diatomic molecules is

$$H_i^{\mathrm{Elec}} = K_i(r_i) + V_i(\boldsymbol{r}_i; \boldsymbol{R}), \quad (47)$$

where

$$K_i(r_i) = -\frac{1}{2}\frac{\mathrm{d}^2}{\mathrm{d}r_i^2} + \frac{l(l+1)}{2r_i^2}, \quad (48)$$

$$V_i(\boldsymbol{r}_i; \boldsymbol{R}) = \left(\frac{z_i}{\left|\boldsymbol{r}_i + \frac{\boldsymbol{R}}{2}\right|} + \frac{z_i}{\left|\boldsymbol{r}_i - \frac{\boldsymbol{R}}{2}\right|}\right). \quad (49)$$

The electron–nuclei (or positron–nuclei) potential (49) in the Born–Oppenheimer approximation is expanded in partial waves

$$\begin{aligned} V_i(\boldsymbol{r}_i; \boldsymbol{R}) &= 2z_i \sum_{\lambda=0,2,4,..}^{\infty} \sqrt{\frac{4\pi}{(2\lambda+1)}}\, v_\lambda(r_i, R/2) Y_{\lambda 0}(\hat{\boldsymbol{r}}_i) \\ &= z_i \sum_{\lambda=0}^{\infty} (1 + (-1)^\lambda) \sqrt{\frac{4\pi}{(2\lambda+1)}} \\ &\quad \times v_\lambda(r_i, R/2) Y_{\lambda 0}(\hat{\boldsymbol{r}}_i), \end{aligned} \quad (50)$$

where

$$v_\lambda(r_i, r_j) = \frac{r_<^\lambda}{r_>^{\lambda+1}}, \quad (51)$$

$r_< = \min(r_i, r_j)$ and $r_> = \max(r_i, r_j)$.

The electronic target states of H_2^+ are characterised by the projection of orbital angular momentum m, parity π and spin s, with $s = 1/2$. For each combination of (m, π, s) the generalised eigenvalue problem (for either an orthogonal or non-orthogonal basis $\{\phi_i\}$)

$$\sum_{j=1}^{N} (\langle \phi_i|H_T^{\mathrm{Elec}}|\phi_j\rangle - \varepsilon^{\mathrm{Elec}}(R)\langle \phi_i|\phi_j\rangle) C_j = 0, \quad (52)$$

is solved via diagonalisation of the target electronic Hamiltonian (46) to obtain energies $\varepsilon^{\mathrm{Elec}}(R)$ (eigenvalues) and expansion coefficients C_j (eigenvectors). Once these are obtained, electronic target states are constructed

$$\Phi_n^{m\pi}(\mathbf{x}_1) = \sum_{j=1}^{N} C_j^{(n)} \phi_j^{m\pi}(\mathbf{x}_1), \quad (53)$$

where N is the number of one-electron orbitals $\phi_j^{m\pi}(\mathbf{x})$.

For H_2^+, one-electron orbitals are represented by

$$\phi_j^{m\pi}(\mathbf{x}) = \frac{1}{r}\varphi_{k_j l_j}(r) Y_{l_j m_j}(\hat{\boldsymbol{r}}) \chi_{m_{s_j}}(\sigma), \quad (54)$$

with $m_j = m$, $(-1)^{l_j} = \pi$ and $\chi_{m_{s_j}}(\sigma)$ is the spin-$\frac{1}{2}$ eigenfunction with angular projection m_{s_j}. The radial functions $\varphi_{k_j l_j}(r)$ are the Laguerre functions

$$\begin{aligned} \varphi_{kl}(r) &= \sqrt{\frac{\alpha_l (k-1)!}{(k+l)(k+2l)!}} (2\alpha_l r)^{l+1} \\ &\quad \times \exp(-\alpha_l r) L_{k-1}^{2l+1}(2\alpha_l r), \end{aligned} \quad (55)$$

where α_l is the exponential fall-off parameter, L_{k-1}^{2l+1} are the associated Laguerre polynomials of order $2l + 1$ and k ranges

from 1 to N_l. N_l is the number of Laguerre basis function per orbital angular momentum l, where the largest value of l is $l_{\max}$. Analytic properties of Laguerre basis functions of order $2l + 1$ [65] have extensively been used in the J-matrix method [66] to evaluate matrix elements of the target Hamiltonian (46). These matrix elements are given in appendix B. Note that each Laguerre basis function constructs $2l + 1$ one-electron orbitals and electronic target states.

The choice of the exponential fall-off parameters α_l can result in more (or less) accurate electronic pseudostates, and controls the pseudostates energy distribution. For example the ground state of the H_2 molecule (similar to atomic He) is very tightly bound compared to the excited states. In our models [48, 49, 67], we chose short-ranged (large α_l) Laguerre functions for the first few low-lying functions to account for the electron correlations in the short-ranged electronic ground state wave function. Long-ranged (small α_l) functions were utilised for the rest of the basis, which primarily construct the relatively long-ranged electronic excited states. The long-ranged functions α_l is then optimised to adjust the resulting pseudostates energy distribution in order to accurately distinguish the scattering flux captured by the continuum and discrete spectrum. We generally aim to have the negative-energy pseudostates as far as possible from the ionisation threshold, and the first positive energy pseudostates close to the ionisation threshold. This allows us to accurately model the inter-channel coupling to low-energy ionisation processes.

3.2. Molecular orbital basis functions

The multi-centre nature of the H_2^+ and H_2 molecules leads to a slow convergence rate of the calculated wave functions with respect to the orbital angular momentum l of the one-electron orbitals. This is only an issue for the ground and few lowest-lying excited states; other states are usually hydrogenic and are well represented in a single-centre Laguerre basis formulation.

Specifically for H_2^+ we find a slow convergence rate of the $1s\sigma_g$ ground state and $2p\sigma_u$ excited state. For H_2 only the ground state $X^1\Sigma_u^+$ and first excited triplet state $b^3\Sigma_u^+$ converge slowly. To improve accuracy and save on computational resources, structure calculations are performed in two steps. Firstly, a large Laguerre basis is used to diagonalise the H_2^+ target Hamiltonian (46) and generate accurate $1s\sigma_g$ and $2p\sigma_u$ states of H_2^+. Secondly, a new Laguerre basis is produced with smaller values of l and N_l.

For H_2^+ the $1s\sigma_g$ and $2p\sigma_u$ orbitals of this new (smaller) basis are replaced with the accurate $1s\sigma_g$ and $2p\sigma_u$ states (molecular orbitals) calculated at the first step. For H_2 the $1s\sigma_g$ orbital of this new basis is replaced with the accurate $1s\sigma_g$ molecular orbital calculated at the first step. This new basis is then used to diagonalise the respective target Hamiltonian and generate electronic states that are used in the scattering calculations.

3.3. H_2 electronic target states

The H_2 target electronic Hamiltonian $H_{\rm T}^{\rm Elec}$ in the Born–Oppenheimer approximation describes two electrons in the Coulomb potential of two protons that are fixed at a distance R and is defined as

$$H_{\rm T}^{\rm Elec} = H_1^{\rm Elec} + H_2^{\rm Elec} + V_{12} + 1/R, \tag{56}$$

where V_{12} is the electron–electron (or positron–electron) potential expanded in partial waves

$$V_{i,j} = \frac{z_i z_j}{|\boldsymbol{r}_i - \boldsymbol{r}_j|} = z_i z_j \sum_{\lambda\mu}^{\infty} (-1)^{\mu} \frac{4\pi}{(2\lambda+1)} \times v_\lambda(r_i, r_j) Y_{\lambda-\mu}(\hat{\boldsymbol{r}}_i) Y_{\lambda\mu}(\hat{\boldsymbol{r}}_j), \tag{57}$$

and $v_\lambda(r_i, r_j)$ is defined in equation (51).

Electronic target states of H_2 are constructed using a similar method to that described above in section 3.1 for H_2^+. The target Hamiltonian (56) is diagonalised in a set of anti-symmetrised two-electron configurations and then target states are constructed. The electronic target states of H_2 are characterised by their orbital angular momentum projection m, parity π and spin s. The two-electron configurations $\phi_{\gamma,\delta}^{m\pi s}(\mathbf{x}_1, \mathbf{x}_2)$ of H_2 are constructed from antisymmetric combinations of one-electron orbitals $\phi(\mathbf{x})$ (54)

$$\phi_{\gamma,\delta}^{m\pi s}(\mathbf{x}_1, \mathbf{x}_2) = \frac{1}{\sqrt{2(1+\delta_{\gamma,\delta})}} \mathcal{A} |\phi_\gamma(\mathbf{x}_1)\phi_\delta(\mathbf{x}_2) : m\pi s m_s\rangle, \tag{58}$$

where the antisymmetrisation operator is $\mathcal{A} = 1 - P_{12}$.

Diagonalising the H_2 target Hamiltonian (56), eigenvectors $C_{\gamma,\delta}^{(n)}$ and eigenvalues are obtained. H_2 target states are then constructed and are represented by ordered configurations

$$\begin{aligned}\Phi_n^{m\pi s}(\mathbf{x}_1, \mathbf{x}_2) &= \sum_{\gamma\delta} C_{\gamma,\delta}^{(n)} |\phi_\gamma(\mathbf{x}_1)\phi_\delta(\mathbf{x}_2) : m\pi s m_s\rangle \\ &= \frac{1}{r_1 r_2} \sum_{\gamma\delta} C_{\gamma,\delta}^{(n)} \varphi_\gamma(r_1)\varphi_\delta(r_2) \\ &\quad \times Y_{l_\gamma m_\gamma}(\hat{\boldsymbol{r}}_1) Y_{l_\delta m_\delta}(\hat{\boldsymbol{r}}_2) X_{m_s}^s,\end{aligned} \tag{59}$$

where, to account for the antisymmetry of the two-electron wave functions (59), the CI coefficients satisfy $C_{\gamma\delta}^{(n)} = (-1)^s C_{\delta\gamma}^{(n)}$, and the spin function is

$$X_{m_s}^s = \sum_{m_{s_\gamma} m_{s_\delta}} C_{\frac{1}{2}m_{s_\gamma}, \frac{1}{2}m_{s_\delta}}^{s m_s} \chi_{m_{s_\gamma}}(\sigma_1)\chi_{m_{s_\delta}}(\sigma_2). \tag{60}$$

3.4. Nuclear wave functions

For a diatomic molecule in the n electronic state, the total non-relativistic Born–Oppenheimer Hamiltonian is given by

$$H_n^{\rm BO} = -\frac{1}{2\mu}\frac{{\rm d}^2}{{\rm d}R^2} + \frac{J(J+1) - m_n^2}{2\mu R^2} + \varepsilon_n^{\rm Elec}(R), \tag{61}$$

where the reduced mass is $\mu = M_1 M_2/(M_1 + M_2)$ and M_i is the mass of the individual nuclei; $M_i = 1836.152$ for a proton, $M_i = 3670.483$ for a deuteron and $M_i = 5496.922$ for a triton.

By performing structure calculations over the range of R and interpolating, the Born–Oppenheimer potential energy curves $\varepsilon_n^{\rm Elec}(R)$ are obtained (as defined in [57]). Here, however, for the electronic ground state ($m = 0$) we utilise the accurate Born–Oppenheimer potential energy curve of Wolniewicz and Poll [68] for H_2^+ and for H_2 we use the potential energy curve of Kolos *et al* [69].

Nuclear wave functions $\Xi_{nvJm_J}(\boldsymbol{R})$ of the electronic ground state are calculated via diagonalisation of the total Hamiltonian (61) for each rotational angular momentum J using a set of nuclear orbitals

$$\xi_j(\boldsymbol{R}) = \frac{1}{R}\varphi_{k_jJ_j}(R)\,Y_{J_jm_j}(\hat{\boldsymbol{R}}). \tag{62}$$

Here $\varphi_{k_jJ_j}(R)$ are Laguerre basis functions (55). We diagonalise the total $m = 0$ Born–Oppenheimer Hamiltonian (61) with a large set of $J = 0$ nuclear orbitals that was taken to convergence. The resulting molecular state energies [42, 49] were found to be in good agreement with the calculations of Wünderlich and Fantz [70] for H_2^+, D_2^+ and T_2^+, and of Wünderlich and Fantz [71] for H_2.

4. The CCC method

Following from the adiabatic-nuclei approximation introduced in section 2.2, the scattering system Schrödinger equation is formulated in the body-frame for a fixed internuclear distance R (and orientation) of the diatomic molecule

$$(E^{(+)} - H)|\Psi_i^{\mathcal{S}(+)}\rangle = 0. \tag{63}$$

Here the scattering Hamiltonian H is a sum of the single-particle Hamiltonian for the projectile $H_0^{\rm Elec}$ (47), the projectile-target electron interaction potential terms V_{0j} (57) and the target Hamiltonian $H_{\rm T}^{\rm Elec}$ given in equation (46) for H_2^+ and equation (56) for H_2

$$H = H_{\rm T}^{\rm Elec} + H_0^{\rm Elec} + \sum_{j=1}^{N_e} V_{0j}. \tag{64}$$

A general form of the scattering system asymptotic Hamiltonian $H_{\rm asy}$ is chosen such that

$$H_{\rm asy} = H_{\rm T}^{\rm Elec} + K_0^{\rm Elec} + \frac{z_0 Z_{\rm Ion}}{r_0} + U_0, \tag{65}$$

where z_0 is the charge of the projectile. This form of $H_{\rm asy}$ allows for scattering from ionic targets with asymptotic charge $Z_{\rm Ion}$ (for H_2^+ $Z_{\rm Ion} = 1$). The method described here is also suitable for asymptotically neutral targets by taking $Z_{\rm Ion} = 0$ (as is the case for H_2). An optional short-ranged distorting potential U_0 (detailed later in section 4.4) is used purely for numerical stability of the solution and does not change final CCC results. For this choice of the asymptotic Hamiltonian $H_{\rm asy}$ (65), $|\Phi_n^N \boldsymbol{k}^{(+)}\rangle$ satisfy

$$0 = I^N(E^{(+)} - H_{\rm asy})|\Phi_n^N \boldsymbol{k}^{(+)}\rangle = (E^{(+)} - \varepsilon_k - \varepsilon_n^N)|\Phi_n^N \boldsymbol{k}^{(+)}\rangle, \tag{66}$$

where I^N is the projection operator (75) in the target space and $|\boldsymbol{k}^{(\pm)}\rangle$ denotes a distorted-wave normalised in momentum space, which is a solution of the equation

$$(\varepsilon_k^{(\pm)} - K_0 - z_0 Z_{\rm Ion}/r_0 - U_0)|\boldsymbol{k}^{(\pm)}\rangle = 0. \tag{67}$$

Following from equation (30) the CCC method utilises a multichannel expansion for this choice of $H_{\rm asy}$ (65), which is explicitly antisymmetrised in the case of electron-scattering. The fixed-nuclei total scattering wave function $\Psi_i^{\mathcal{S}(+)}(\mathbf{x}_0, \mathbf{x}; R)$ is expanded over a (near) complete set of N positive- and negative-energy pseudostates $\Phi_n^N(\mathbf{x}; R)$ of the target (formulated in section 3)

$$\begin{aligned}\Psi_i^{\mathcal{S}N(+)}(\mathbf{x}_0, \mathbf{x}; R) &= \mathcal{A}\sum_{n=1}^{N}\Phi_n^N(\mathbf{x}; R) f_{ni}^{\mathcal{S}N(+)}(\mathbf{x}_0; R) \\ &= \mathcal{A}\psi_i^{\mathcal{S}N(+)}(\mathbf{x}_0, \mathbf{x}; R),\end{aligned} \tag{68}$$

where the positive-energy pseudostates provide a discretised representation of the target continuum. The CCC method relies on the completeness of the Laguerre basis and hence pseudostates $\Phi_n^N(\mathbf{x}; R)$ such that

$$\lim_{N\to\infty} \Psi_i^{\mathcal{S}N(+)}(\mathbf{x}_0, \mathbf{x}; R) = \Psi_i^{\mathcal{S}(+)}(\mathbf{x}_0, \mathbf{x}; R). \tag{69}$$

The single-centre positron scattering approach is discussed in section 8.1, and note that for positron scattering $\mathcal{A}$ is not required in equation (68).

4.1. Non-uniqueness in electron scattering

The antisymmetric total wave function $\Psi_i^{\mathcal{S}N(+)}(\mathbf{x}_0, \mathbf{x}; R)$ in equation (68) is unique, however $\psi_i^{\mathcal{S}N(+)}(\mathbf{x}_0, \mathbf{x}; R)$ is not unique since the antisymmetrisation operator can transform two different functions into one single function. Hence expression (68) is too general and leads to non-unique solutions [54, 55, 72, 73]. For example, suppose functions $g_n^{\mathcal{S}N}(\mathbf{x}_0; R)$ are of the form

$$0 = \mathcal{A}\sum_{n=1}^{N}\Phi_n^N(\mathbf{x}; R) g_n^{\mathcal{S}N}(\mathbf{x}_0; R), \tag{70}$$

then there are solutions

$$\begin{aligned}\Psi_i^{\mathcal{S}N(+)}(\mathbf{x}_0, \mathbf{x}; R) = \mathcal{A}\sum_{n=1}^{N}\Phi_n^N(\mathbf{x}; R) \\ \times (f_{ni}^{\mathcal{S}N(+)}(\mathbf{x}_0; R) + B g_n^{\mathcal{S}N}(\mathbf{x}_0; R)),\end{aligned} \tag{71}$$

for any constant B.

In practice this non-unique expansion leads to the non-unique half-on-shell K- and T-matrices and consequently can lead to numerical instabilities in the calculation of the on-shell K- and T-matrices. Non-uniqueness becomes evident when a small variation in the momentum quadrature points in the Green's function (81) (k-grid) leads to a large variation in the on-shell T-matrix results. This is a purely numerical problem that has been addressed for atomic and ionic targets [54, 55, 73], and a similar technique is applied to molecules. The non-uniqueness problem is solved by forcing $g_n^{\mathcal{S}N}(\mathbf{x}_0; R) = 0$.

For electron scattering from H_2^+ forcing $g_n^{\mathcal{S}N}(\mathbf{x}_0; R) = 0$ is accomplished by making $\psi_i^{\mathcal{S}N(+)}(\mathbf{x}_0, \mathbf{x}_1; R)$ antisymmetric like $\Psi_i^{\mathcal{S}N(+)}(\mathbf{x}_0, \mathbf{x}_1; R)$, hence

$$\psi_i^{\mathcal{S}N(+)}(\boldsymbol{r}_0, \boldsymbol{r}_1; R) = (-1)^{\mathcal{S}} P_{\boldsymbol{r}_0,\boldsymbol{r}_1} \psi_i^{\mathcal{S}N(+)}(\boldsymbol{r}_0, \boldsymbol{r}_1; R). \quad (72)$$

By having $\psi_i^{\mathcal{S}N(+)}(\boldsymbol{r}_0, \boldsymbol{r}_1; R)$ antisymmetric (72), the following condition is true

$$\langle \Phi_j^N | f_{ni}^{\mathcal{S}N(+)} \rangle = (-1)^{\mathcal{S}} \langle \Phi_n^N | f_{ji}^{\mathcal{S}N(+)} \rangle, \quad (73)$$

which leads to the property

$$(-1)^{\mathcal{S}} \langle \boldsymbol{k}_f^{(-)} \Phi_f^N | P_{\boldsymbol{r}_0,\boldsymbol{r}_1} | \psi_i^{\mathcal{S}N(+)} \rangle = \langle \boldsymbol{k}_f^{(-)} \Phi_f^N | I_0^N | \psi_i^{\mathcal{S}N(+)} \rangle, \quad (74)$$

where the projection operator I_0^N is in the projectile space 0 and is expressed as an expansion over all electronic target states of H_2^+

$$I_0^N = \sum_{n=1}^{N} |\Phi_n^N\rangle \langle \Phi_n^N|. \quad (75)$$

Utilising equation (74), the antisymmetrisation property of $\psi_i^{\mathcal{S}N(+)}(\boldsymbol{r}_0, \boldsymbol{r}_1; R)$ is implemented within the energy term of the V-matrix elements

$$\begin{aligned}
&(-1)^{\mathcal{S}} E \langle \boldsymbol{k}_f^{(-)} \Phi_f^N | P_{\boldsymbol{r}_0,\boldsymbol{r}_1} | \psi_i^{\mathcal{S}N(+)} \rangle \\
&= (-1)^{\mathcal{S}} (1 - \theta + \theta) E \langle \boldsymbol{k}_f^{(-)} \Phi_f^N | P_{\boldsymbol{r}_0,\boldsymbol{r}_1} | \psi_i^{\mathcal{S}N(+)} \rangle \\
&= (-1)^{\mathcal{S}} (1 - \theta) E \langle \boldsymbol{k}_f^{(-)} \Phi_f^N | P_{\boldsymbol{r}_0,\boldsymbol{r}_1} | \psi_i^{\mathcal{S}N(+)} \rangle \\
&\quad + \theta E \langle \boldsymbol{k}_f^{(-)} \Phi_f^N | I_0^N | \psi_i^{\mathcal{S}N(+)} \rangle \quad (76)
\end{aligned}$$

the left-hand side

$$\begin{aligned}
&(E^{(+)} - H_{\mathrm{T}} - K_0^{\mathrm{Elec}}) | \psi_i^{\mathcal{S}N(+)} \rangle \\
&= \left(V_0 + \sum_{j=1}^{N_e} V_{0j} + (E - H) \sum_{j=1}^{N_e} P_{0j} \right) | \psi_i^{\mathcal{S}N(+)} \rangle. \quad (77)
\end{aligned}$$

Subtracting the asymptotic target ion potential $\frac{z_0 Z_{\mathrm{Ion}}}{r_0}$ and short-ranged distorting potential U_0 on both sides

$$(E^{(+)} - H_{\mathrm{asy}}) | \psi_i^{\mathcal{S}N(+)} \rangle = V_U | \psi_i^{\mathcal{S}N(+)} \rangle, \quad (78)$$

where

$$V_U = V_0 + \sum_{j=1}^{N_e} V_{0j} - \frac{z_0 Z_{\mathrm{Ion}}}{r_0} - U_0 + (E - H) \sum_{j=1}^{N_e} P_{0j}. \quad (79)$$

Note that in single-centre positron scattering the exchange interaction (last term of equation (79)) is not present. To solve non-uniqueness for electron scattering, the interaction potential V_U (79) will have terms that are dependent on $\mathcal{S}$, N and θ [referring to equation (76)]. For generality, here we use the notation $V_U^{\mathcal{S}N}(\theta)$ for the interaction potential.

For the asymptotic Hamiltonian H_{asy} (65) the Green's function approach is utilised to transform the Schrödinger equation (63) to the momentum-space Lippmann–Schwinger equation

$$| \psi_i^{\mathcal{S}N(+)} \rangle = | \Phi_i^N \boldsymbol{k}_i^{(+)} \rangle + \sum_{n=1}^{N} \sum\!\!\!\!\!\!\int d^3k \, \frac{| \Phi_n^N \boldsymbol{k}^{(-)} \rangle \langle \boldsymbol{k}^{(-)} \Phi_n^N | V_U^{\mathcal{S}N}(\theta) | \psi_i^{\mathcal{S}N(+)} \rangle}{E^{(+)} - \varepsilon_k - \varepsilon_n^N + i0}. \quad (80)$$

Hence the antisymmetrisation property of $\psi_i^{\mathcal{S}N(+)}(\boldsymbol{r}_0, \boldsymbol{r}_1; R)$ (72) is enforced within the energy term of the V-matrix elements for non-zero θ. For electron scattering from H_2 and other quasi two-electron atoms, a similar approach is taken in the CCC method to eliminate non-unique solutions [55]. Details of the method are given in appendix C. The numerical stability of a calculation can be checked by varying θ, and the final CCC results are checked to be independent of the choice of non-zero θ.

4.2. Momentum-space coupled-channel Lippmann–Schwinger equation

The CCC method utilises the close-coupling expansion (68) and transforms the Schrödinger equation (63) into the momentum-space coupled-channel Lippmann–Schwinger equation. Here the dependence on R is suppressed for the brevity of notation.

Substituting $\Psi_i^{\mathcal{S}N(+)}(\mathbf{x}_0, \mathbf{x}; R)$ (68), the scattering Hamiltonian H (64) into the Schrödinger equation (63), and rearranging to have the asymptotic Hamiltonian H_{asy} (65) on

Premultiplying equation (80) by $\langle \boldsymbol{k}_f^{(-)} \Phi_f^N | V_U^{\mathcal{S}N}(\theta)$, the coupled Lippmann–Schwinger equation for the distorted-wave T-matrix is obtained

$$\begin{aligned}
&\langle \boldsymbol{k}_f^{(-)} \Phi_f^N | T_U^{\mathcal{S}N} | \Phi_i^N \boldsymbol{k}_i^{(+)} \rangle = \langle \boldsymbol{k}_f^{(-)} \Phi_f^N | V_U^{\mathcal{S}N}(\theta) | \Phi_i^N \boldsymbol{k}_i^{(+)} \rangle \\
&+ \sum_{n=1}^{N} \sum\!\!\!\!\!\!\int d^3k \frac{\langle \boldsymbol{k}_f^{(-)} \Phi_f^N | V_U^{\mathcal{S}N}(\theta) | \Phi_n^N \boldsymbol{k}^{(-)} \rangle \langle \boldsymbol{k}^{(-)} \Phi_n^N | T_U^{\mathcal{S}N} | \Phi_i^N \boldsymbol{k}_i^{(+)} \rangle}{E^{(+)} - \varepsilon_k - \varepsilon_n^N + i0}, \quad (81)
\end{aligned}$$

where f denotes the final state of the system and

$$\langle \boldsymbol{k}_f^{(-)} \Phi_f^N | T_U^{\mathcal{S}N} | \Phi_i^N \boldsymbol{k}_i^{(+)} \rangle \equiv \langle \boldsymbol{k}_f^{(-)} \Phi_f^N | V_U^{\mathcal{S}N}(\theta) | \psi_i^{\mathcal{S}N(+)} \rangle. \quad (82)$$

The short-ranged distorting potential U_0 in equations (66) and (67) can lead to a number of projectile bound states. For ionic targets there are an infinite number of projectile bound states, while for neutral targets U_0 can support a finite number of projectile bound states. Projectile bound states are included into the Green's function until convergence is reached. Referring to equation (82) the distorted-wave T-matrix $\langle \boldsymbol{k}_f^{(-)} \Phi_f^N | T_U^{\mathcal{S}N} | \Phi_i^N \boldsymbol{k}_i^{(+)} \rangle$ is defined for the potential $V_U^{\mathcal{S}N}(\theta) = V^{\mathcal{S}N}(\theta) - U_0$. The

physical T-matrix $T^{\mathcal{SN}}$ is extracted via the relation [73]

$$\langle \boldsymbol{q}_f^{(-)}\Phi_f^N|T^{\mathcal{SN}}|\Phi_i^N\boldsymbol{q}_i^{(+)}\rangle \equiv \langle \boldsymbol{q}_f^{(-)}\Phi_f^N|V^{\mathcal{SN}}|\psi_i^{\mathcal{SN}(+)}\rangle$$
$$= \langle \boldsymbol{k}_f^{(-)}\Phi_f^N|T_U^{\mathcal{SN}}|\Phi_i^N\boldsymbol{k}_i^{(+)}\rangle + \delta_{f,i}\langle \boldsymbol{k}_f^{(-)}|U_0|\boldsymbol{q}_i^{(+)}\rangle, \quad (83)$$

where $|\boldsymbol{q}^{(\pm)}\rangle$ refers to a Coulomb wave function for an ionic target or a plane-wave for a neutral target. The resulting on-shell T-matrix elements are physical and are used to calculate body-frame scattering amplitudes. Note that although V-matrix elements in equation (81) have a dependence on an arbitrary θ, the resultant on-shell T-matrix elements do not.

4.3. Solving the coupled Lippmann–Schwinger equation

A partial-wave expansion of the projectile wave function allows the three-dimensional Lippmann–Schwinger equation (81) to be solved in effectively one-dimension. The distorted-wave partial-wave expansion is

$$|\boldsymbol{k}^{(\pm)}\rangle = \sqrt{\frac{2}{\pi}}\frac{1}{kr}\sum_{L,M}^{\infty} i^L \mathrm{e}^{\pm \mathrm{i}(\sigma_L+\delta_L)} u_L\,(r;\,k;\,Z_{\mathrm{Ion}})\,Y_{LM}(\hat{\boldsymbol{r}})\,Y_{LM}^*(\hat{\boldsymbol{k}})\,\chi_{m_s}(\sigma), \quad (84)$$

where $\boldsymbol{k}$ is the linear momentum vector and σ_L and δ_L are the Coulomb and distorting phase shifts respectively. Angular terms in the matrix elements of the Lippmann–Schwinger equation can now be evaluated analytically. This allows us to perform accurate, large-scale multichannel calculations and minimises computational resources required.

Utilising the partial-wave expansion of the projectile wave function (84) and analysing the V-matrix elements $\langle \boldsymbol{k}_f^{(-)}\Phi_f^N|V_U^{\mathcal{SN}}(\theta)|\Phi_i^N\boldsymbol{k}_i^{(\pm)}\rangle$ in the Lippmann–Schwinger equation (81), it can be shown that symmetric linear molecules and their isotopologues conserve the scattering system total electronic orbital angular momentum projection $\mathcal{M}$, parity Π and spin $\mathcal{S}$, where

$$\mathcal{M} = m_i + M_i = \ m_f + M_f,$$
$$\Pi = \pi_i \times (-1)^{L_i} = \pi_f \times (-1)^{L_f},$$
$$\mathcal{S} = |s_i \pm 1/2| = |s_f \pm 1/2|,$$

maximum total orbital angular momentum projection $\mathcal{M}_{\max}$, where $-\mathcal{M}_{\max} \leqslant \mathcal{M} \leqslant \mathcal{M}_{\max}$. The same method is also applicable to scattering from heterogeneous linear molecules, however the T- and V-matrix elements will not have conservation in the total parity Π.

The partial-wave expansion of the V- (or T-) matrix for an incident electron with orbital angular momentum L_i and orbital angular projection M_i has the form

$$\langle \boldsymbol{k}_f^{(-)}\Phi_f^N|V_U^{\mathcal{SN}}(\theta)|\Phi_i^N\boldsymbol{k}_i^{(\pm)}\rangle = (k_f k_i)^{-1}$$
$$\times \sum_{\substack{L_f,L_i\\M_f,M_i}}^{L_{\max},M_{\max}} i^{L_i-L_f}\mathrm{e}^{\mathrm{i}(\sigma_{L_f}+\delta_{L_f}\pm\sigma_{L_i}\pm\delta_{L_i})}$$
$$\times V^{\mathcal{M}\Pi\mathcal{S}}_{fL_fM_f,iL_iM_i}(k_f,\,k_i)\,Y_{L_fM_f}(\hat{\boldsymbol{k}}_f^{(\mathrm{b})})\,Y^*_{L_iM_i}(\hat{\boldsymbol{k}}_i^{(\mathrm{b})}), \quad (85)$$

or alternatively as

$$V^{\mathcal{M}\Pi\mathcal{S}}_{fL_fM_f,iL_iM_i}(k_f,\,k_i) = (k_f k_i) i^{L_f-L_i}\mathrm{e}^{-\mathrm{i}(\sigma_{L_f}+\delta_{L_f}\pm\sigma_{L_i}\pm\delta_{L_i})}$$
$$\times \int \mathrm{d}\hat{\boldsymbol{k}}_f \int \mathrm{d}\hat{\boldsymbol{k}}_i\, Y^*_{L_fM_f}(\hat{\boldsymbol{k}}_f^{(\mathrm{b})})\,Y_{L_iM_i}(\hat{\boldsymbol{k}}_i^{(\mathrm{b})})$$
$$\times \langle \boldsymbol{k}_f^{(-)}\Phi_f^N|V_U^{\mathcal{SN}}(\theta)|\Phi_i^N\boldsymbol{k}_i^{(\pm)}\rangle, \quad (86)$$

where $V^{\mathcal{M}\Pi\mathcal{S}}_{fL_fM_f,iL_iM_i}(k_f,\,k_i)$ are the real V-matrix elements evaluated in appendix C, and $\hat{\boldsymbol{k}}^{(\mathrm{b})}$ refers to the electron momentum vector in the body-frame. Substituting equation (85) into the Lippmann–Schwinger equation (81), complex phases $i^{L_i-L_f}\mathrm{e}^{\mathrm{i}(\sigma_{L_f}+\delta_{L_f}\pm\sigma_{L_i}\pm\delta_{L_i})}$, constants $(k_f k_i)^{-1}$ and angular functions $Y_{L_fM_f}(\hat{\boldsymbol{k}}_f^{(\mathrm{b})})\,Y^*_{L_iM_i}(\hat{\boldsymbol{k}}_i^{(\mathrm{b})})$ can be factored out. Performing the integration over $\mathrm{d}\hat{k}$ in the Lippmann–Schwinger equation (81), the partial-wave Lippmann–Schwinger equation for the distorted-wave T-matrix can be written as

$$T^{\mathcal{M}\Pi\mathcal{S}}_{fL_fM_f,iL_iM_i}(k_f,\,k_i) = V^{\mathcal{M}\Pi\mathcal{S}}_{fL_fM_f,iL_iM_i}(k_f,\,k_i) + \sum_{n=1}^{N}\sum_{L',M'}^{L_{\max},M_{\max}} \not\int \mathrm{d}k \frac{V^{\mathcal{M}\Pi\mathcal{S}}_{fL_fM_f,nL'M'}(k_f,\,k)\,T^{\mathcal{M}\Pi\mathcal{S}}_{nL'M',iL_iM_i}(k,\,k_i)}{E^{(+)} - \varepsilon_k - \varepsilon_n^N + i0}. \quad (87)$$

and m, π and s denote the electronic target state orbital angular momentum projection, parity and spin respectively. In practice the sum in the partial-wave expansion of the projectile (84) is taken to a maximum orbital angular momentum $L_{\max}$ and projection $M_{\max}$. CCC scattering calculations include all possible channels of total spin $\mathcal{S}$, (odd and even) parity Π up to the

The Lippmann–Schwinger equation (87) has been efficiently solved for scattering from atomic and ionic targets [54, 73, 74], and here the same standard techniques are utilised. The loss of total angular momentum conservation in equation (87) is the major difference between solving equation (87) for molecules and atoms.

Evaluating the singularity in equation (87) analytically, it becomes

$$T^{\mathcal{M}\Pi\mathcal{S}}_{fL_fM_f,iL_iM_i}(k_f,k_i) = V^{\mathcal{M}\Pi\mathcal{S}}_{fL_fM_f,iL_iM_i}(k_f,k_i) + \sum_{n=1}^{N}\sum_{L',M'}^{L_{\max},M_{\max}} \mathcal{P}\!\!\!\!\!\!\int_k \mathrm{d}k \frac{V^{\mathcal{M}\Pi\mathcal{S}}_{fL_fM_f,nL'M'}(k_f,k)T^{\mathcal{M}\Pi\mathcal{S}}_{nL'M',iL_iM_i}(k,k_i)}{E^{(+)}-\varepsilon_k-\varepsilon_n} - \mathrm{i}\pi\sum_{n=1}^{N_0}\sum_{L',M'}^{L_{\max},M_{\max}} k_n^{-1}V^{\mathcal{M}\Pi\mathcal{S}}_{fL_fM_f,nL'M'}(k_f,k_n)T^{\mathcal{M}\Pi\mathcal{S}}_{nL'M',iL_iM_i}(k_n,k_i), \tag{88}$$

where $\mathcal{P}$ indicates the integral is of principal value type, the total energy is $E=\varepsilon_i+\varepsilon_{k_i}=\varepsilon_f+\varepsilon_{k_f}$, and the on-shell momentum $k_n=\sqrt{2(E-\varepsilon_n)}$ is always real. N_0 is the number of open states; a state is open if $\varepsilon_n \leqslant E$. To obtain a symmetric, unitary T-matrix and to save on computational resources, the K-matrix formulation is introduced to solve (88) using real arithmetic

$$K^{\mathcal{M}\Pi\mathcal{S}}_{nLM,iL_iM_i}(k_n,k_i) = \sum_{n'=1}^{N_0}\sum_{L',M'}^{L_{\max},M_{\max}} T^{\mathcal{M}\Pi\mathcal{S}}_{nLM,n'L'M'}(k_n,k_{n'}) \times (\delta_{n_i,n'}\delta_{L_i,L'}\delta_{M_i,M'} + \mathrm{i}\pi k_{n'}^{-1}K^{\mathcal{M}\Pi\mathcal{S}}_{n'L'M',iL_iM_i}(k_{n'},k_i)). \tag{89}$$

Summing over all initial channels in (88), performing some algebra and substituting (89), one obtains

$$K^{\mathcal{M}\Pi\mathcal{S}}_{fL_fM_f,iL_iM_i}(k_f,k_i) = V^{\mathcal{M}\Pi\mathcal{S}}_{fL_fM_f,iL_iM_i}(k_f,k_i) + \sum_{n=1}^{N}\sum_{L',M'}^{L_{\max},M_{\max}} \mathcal{P}\!\!\!\!\!\!\int_k \mathrm{d}k \frac{V^{\mathcal{M}\Pi\mathcal{S}}_{fL_fM_f,nL'M'}(k_f,k)K^{\mathcal{M}\Pi\mathcal{S}}_{nL'M',iL_iM_i}(k,k_i)}{E^{(+)}-\varepsilon_k-\varepsilon_n^N}. \tag{90}$$

Letting the indices i and f refer to channels $(n_im_i\pi_is_i,\ k_iL_iM_i)$ and $(n_fm_f\pi_fs_f,\ k_fL_fM_f)$, respectively, the coupled integral equations are solved by replacing the integrand with a quadrature rule

$$K^{\mathcal{M}\Pi\mathcal{S}}_{fi} = V^{\mathcal{M}\Pi\mathcal{S}}_{fi} + \sum_{n=1} w_n V^{\mathcal{M}\Pi\mathcal{S}}_{fn}K^{\mathcal{M}\Pi\mathcal{S}}_{ni}, \tag{91}$$

where, w_n contain the Gaussian type weights divided by the Green's function denominator (energy terms) and n now runs over all combinations of off-shell momentum quadrature (k-grid) points and channels ($nm\pi s,\ kL'M'$) for a particular partial-wave. Given that the integrand contains a singularity at different energies for open channels, the zero-to-infinity integration interval is typically broken into regions such that the singularity can be managed using an even number of Gaussian quadrature points arranged symmetrically around the singularity. The remaining finite intervals are then managed by other Gaussian quadratures, with the final interval to infinity managed via a power transformation law. In addition, the bound states of the projectile are included as extra quadrature points with weight $w_n=1$ in equation (91), for more details see [73]. Equation (91) is rearranged to form a linear system of equations $Ax=b$ by letting channels f run over the same range as n. This is indicated by replacing index f with n'. Equation (91) is now rearranged in the form

$$\sum_{n=1}(\delta_{n',n} - w_nV^{\mathcal{M}\Pi\mathcal{S}}_{n'n})K^{\mathcal{M}\Pi\mathcal{S}}_{ni} = V^{\mathcal{M}\Pi\mathcal{S}}_{n'i}. \tag{92}$$

Equation (92) is solved for the half-on-shell K-matrix elements $K^{\mathcal{M}\Pi\mathcal{S}}_{ni}$ using a standardised linear equation solver, such as SCALAPACK. Substitution of $K^{\mathcal{M}\Pi\mathcal{S}}_{ni}$ into equation (91) allows for the on-shell solution $K^{\mathcal{M}\Pi\mathcal{S}}_{fi}$. The real on-shell K-matrix elements are then used to solve the linear system of equations for the complex distorted-wave T-matrix elements via equation (89)

$$\sum_{n=1}^{N_0}(\delta_{n,i}+\mathrm{i}\pi k_nK^{\mathcal{M}\Pi\mathcal{S}}_{ni})T^{\mathcal{M}\Pi\mathcal{S}}_{fn} = K^{\mathcal{M}\Pi\mathcal{S}}_{fi}, \tag{93}$$

here n is the on-shell channels ($nm\pi s,\ k_nL'M'$) and N_0 is the total number of open on-shell channels. Incidentally, an alternative to this numerical treatment of the Green's function has been developed using an analytical approach for atoms [75, 76] and ions [77]. It will be extended to molecular targets in due course.

From equation (83) the distorted-wave T-matrix elements are used to obtain physical ($U_0=0$) T-matrix elements $T^{\mathcal{M}\Pi\mathcal{S}}_{fL_fM_f,iL_iM_i}(q_f,q_i)$, which in the partial-wave form is given by

$$T^{\mathcal{M}\Pi\mathcal{S}}_{fL_fM_f,iL_iM_i}(q_f,q_i) = T^{\mathcal{M}\Pi\mathcal{S}}_{fL_fM_f,iL_iM_i}(k_f,k_i)\mathrm{e}^{\mathrm{i}(\delta_{L_i}+\delta_{L_f})} - \delta_{f,i}\delta_{L_f,L_i}\delta_{M_f,M_i}q_i\pi^{-1}\mathrm{e}^{\mathrm{i}\delta_{L_i}}\sin(\delta_{L_i}), \tag{94}$$

where q is the linear momentum of the projectile and indicates the physical T-matrix elements. The physical T-matrix can then be expressed as

$$\langle \boldsymbol{q}_f^{(-)}\Phi_f^N|T^{\mathcal{S}N}|\Phi_i^N\boldsymbol{q}_i^{(+)}\rangle = (q_fq_i)^{-1}\sum_{\substack{L_f,L_i\\M_f,M_i}}^{L_{\max},M_{\max}} i^{L_i-L_f}\mathrm{e}^{\mathrm{i}(\sigma_{L_i}+\sigma_{L_f})} \times T^{\mathcal{M}\Pi\mathcal{S}}_{fL_fM_f,iL_iM_i}(q_f,q_i)Y_{L_fM_f}(\hat{\boldsymbol{q}}_f^{(\mathrm{b})})Y^*_{L_iM_i}(\hat{\boldsymbol{q}}_i^{(\mathrm{b})}). \tag{95}$$

This physical body-frame T-matrix is used to obtain the laboratory-frame scattering amplitudes defined in equations (35)–(37). For electronically homogeneous diatomic molecules the partial-wave term $A^{\mathcal{S}(\mathrm{b})}_{fL_fM_f,iL_iM_i}(R)$ utilised in equations (33), (35)–(37) is more appropriately replaced by

$$A^{\mathcal{M}\Pi\mathcal{S}(\mathrm{b})}_{fL_fM_f,iL_iM_i}(R) = -(2\pi)^2(q_fq_i)^{-1}i^{L_i-L_f} \times \mathrm{e}^{\mathrm{i}(\sigma_{L_i}+\sigma_{L_f})}T^{\mathcal{M}\Pi\mathcal{S}(\mathrm{b})}_{fL_fM_f,iL_iM_i}(q_f,q_i;R), \tag{96}$$

where $T^{\mathcal{M}\Pi\mathcal{S}(\mathrm{b})}_{fL_fM_f,iL_iM_i}(q_f,q_i;R) \equiv T^{\mathcal{M}\Pi\mathcal{S}}_{fL_fM_f,iL_iM_i}(q_f,q_i)$ in equations (94) and (95).

4.4. Choice of the short-ranged distorting potential U_0

Projectile wave functions with large values of momentum k are highly oscillatory and hence can lead to a loss of accuracy in the calculation of the V-matrix elements $\langle \boldsymbol{k}_f^{(-)}\Phi_f^N|V_U^{\mathcal{S}N}(\theta)|\Phi_i^N\boldsymbol{k}_i^{(\pm)}\rangle$. As Z increases, the projectile-nuclei term V_0 in equation (79) is responsible for making V-matrix elements with larger values of k to become more important. To effectively deal with this numerical issue, a short-ranged distorting potential U_0 is chosen such that it cancels the spherical part of the V_0 potential. Using the antisymmetrisation property of the target states, the

distorting potential can be written as

$$U_0 = 2z_0 Z v_0(r_0, R/2) - \frac{z_0 Z_{\rm Ion}}{r_0} - z_0 N_{\rm e} \int {\rm d}^3 r |\Phi_n(\boldsymbol{r})|^2 v_0(r_0, r_1), \quad (97)$$

where $\boldsymbol{r}$ is collectively all target electronic spatial coordinates, n is typically the electronic ground state and $v_0(r_0, r_1)$ is defined in equation (51). This form of U_0 is spherically symmetric, short-ranged and ensures the shortest-range V-matrix elements by removing the projectile-nuclei term V_0 for the $\lambda = 0$ partial-wave (referring to equation (50)). The use of a distorting potential is a purely numerical technique which saves on computational resources when solving the integral in equation (81). Results of $T^{\mathcal{SN}}$ from equation (83) must be independent of U_0.

5. ABS (top-up) technique

The direct-potential V-matrix can be calculated without the infinite series partial-wave expansion of the projectile (84) by applying the Bethe-formula [78], which allows analytic integration over the projectile coordinate space. Here the plane-wave ABS technique is applied to both charged and neutral targets for inelastic-scattering only, hence by orthogonality of the target states the matrix elements of the non-spherical potential V_0 and asymptotic potential $\frac{z_0 Z_{\rm Ion}}{r_0}$ are zero. The ABS technique is not used for elastic scattering because in a close-coupling calculation the elastic cross section converges quickly with respect to the partial-wave expansion. Also to describe elastic scattering the effect of dipole polarisation must be included [79], which comes in at the second-order Born approximation.

Note that in the present formulation the target states are defined in the body-frame of reference. Therefore we have chosen to evaluate the Born matrix elements in the body-frame. The analytic Born body-frame scattering amplitude is formulated and then transformed to the lab-frame.

Writing out the direct-potential V-matrix for inelastic-scattering and substituting plane waves normalised in momentum space (with the normalisation constant $(2\pi)^{-3/2}$)

$$\langle \boldsymbol{q}_f \Phi_f | \sum_{j=1}^{N_{\rm e}} V_{0j} | \Phi_i \boldsymbol{q}_i \rangle = -\frac{1}{(2\pi)^3} \delta_{s_f, s_i} \times \sum_{j=1}^{N_{\rm e}} \int {\rm d}\boldsymbol{r} \Phi_f(\boldsymbol{r}) \Phi_i(\boldsymbol{r}) \int {\rm d}\boldsymbol{r}_0 {\rm e}^{{\rm i}\boldsymbol{Q}\cdot\boldsymbol{r}_0} \frac{z_0}{|\boldsymbol{r}_0 - \boldsymbol{r}_j|}, \quad (98)$$

where $\boldsymbol{r}$ represents all target electrons spatial coordinates collectively and $\boldsymbol{Q} = \boldsymbol{q}_i - \boldsymbol{q}_f$. Utilising the Bethe-formula [78]

$$\int {\rm d}\boldsymbol{r}_0 {\rm e}^{{\rm i}\boldsymbol{Q}\cdot\boldsymbol{r}_0} \frac{z_0}{|\boldsymbol{r}_0 - \boldsymbol{r}_j|} = \frac{4\pi z_0}{Q^2} {\rm e}^{{\rm i}\boldsymbol{Q}\cdot\boldsymbol{r}_j}, \quad (99)$$

and the multipole expansion, equation (98) becomes

$$\langle \boldsymbol{q}_f \Phi_f | \sum_{j=1}^{N_{\rm e}} V_{0j} | \Phi_i \boldsymbol{q}_i \rangle = -\frac{N_{\rm e} z_0}{2Q^2 \pi^2} \delta_{s_f, s_i} \times \int {\rm d}\boldsymbol{r} \Phi_f(\boldsymbol{r}) {\rm e}^{{\rm i}\boldsymbol{Q}\cdot\boldsymbol{r}_1} \Phi_i(\boldsymbol{r}). \quad (100)$$

To carry out analytic integration over the angular terms in equation (100) the exponential term ${\rm e}^{{\rm i}\boldsymbol{Q}\cdot\boldsymbol{r}_1}$ is expanded in partial-wave form

$${\rm e}^{{\rm i}\boldsymbol{Q}\cdot\boldsymbol{r}_1} = 4\pi \sum_{\lambda\mu}^{\infty} i^\lambda j_\lambda(Qr_1) Y^*_{\lambda\mu}(\hat{\boldsymbol{Q}}) Y_{\lambda\mu}(\hat{\boldsymbol{r}}_1). \quad (101)$$

Substituting (101) into equation (100), the analytic Born matrix elements (labelled by superscript $^{\rm (AB)}$) are conveniently expressed as

$$\langle \boldsymbol{q}_f \Phi_f | \sum_{j=1}^{N_{\rm e}} V_{0j} | \Phi_i \boldsymbol{q}_i \rangle = \sum_{\lambda\mu} i^\lambda V^{\rm (AB)}_{\substack{f,i \\ \lambda\mu}}(Q) Y^*_{\lambda\mu}(\hat{\boldsymbol{Q}}). \quad (102)$$

For H_2^+ the analytic Born matrix elements $V^{\rm (AB)}_{\substack{f,i \\ \lambda\mu}}(Q)$ have the form

$$V^{\rm (AB)}_{\substack{f,i \\ \lambda\mu}}(Q) = -(-1)^\lambda \frac{z_0 \hat{\lambda}}{Q^2 \pi^{3/2}} \sum_{\alpha\gamma} C^{(f)}_\alpha C^{(i)}_\gamma C^{l_\gamma 0}_{l_\alpha 0, \lambda 0} \times C^{l_\alpha m_\alpha}_{l_\gamma m_\gamma, \lambda\mu} \int_0^\infty {\rm d}r_1 \varphi_\alpha(r_1) j_\lambda(Qr_1) \varphi_\gamma(r_1), \quad (103)$$

while for H_2

$$V^{\rm (AB)}_{\substack{f,i \\ \lambda\mu}}(Q) = -(-1)^\lambda \frac{2 z_0 \hat{\lambda}}{Q^2 \pi^{3/2}} \delta_{s_f, s_i} \sum_{\alpha\beta\gamma\delta} C^{(f)}_{\alpha,\beta} C^{(i)}_{\gamma,\delta} \times \langle \phi_\beta | \phi_\delta \rangle C^{l_\gamma 0}_{l_\alpha 0, \lambda 0} C^{l_\alpha m_\alpha}_{l_\gamma m_\gamma, \lambda\mu} \times \int_0^\infty {\rm d}r_1 \varphi_\alpha(r_1) j_\lambda(Qr_1) \varphi_\gamma(r_1). \quad (104)$$

Noting the Clebsch–Gordan coefficient triangle rules and the one-electron orbital overlaps (B.8) (i.e. $\delta_{m_\beta, m_\delta}$), $V^{\rm (AB)}_{\substack{f,i \\ \lambda\mu}}(Q)$ in equations (103) and (104) must have $\mu = m_f - m_i$ so that $V^{\rm (AB)}_{\substack{f,i \\ \lambda\mu}}(Q)$ is non-zero.

5.1. Analytic Born orientation averaged DCS

In the above section the analytic Born matrix elements (100) were evaluated in the body-frame. Following from the definition of the body-frame scattering amplitude in equation (33), and noting the definition of the first-Born approximation

$$\langle \boldsymbol{q}_f^{(-)} \Phi_f | T | \Phi_i \boldsymbol{q}_i^{(+)} \rangle = \langle \boldsymbol{q}_f \Phi_f | \tilde{V} | \Phi_i \boldsymbol{q}_i \rangle, \quad (105)$$

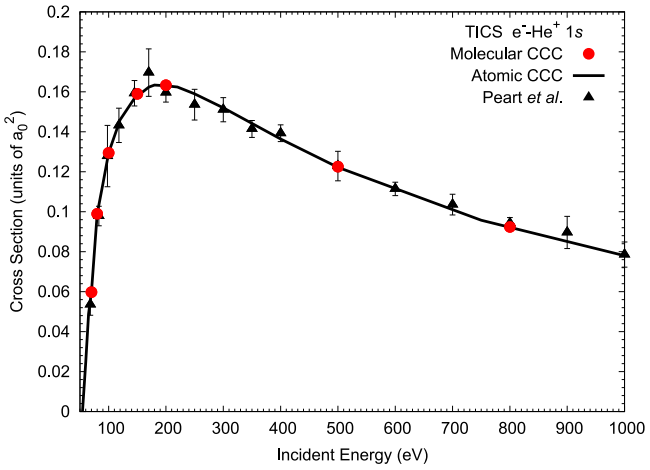

Figure 1. Total ionisation cross section (TICS) of electron scattering from the He^+ ground state. The molecular CCC calculations for the united atom limit ($R = 0\ a_0$) of H_2^+ are compared with the atomic CCC code calculations [81] and the measurements of Peart *et al* [82].

the analytic Born body-frame scattering amplitude for the transition $iv_i \rightarrow fv_f$ is conveniently expressed as

$$F^{(\mathrm{AB})}_{fv_f,iv_i}(\Omega^{(\mathrm{b})}) = \sum_{\lambda\mu} \langle \nu_{fv_f} | A^{(\mathrm{AB})}_{\substack{f,i \\ \lambda\mu}}(Q^{(\mathrm{b})}) | \nu_{iv_i} \rangle_R \, Y^*_{\lambda\mu}(\hat{\boldsymbol{Q}}^{(\mathrm{b})}), \tag{106}$$

where $\tilde{V}$ denotes the direct potential between the projectile and the target

$$\tilde{V} = V_0 + \sum_{j=1}^{N_e} V_{0j} - \frac{z_0 Z_{\mathrm{Ion}}}{r_0}, \tag{107}$$

superscript $^{(\mathrm{b})}$ indicates the body-frame of reference,

$$A^{(\mathrm{AB})}_{\substack{f,i \\ \lambda\mu}}(Q^{(\mathrm{b})}; R) = -(2\pi)^2 i^\lambda V^{(\mathrm{AB})}_{\substack{f,i \\ \lambda\mu}}(Q^{(\mathrm{b})}; R) \tag{108}$$

and $V^{(\mathrm{AB})}_{\substack{f,i \\ \lambda\mu}}(Q^{(\mathrm{b})}; R)$ is the body-frame fixed-nuclei analytic Born matrix elements defined in equations (103) and (104). Note that due to the orthogonality of the target states, the first and last term of the interaction potential (107) do not contribute to inelastic transitions.

To transform the analytic Born body-frame scattering amplitude $F^{(\mathrm{AB})}_{fv_f,iv_i}(\Omega^{(\mathrm{b})})$ to the lab-frame, $\hat{\boldsymbol{q}}_i^{(\mathrm{lab})}$ is rotated so that $\hat{\boldsymbol{q}}_i^{(\mathrm{lab})}$ is aligned with the body-frame z-axis. The definition in equation (34) is again utilised such that

$$Y^*_{\lambda\mu}(\hat{\boldsymbol{Q}}^{(\mathrm{b})}) = \sum_\rho D^{\lambda *}_{\rho,\mu}(\hat{\boldsymbol{R}}^{(\mathrm{lab})}) Y^*_{\lambda\rho}(\hat{\boldsymbol{Q}}^{(\mathrm{lab})}), \tag{109}$$

where in the lab-frame of reference the angle $\hat{\boldsymbol{Q}}^{(\mathrm{lab})}$ with respect to the lab-frame z-axis (or $\hat{\boldsymbol{q}}_i^{(\mathrm{lab})}$) is

$$\theta^{(\mathrm{lab})}_{\boldsymbol{Q}} = \arccos\left((q_i - q_f \cos(\theta^{(\mathrm{lab})}_{\hat{\boldsymbol{q}}_f}))\Big/ Q^{(\mathrm{lab})}\right) \tag{110}$$

and $\theta^{(\mathrm{lab})}_{\hat{\boldsymbol{q}}_f}$ is the angle between the $\hat{\boldsymbol{q}}_i^{(\mathrm{lab})}$ and $\hat{\boldsymbol{q}}_f^{(\mathrm{lab})}$, as well as the angle between $\hat{\boldsymbol{q}}_i^{(\mathrm{b})}$ and $\hat{\boldsymbol{q}}_f^{(\mathrm{b})}$. $|\boldsymbol{Q}|$ has the same form in both the body- and lab-frames of reference

$$\begin{aligned} Q = Q^{(\mathrm{b})} = Q^{(\mathrm{lab})} &= |\boldsymbol{Q}| = |\boldsymbol{q}_i - \boldsymbol{q}_f| \\ &= \sqrt{q_i^2 + q_f^2 - 2\boldsymbol{q}_i \cdot \boldsymbol{q}_f}\,, \end{aligned} \tag{111}$$

where vectors $\boldsymbol{q}_i$ and $\boldsymbol{q}_f$ are in the same frame as $\boldsymbol{Q}$. The analytic Born lab-frame scattering amplitude is now defined as

$$\begin{aligned} F^{(\mathrm{AB})}_{fv_f,iv_i}(\Omega^{(\mathrm{lab})}, \hat{\boldsymbol{R}}^{(\mathrm{lab})}) = \sum_{\lambda\mu} &\langle \nu_{fv_f} | A^{(\mathrm{AB})}_{\substack{f,i \\ \lambda\mu}}(Q^{(\mathrm{b})}) | \nu_{iv_i} \rangle_R \\ &\times \sum_\rho D^{\lambda *}_{\rho,\mu}(\hat{\boldsymbol{R}}^{(\mathrm{lab})}) Y^*_{\lambda\rho}(\hat{\boldsymbol{Q}}^{(\mathrm{lab})}). \end{aligned} \tag{112}$$

The analytic Born DCS is obtained by substituting $F^{(\mathrm{AB})}_{fv_f,iv_i}(\Omega^{(\mathrm{lab})}, \hat{\boldsymbol{R}}^{(\mathrm{lab})})$ into the orientation averaged DCS equation (38). The final form of the analytic Born DCS is

$$\frac{\mathrm{d}\sigma^{(\mathrm{AB})}_{fv_f,iv_i}}{\mathrm{d}\Omega^{(\mathrm{lab})}} = \frac{q_f}{q_i}\frac{1}{4\pi} \sum_{\lambda\mu} |\langle \nu_{fv_f} | A^{(\mathrm{AB})}_{\substack{f,i \\ \lambda\mu}}(Q^{(\mathrm{b})}) | \nu_{iv_i} \rangle_R|^2. \tag{113}$$

For a full derivation of the analytic Born DCS orientation averaging procedure see appendix A. The orientation averaged integrated cross sections are calculated by numerically integrating over $\theta^{(\mathrm{lab})}_{\hat{\boldsymbol{q}}_f}$, noting that $Q^{(\mathrm{b})}$ is dependent upon $\theta^{(\mathrm{lab})}_{\hat{\boldsymbol{q}}_f}$ (refer to equation (111) and preceding discussion).

5.2. ABS method

The ABS method is generally used to top-up partial-wave differential and integrated cross sections. Here the ABS method is used for integrated cross sections. In our recent e^-–H_2 scattering paper [48] we describe the ABS technique utilised for topping-up DCS.

Utilising the Born subtraction method, orientationally averaged fixed-nuclei inelastic integrated cross sections are calculated via

$$\sigma^{\mathcal{S}}_{f,i} = \sum_{\mathcal{M}\Pi}^{\mathcal{M}_{\max}} (\sigma^{\mathcal{M}\Pi\mathcal{S}}_{f,i} - \tilde{\sigma}^{\mathcal{M}\Pi}_{f,i}) + \sigma^{(\mathrm{AB})}_{f,i}, \tag{114}$$

where the orientationally averaged fixed-nuclei partial-wave (close-coupling) integrated cross section $\sigma^{\mathcal{M}\Pi\mathcal{S}}_{f,i}$ is calculated with equations (44) and (96). The orientationally averaged partial-wave Born integrated cross section $\tilde{\sigma}^{\mathcal{M}\Pi}_{f,i}$ is calculated with equations (44) and (96) but with $e^{i(\sigma_{L_i}+\sigma_{L_f})} T^{\mathcal{M}\Pi\mathcal{S}}_{fL_fM_f,iL_iM_i}(q_f, q_i)$ replaced by $\tilde{V}^{\mathcal{M}\Pi}_{fL_fM_f,iL_iM_i}(q_f, q_i)$ (refer to equations (95), (105) and (107)). Orientationally averaged analytic Born integrated cross sections $\sigma^{(\mathrm{AB})}_{f,i}$ are calculated from the analytic Born DCS (113) via numerical integration over $\theta^{(\mathrm{lab})}_{\hat{\boldsymbol{q}}_f}$.

6. Convergence studies

In [80] we gave a detailed discussion of convergence studies within the (atomic and molecular) CCC method and demonstrated convergence (accurate to within numerical accuracy; approximately better than 5%) of the major positron–H_2

scattering cross sections. The reader is referred to [80] for the full details of checking convergence in CCC calculations and [45] for discussion on uncertainty estimates in atomic and molecular data.

Here we demonstrate convergence of the electron–H_2^+ cross sections within the fixed-nuclei approximation. However, first we demonstrate the accuracy of the molecular CCC code by performing calculations in the unified atom limit ($R = 0\ a_0$) of H_2^+, which by omitting the internuclear Coulomb repulsion term $1/R$ in equation (46) is equivalent to modelling He^+.

6.1. Unified atom limit test for e^-–He^+

The accuracy of the molecular CCC calculations is demonstrated by comparing $R = 0\ a_0$ results with the atomic CCC code results for electron–He^+ scattering [81]. The difference between the two codes is that the atomic CCC calculations conserve total orbital angular momentum $\mathcal{J}$, total orbital angular momentum projection $\mathcal{M}$, parity Π and spin $\mathcal{S}$, while molecular calculations conserve total orbital angular momentum projection $\mathcal{M}$, parity Π and spin $\mathcal{S}$. Consequently the formulation of the atomic and electronic molecular target states, V-matrix elements and the set of coupled equations are very different. Here the atomic and molecular CCC calculations both use the same size Laguerre basis with $N_l = 15 - l$, $l_{\max} = 4$ and Laguerre functions with exponential fall-offs $\alpha_l = 1.4$. The atomic code diagonalisation generated 65 states, while the molecular code produced 305 states. Atomic CCC calculations were performed up to $\mathcal{J} = 15$ for both singlet and triplet spin $\mathcal{S}$. The molecular CCC calculations were performed with a projectile partial-wave expansion with maximum orbital angular momentum $L_{\max} = 8$. The singlet and triplet spin $\mathcal{S}$, odd and even parity Π and maximum total orbital angular projection $\mathcal{M}_{\max} = 8$ channels were included. Both codes use the ABS method to top-up the partial-wave expansion. TICSs of electron scattering from the ground-state of He^+ are presented in figure 1. The atomic and molecular CCC code results are compared with the experimental measurements of Peart *et al* [82] and are in excellent agreement with each other and experiment across the entire energy range.

6.2. Convergence of e^-–H_2^+ cross sections with the number of states

For electron scattering from H_2^+ and its isotopologues the major scattering processes (above 10 eV) are DE (12) and (13), and DI (17). In experiment the proton production (PP) cross section is measured as $\sigma_{PP} = \sigma_{DE} + 2\sigma_{DI}$. Almost all electronically exited states of H_2^+ are repulsive and excitation from the ground state to the electronically excited states leads to dissociation of the molecule (within the adiabatic-nuclei approximation). We have assumed that the DE cross section measured by experiment is the sum of all electronic excitation cross sections. This is a generally accepted approximation [83–85] for collision energies (above 10 eV), where the direct DE cross section is dominant compared to the resonant DE cross section [86].

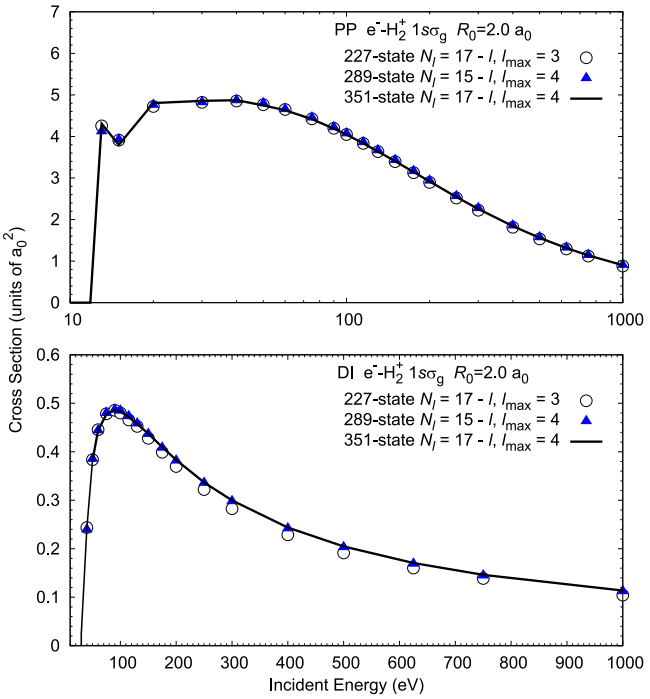

Figure 2. Convergence studies of electron scattering from H_2^+ at the equilibrium distance $R_0 = 2.0\ a_0$. 351-, 289- and 227-state CCC calculations are presented for the proton production (PP) and dissociative ionisation (DI) cross section. Target states are calculated with N_l Laguerre basis functions for each orbital angular momentum l up to $l_{\max}$.

For e^-–H_2^+ scattering molecular CCC calculations were conducted over the energy range from 10 to 1000 eV and performed with a projectile partial-wave expansion up to orbital angular momentum $L_{\max} = 9$. All total orbital angular momentum projection $\mathcal{M}$, odd and even parity Π and singlet and triplet spin $\mathcal{S}$ channels were included in the calculation up to $\mathcal{M}_{\max} = 9$. The orientationally averaged ABS method (described in section 5) was used to top-up the partial-wave expansion.

Convergence studies of the close-coupling (target state) expansion are investigated for electron scattering from H_2^+ at the equilibrium distance $R_0 = 2.0\ a_0$. A 351-state CCC calculation is compared with a 289-state and 227-state CCC calculation. Note that these scattering calculations omitted the highest energy pseudostates from the structure models described below. The highest-energy pseudostates in a CCC calculation can usually be omitted without changing the final results as they have a large energy and are normally closed in the scattering calculations. This ensures that high-energy highly oscillatory pseudostates do not result in inaccurate V-matrix elements.

The 351-, 289- and 227-state structure models utilise the molecular orbital method (described in section 3.2) for the $1s\sigma_g$ and $2p\sigma_u$ orbitals, which were produced with a large basis that had $N_l = 60 - l$ functions with $l_{\max} = 9$ and $\alpha_l = 1.4$. These molecular orbitals replace the $1s\sigma_g$ and $2p\sigma_u$ Laguerre basis orbitals in the following models. The 351 states used in the scattering calculation were generated with a second Laguerre basis that had $N_l = 17 - l$, $l_{\max} = 4$

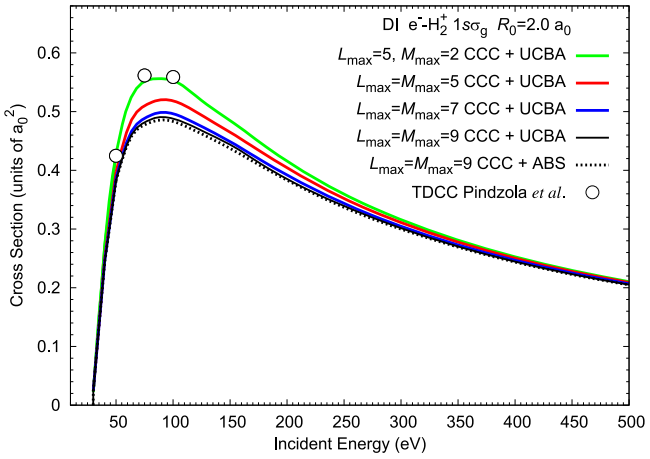

Figure 3. The dissociative ionisation (DI) cross section of electron scattering from H_2^+ at the equilibrium distance $R_0 = 2.0\ a_0$. CCC results are calculated with a partial-wave expansion up to orbital angular momentum $L_{\max}$ and maximum total orbital angular projection $\mathcal{M}_{\max}$ channels are included. CCC results utilise the orientationally averaged analytic Born subtraction (ABS) method to top-up results or the unitarised Coulomb Born approximation (UCBA) method to top-up results to $L_{\max} = \mathcal{M}_{\max} = 16$ and then the ABS method for the higher terms. CCC results are compared with the time-dependent close-coupling (TDCC) results of Pindzola *et al* [87], which used a $L_{\max} = 5$, $\mathcal{M}_{\max} = 2$ model with a distorted-wave top-up to $L_{\max} = \mathcal{M}_{\max} = 16$.

Laguerre basis functions with exponential fall-offs $\alpha_l = 1.4$. This Laguerre basis was also used in the 227-state model, however basis functions were restricted up to $l_{\max} = 3$. The 289-state model was constructed from a Laguerre basis that had $N_l = 15 - l$, $l_{\max} = 4$ and $\alpha_l = 1.4$.

351-, 289- and 227-state molecular CCC calculations are presented in figure 2 for $R_0 = 2.0\ a_0$ PP and DI cross sections. These calculations yield practically the same results and are therefore convergent in N_l and $l_{\max}$. The PP cross section feature at 20 eV is from the newly opened $2p\pi_u$ states contribution to the cross section.

6.3. Convergence of e^-–H_2^+ scattering with the projectile partial-wave expansion

Here convergence of the $R_0 = 2.0\ a_0$ CCC calculations is investigated with respect to the size of the projectile-electron partial-wave expansion and the use of different top-up procedures.

For the DI cross section, TDCC calculations have been performed for $R_0 = 2.0\ a_0$ with a partial-wave expansion up to $L_{\max} = 5$ and included up to $\mathcal{M}_{\max} = 2$ channels [87]. They utilised a distorted-wave top-up for the higher terms up to $L_{\max} = \mathcal{M}_{\max} = 16$. Here we investigate the plane-wave ABS and unitarised Coulomb Born approximation (UCBA) top-up procedures. The UCBA approximates equation (90) as

$$K^{\mathcal{M}\Pi\mathcal{S}}_{fL_fM_f,iL_iM_i}(k_f, k_i) = \tilde{V}^{\mathcal{M}\Pi}_{fL_fM_f,iL_iM_i}(k_f, k_i), \tag{115}$$

where k indicates a distorted Coulomb wave and $\tilde{V}$ indicates the direct part of the interaction potential (107) V-matrix elements.

To test the current top-up procedure, the 351-state CCC results are calculated with different sized partial-wave expansions that utilise the UCBA to top-up results up to $L_{\max} = \mathcal{M}_{\max} = 16$ and the orientationally averaged ABS technique to top-up results for the higher terms ($\mathcal{M}_{\max} > 16$). These results are compared in figure 3 with the TDCC results [87] and 351-state CCC results that utilise just the orientationally averaged ABS method to top-up results. Firstly convergence is achieved for the $L_{\max} = \mathcal{M}_{\max} = 7$ and $L_{\max} = \mathcal{M}_{\max} = 9$ calculations using either the UCBA or ABS top-up procedures. The $L_{\max} = 5$ $\mathcal{M}_{\max} = 2$ CCC results that utilise the UCBA top-up procedure are in excellent agreement with the corresponding TDCC results, however, the TDCC results are approximately 20% larger than the converged CCC results at the cross section peak. For these top-up procedures (ABS and UCBA) there is only a very minor difference in the converged results ($L_{\max} = \mathcal{M}_{\max} = 7$ and $L_{\max} = \mathcal{M}_{\max} = 9$). Therefore the orientationally averaged plane-wave ABS method is sufficiently accurate for close-coupling calculations with a converged partial-wave expansion, as is the case here.

7. Electron scattering from H_2^+ and its isotopologues

Experimentally H_2^+ is produced by electron-impact ionisation of H_2 which leaves H_2^+ in a range of vibrationally excited states. Due to the lack of dipole moment of homonuclear-diatomic molecules, relaxation of these states via dipole transitions is forbidden and they have long lifetimes. Hence measurements of the electron–H_2^+ collision system are generally taken with H_2^+ populated in various vibrationally excited states [88]. To compare with experiment, cross sections are weighted according to the vibrational population of the beam

$$\bar{\sigma}_{f,i} = \sum_{v_i=0}^{N_v} p_{v_i}\,\sigma_{f,iv_i} \Bigg/ \left(\sum_{v_i=0}^{N_v} p_{v_i}\right), \tag{116}$$

where p_{v_i} are the Franck–Condon [42, 70] (FC) or von Busch and Dunn [88] (BD) vibrational distribution weights, N_v is the last vibrational state of the population and σ_{f,iv_i} is calculated using equation (43). In the adiabatic-nuclei approximation, calculations of σ_{f,iv_i} are performed as a post processing of fixed-nuclei scattering results and requires scattering calculations to be conducted at a (large) number of internuclear distances. In the Born–Oppenheimer approximation the results for electron scattering from H_2^+ and its isotopologues can be obtained by using the same fixed-nuclei scattering results in equation (43) with the appropriate vibrational wave functions of the target.

Preliminary CCC results of electron–H_2^+ scattering were published in [89]. The reader is referred to [42] for a detailed literature review and presentation of CCC results for these systems (electron scattering from H_2^+ and its isotopologues). Here we present selected results of these systems: the H_2^+ vibrationally weighted PP and DI cross sections, and the HD^+ vibrationally resolved DE and DI cross sections. These results have also been made available on the LXCat website [90].

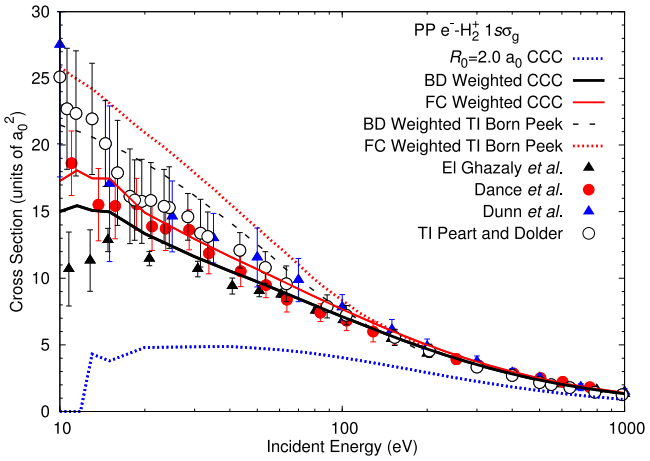

Figure 4. Adiabatic-nuclei CCC calculations of electron scattering from the electronic ground, vibrationally excited states of H_2^+. Franck–Condon (FC) and von Busch and Dunn [88] (BD) vibrationally weighted proton production (PP) cross sections are compared with the CCC $R_0 = 2.0\ a_0$ calculations, vibrationally weighted total inelastic (TI) Born calculations of Peek [85], the TI measurements of Peart and Dolder [91] and the PP experiments of El Ghazaly *et al* [92], Dunn *et al* [84, 93] and Dance *et al* [83].

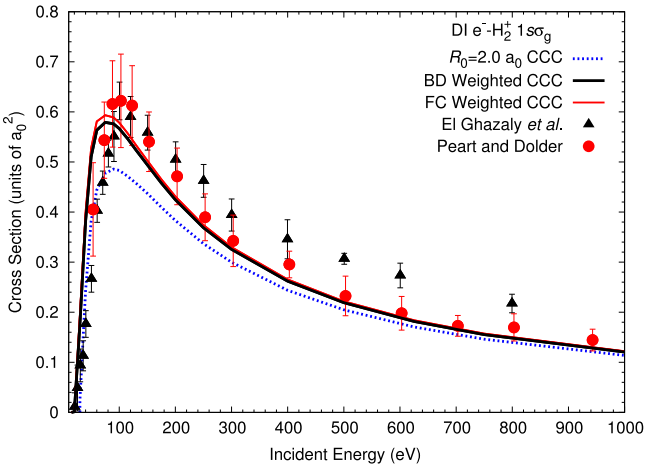

Figure 5. Adiabatic-nuclei CCC calculations of electron scattering from the electronic ground, vibrationally excited states of H_2^+. Franck–Condon (FC) and von Busch and Dunn [88] (BD) vibrationally weighted dissociative ionisation (DI) cross sections are compared with the CCC $R_0 = 2.0\ a_0$ results, and the measurements of Peart and Dolder [96] and El Ghazaly *et al* [92].

7.1. Scattering calculation details

The fixed-nuclei CCC e^-–H_2^+ calculation details were given above in section 6.2. For the 351-state $R_0 = 2.0\ a_0$ model, convergence was demonstrated for the size of the partial-wave expansion ($L_{\max}$ and $\mathcal{M}_{\max}$), number of Laguerre basis functions per l (N_l) and the maximum orbital angular momentum of the basis $l_{\max}$. The 351-state model's first few low-lying target state energies, oscillator strengths and ground static dipole polarisability are presented in [42] as a function of R.

For internuclear separations $R > 5.5\ a_0$, the accuracy of the 351-state CCC (single-centre) structure model deteriorates and is likely to produce unreliable cross sections [42]. However the 351-state model is sufficiently accurate for scattering calculations in the range $0 \leqslant R \leqslant 5.5\ a_0$. 351-state CCC scattering calculations were conducted over a 23 point R grid within the interval $1.2 \leqslant R \leqslant 5.5\ a_0$. Cross sections in this interval for DI and DE cross sections were found to be smooth away from the major excitation thresholds. Cross sections were interpolated and extrapolated across the grid $1.0 \leqslant R \leqslant 18.0\ a_0$, which is the span of the highest excited vibrational levels. Extrapolation outside the interval $1.2 \leqslant R \leqslant 5.5\ a_0$ introduces uncertainty in the vibrationally resolved and weighted cross sections. The procedure used to check the extrapolation method was detailed in [42].

By performing convergence studies, the CCC fixed-nuclei cross sections are estimated to be accurate to within 5%. Vibrationally weighted cross sections are estimated to be accurate within 5% for DI and 10% for PP. PP cross sections have a larger uncertainty estimate due to their higher sensitivity to extrapolation to large R. Note that the vibrational population weighting p_{v_i} also has an associated uncertainty, however, this is dependent on the experiment or application.

7.2. Results

Adiabatic-nuclei CCC results of vibrationally weighted PP cross sections (116) are presented in figure 4 for electron scattering from H_2^+. Adiabatic-nuclei CCC results have been vibrationally weighted according to the BD and FC distributions, and are compared with the CCC $R_0 = 2.0\ a_0$ fixed-nuclei calculations, vibrationally weighted total inelastic (TI) Born cross sections of Peek [85], the TI measurements of Peart and Dolder [91] and the PP measurements of El Ghazaly *et al* [92], Dunn *et al* [84, 93] and Dance *et al* [83]. Noting that the DI cross sections are an order of magnitude lower than the PP cross sections [91, 94, 95], the TI cross sections $\sigma_{\rm TI} = \sigma_{\rm DE} + \sigma_{\rm DI}$ and PP cross sections can be compared with each other. Firstly comparing the BD and FC vibrationally weighted results, a large difference of approximately 20% is seen in the low-energy region (10–20 eV), which indicates an extremely large dependence on the vibrational state population of the molecule. FC weighting leads to a larger cross section due to their slightly heavier weighting on the highly excited vibrational states. In the low-energy region the present vibrationally weighted PP results have the maximum assigned uncertainty. This is because the uncertainty associated with the extrapolation of fixed-nuclei results to large R directly affects the cross section contribution of the high-lying vibrational levels, which is very sensitive in the low-energy region. In the intermediate-energy region (20–100 eV) the vibrationally weighted results are within 10% of each other and in the high-energy region (above 100 eV) vibrationally weighted results are practically the same. Comparing fixed-nuclei and vibrationally weighted cross sections, the latter are around four times larger in the low-energy region. A significant difference is also seen in the intermediate- and high-energy regions. This again indicates the importance of accounting for the vibrational distribution of H_2^+. Further investigations found that including the complete vibrational

population (even the high-lying vibrational levels) was very important [89].

The measurements of Peart and Dolder [91], El Ghazaly *et al* [92], Dunn *et al* [84, 93] and Dance *et al* [83] have a large variation in the low-energy region. Peart and Dolder [91] have outlined some possible reasons for this large variation, which is likely due to the different vibrational populations of H_2^+ produced in experiment and the sensitivity of the DE cross sections with respect to the initial vibrational state of H_2^+. In the experiment of El Ghazaly *et al* [92] measurements of the vibrational population of H_2^+ indicated that H_2^+ ions were not produced in the $v \geqslant 14$ states, while the experiments of Peart and Dolder [91] and Dunn *et al* [84, 93] were designed to produce H_2^+ ions in a vibrational population given by the FC factors. Comparing the vibrationally weighted PP cross sections with experimental data, BD and FC CCC results are within the experimental error bars of the Dance *et al* [83], Dunn *et al* [84, 93] and Peart and Dolder [91] measurements in the low- and intermediate-energy regions. In the high-energy region, both vibrationally weighted PP cross sections are in good agreement with all experiments and the vibrationally weighted Born cross sections of Peek [85]. The Born results of Peek [85] are approximately 35% larger than the respective CCC results in the low- and intermediate-energy regions. This is the expected low-energy behaviour of cross sections calculated with a first-order method.

DI cross sections are presented in figure 5 for electron scattering from vibrationally excited H_2^+. The FC and BD vibrationally weighted CCC results are compared with the $R_0 = 2.0\ a_0$ results and the measurements of Peart and Dolder [96] and El Ghazaly *et al* [92]. Vibrationally weighted CCC results are approximately 20% larger than the fixed-nuclei results. The difference between these results and the FC and BD weighted CCC results suggests that the DI cross sections are relatively insensitive to the vibrational distribution compared to the PP cross section. Comparing CCC results with experiment, the FC and BD weighted DI results disagree with the measurements of El Ghazaly *et al* [92] in the high-energy region. Noting that the DI cross sections are relatively insensitive to the vibrational distribution, this disagreement is not likely due to the different vibrational populations (assumed here and produced in experiment). The experiment of El Ghazaly *et al* [92] measured the kinetic energy release of H^+ ions after electron-impact dissociation of H_2^+. To differentiate protons resulting from DI or DE, it was assumed that the DI cross sections are not dependent upon R, i.e. $\sigma_{\rm DI}(R)$ is constant. The DI cross section can then be extracted from the tail of the measured kinetic energy release spectrum by extrapolating the tail signal [97]. This procedure was expected to produce inaccurate DI cross sections only near threshold [92], however there is still disagreement with CCC results in the high-energy region. Our calculations indicate that the DI cross section has a linear dependence on R. This dependence on R is not surprising considering that the single-photon ionisation cross sections of H_2^+ have a significant dependence on R [98]. The FC and BD vibrationally weighted

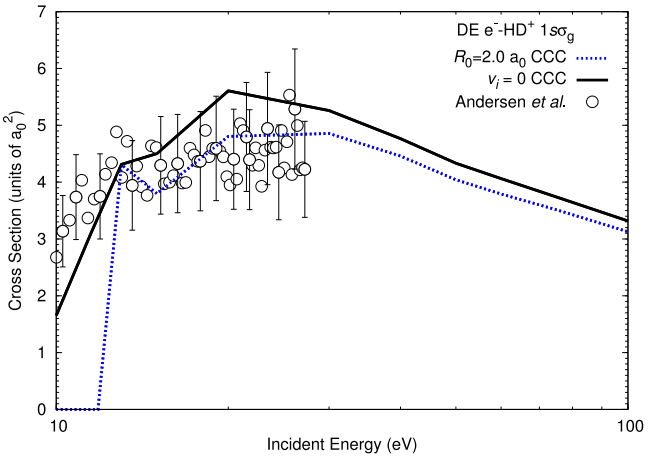

Figure 6. Adiabatic-nuclei CCC calculations of the dissociative excitation (DE) cross section for electron scattering from the ground state of HD^+. Adiabatic-nuclei vibrational ground state results ($v_i = 0$) are compared with the CCC $R_0 = 2.0\ a_0$ results and the measurements of Andersen *et al* [99].

CCC results are in excellent agreement with the measurements of Peart and Dolder [96].

Unlike homonuclear diatomic molecules, the heterogeneous isotopologues all have a permanent electric dipole-moment and internally cool via rotational-vibrational radiative transitions [42]. This allows experiments to prepare the HD^+, HT^+ and DT^+ molecules in the ground vibrational state [99].

Here the vibrationally resolved cross sections are presented for initial vibrational states v_i which have a probability density function that is spanned within the range $1.0 \leqslant R \leqslant 5.5\ \ a_0$. Therefore vibrationally resolved cross sections presented here do not utilise the extrapolation procedure to large R and hence do not have the associated uncertainty. For HD^+ the vibrational state $v = 11$ spans over the range $1.0 \leqslant R \leqslant 5.5\ a_0$.

In figure 6 the HD^+ $v_i = 0$ DE cross section is compared with the experiment of Andersen *et al* [99]. Above 13 eV the adiabatic-nuclei CCC results are in good agreement with experiment, while surprisingly the fixed-nuclei CCC results are in better agreement with experiment than the adiabatic-nuclei CCC results. The poor agreement with experiment below 13 eV comes from the indirect resonant electron attachment processes neglected in the current formalism. For HD^+ in the $v_i = 0$ state the direct DE mechanism (excitation to the $2p\sigma_u$) starts to contribute to the DE cross section at approximately 9 eV, while the indirect mechanism contribution starts to diminish at 9 eV and practically goes to zero at approximately 13 eV [100]. The reasonably good agreement between the adiabatic-nuclei CCC results and experiment indicates the dominance of the direct-scattering process above 10 eV, which is consistent with findings of Duca and Fifirig [100] and Fifirig and Stroe [86].

In figure 7 the HD^+ DE and DI cross sections are presented as a function of the initial vibrational state v_i of the molecule. The DE and DI cross sections of all the isotopologues have a major dependence on v_i in the low- and

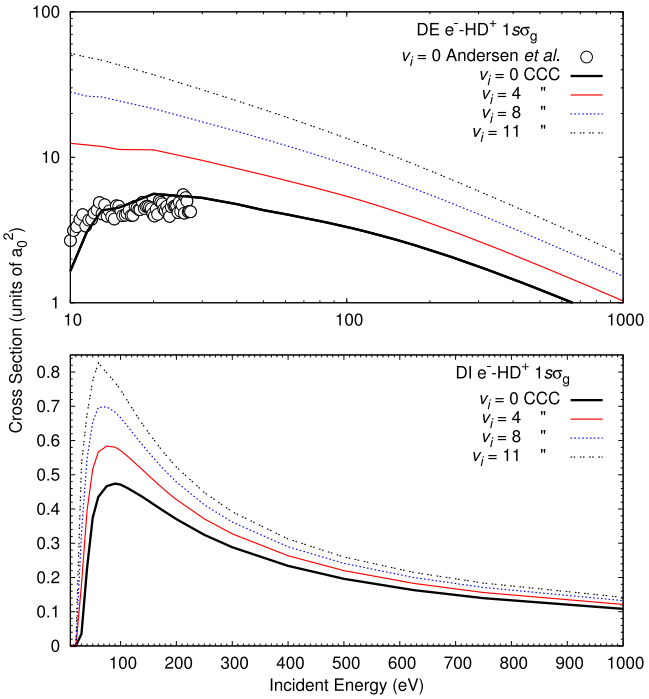

Figure 7. Dissociative excitation (DE) and dissociative ionisation (DI) cross sections for electron scattering from HD^+ in the electronic ground, vibrational state v_i. DE results of HD^+ in the vibrational ground state are compared with the experiment of Andersen *et al* [99].

intermediate-energy regions, as v_i increases the cross sections monotonically increase across the entire energy range. The major difference between the isotopologues vibrationally resolved cross sections is the density and spacing of the vibrational state cross sections, which comes from the number of bound vibrational states in the same range of R [42].

8. Positron scattering from H_2

Adiabatic-nuclei single-centre CCC calculations of positron scattering from the initial $v_i = 0$ and $v_i = 1$ vibrational states of H_2 have been conducted up to 1000 eV and cross sections were calculated with equation (43) [49]. Here we present selected results: the grand total cross section (GTCS), electronic $X^1\Sigma_g^+ \rightarrow B^1\Sigma_u^+$ excitation cross section and total (single-electron) ionisation cross section (TICS), which is the sum of Ps formation (9) and direct ionisation cross sections. In addition we explicitly show that calculations performed with a fixed internuclear distance chosen as the mean internuclear distance of the vibrational ground state ($R_m = 1.448$ a_0) approximates scattering from the vibrational ground state more accurately than the equilibrium distance ($R_0 = 1.4$ a_0) [64]. Preliminary results have been published in [50]. Convergence studies of the present model have been presented in [80], where we estimated the major cross sections to be accurate to within 5% in the fixed-nuclei approximation. For the full details of these calculations and results the reader is referred to [49], which present results for the elastic scattering DCS and the $0 \rightarrow 1$ vibrational excitation cross section. In addition the scattering length, elastic scattering integrated cross section, GTCS and TICS are presented for positron scattering from the $v_i = 0$ and $v_i = 1$ vibrational states. Results will be made available on the LXCat website [90].

8.1. Single- and two-centre close-coupling approaches to positron scattering

For a complete description of positron scattering the two-centre close-coupling method is the most consistent approach to account for Ps formation and the long-range positron–electron correlations. It requires a two centre expansion, where the first expansion is over the target states and the second expansion is over the Ps states. This method, however, is computationally demanding and relatively complicated to implement, and has also been known to suffer from ill conditioning [101, 102]. Pioneering work was conducted by Hewitt *et al* [103, 104], Higgins and Burke [105], Mitroy [106], and Walters *et al* [107], who demonstrated the success of using two-centre expansions for atomic targets. The two-centre approach has also been utilised within the CCC method formalism for positron–atom scattering [101, 102, 108] and recently for positron–H_2 scattering [109]. For a recent review see [110]. To date the only other two-centre coupled-channel positron–molecule (H_2) calculations were conducted by Biswas *et al* [111], which only included the ground states of H_2 and Ps.

In the single-centre approach the total scattering wave function is expanded just over the target states. This close-coupling expansion includes Ps formation implicitly by including configurations that have an electron and positron in the continuum, which corresponds to both the direct ionisation and Ps formation channels. Hence the single-centre expansion includes these channels indirectly and results of the TICS (sum of the direct ionisation and Ps formation cross sections) can be calculated by summing over individual excitation cross sections to positive energy states. This method is significantly simpler to implement than the two-centre approach and is found to be computationally very stable. In the single-centre expansion the strong positron–electron correlations are modelled via a close-coupling expansion that include targets states constructed from a one electron basis that extends to large values of orbital angular momentum. These states orbitals with large values of orbital angular momentum construct the relatively large partial-waves of the positron–electron potential that describe the long-ranged correlations. Convergence can often only be achieved with relatively large close-coupling expansions when compared to the two-centre approach.

However there are a couple of drawbacks of the single-centre approach, the first of which is that the Ps formation and direct ionisation channels are indistinguishable. In addition, incorrect cross sections are calculated in the energy-region (usually referred to as the extended Ore gap) between the Ps formation threshold (6.8 eV below the direct ionisation threshold) and the direct ionisation threshold [112]. This is because an electron can be in the continuum below the direct ionisation threshold via Ps formation, which causes a

mismatch of boundary conditions with the single-centre expansion. Performing single-centre calculations with target state orbitals that have small values of orbital angular momentum, provides an estimate of the cross sections in this energy-region. This is because the Ps formation and breakup processes are effectively taken into account by states that have orbitals with large orbital angular momentum.

8.2. Scattering calculation details

The CCC results have been calculated using a projectile partial-wave expansion with maximum orbital angular momentum $L_{\max} = 8$ and the orientationally averaged ABS method (described in section 5) was used to top-up the partial-wave expansion. The total spin $\mathcal{S} = 1/2$, odd and even parity Π and maximum total orbital angular momentum projection $\mathcal{M}_{\max} = 8$ channels were included in the close-coupling calculations. In this section the dashed–dotted vertical lines at 8.6 and 15.4 eV in the figures respectively indicate the Ps-formation and ionisation thresholds of H_2 in the ground state. Note that with the present $R_m = 1.448\ a_0$ fixed-nuclei structure model, the Ps-formation and ionisation thresholds are at 9.34 and 16.14 eV respectively.

The present H_2 structure model allows for an expansion over the set of antisymmetric two-electron configurations $(nlm, n'l'm')$ (58). One-electron orbitals in the two-electron configurations (58) were constructed from a Laguerre basis that had $l_{\max} = 8$, $N_l = 17 - l$ functions for $l \leqslant 7$ and $N_{l=8} = 10$ with exponential fall-offs $\alpha_l = 1.2$ for $l \leqslant 4$ and $\alpha_l = 1.0$ for $l \geqslant 5$. Here the 'inner' and 'outer' electrons were expanded by all $n, n' \leqslant 3$ one-electron orbitals constructed from short-ranged Laguerre functions with exponential-fall offs of $\alpha_l = 1.9$. In addition, the $1s\sigma_g$ orbital ($n = n' = 1$) was represented by a converged (at an internuclear distance of $R_m = 1.448\ a_0$) molecular-orbital of H_2^+ that was constructed from a Laguerre basis that had $N_l = 60 - l$, $\alpha_l = 1.7$ functions up to $l_{\max} = 8$. The frozen-core model ($1\ s\sigma, n'l'm'$) was utilised for two-electron configurations with $|m_T| \geqslant 2$, where $m_T = m + m'$. For the purpose of scattering calculations this structure model is sufficiently accurate to describe H_2 in the $v_i = 0$ and $v_i = 1$ states, where the $v = 1$ vibrational wave function approximately spans the range $0.8 \leqslant R \leqslant 2.2\ a_0$.

Diagonalising the target Hamiltonian with two-electron configurations built from the above model generated $N = 1013$ target states. At the equilibrium distance of $R_0 = 1.4\ a_0$, the static dipole polarisability of this model is $\alpha_{\parallel} = 6.375\ a_0^3$ and $\alpha_{\perp} = 4.635\ a_0^3$ for the ground state, which compares very well with the accurate calculations of Kolos and Wolniewicz [113] ($\alpha_{\parallel} = 6.380\ a_0^3$ and $\alpha_{\perp} = 4.578\ a_0^3$). The low-lying electronic excited states energies are within 1.5% of the accurate values [69, 114–119] and the dominant oscillator strengths are also well represented in the present model [49].

This 1013-state model is used in the scattering calculations of positron collisions with H_2 in the $v_i = 0$ and $v_i = 1$ vibrational states. Calculations were conducted at eight internuclear distance points within the interval $0.8 \leqslant R \leqslant 2.2\ a_0$. Fixed-nuclei cross sections were found to be smooth as a function of R and were interpolated in this interval of R. Cross sections were calculated within the adiabatic-nuclei approximation (43).

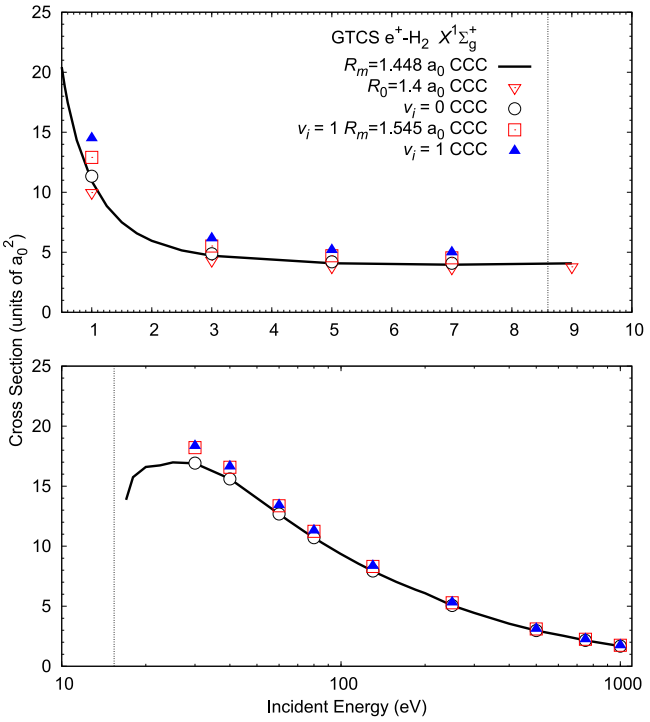

Figure 8. The grand total cross section (GTCS) for positron scattering from the $v_i = 0$ and $v_i = 1$ vibrational states of H_2. Adiabatic-nuclei CCC results are compared with the fixed-nuclei CCC calculations at the mean internuclear distances of the $v_i = 0$ state ($R_m = 1.448\ a_0$), $v_i = 1$ state ($R_m = 1.545\ a_0$) and the equilibrium ($R_0 = 1.4\ a_0$) distance. The dashed–dotted vertical lines at 8.6 and 15.4 eV indicate the positronium-formation and ionisation thresholds of H_2 in the ground state.

8.3. Results

The 1013-state adiabatic-nuclei and fixed-nuclei GTCS are presented in figure 8 for positron scattering from the $v_i = 0$ and $v_i = 1$ states of H_2. In the low-energy region (1–10 eV) the adiabatic-nuclei $v_i = 0$ results are 5%–15% larger than the equilibrium fixed-nuclei $R_0 = 1.4\ a_0$ results, while the mean internuclear distance results of the vibrational ground state $R_m = 1.448\ a_0$, have at most a difference of 3%. This indicates that choosing the mean internuclear distance in a scattering calculation is a better approximation of scattering from the $v_i = 0$ state rather than choosing the commonly used equilibrium internuclear distance. The mean internuclear distance results of the first vibrational state $R_m = 1.545\ a_0$ (taken from the fixed-nuclei cross sections interpolated values) are compared with the $v_i = 1$ adiabatic-nuclei results. At low energies $R_m = 1.545\ a_0$ results are about 10% larger than the $v_i = 1$ adiabatic-nuclei results. Above the ionisation threshold, both mean fixed-nuclei results are a good approximation of the respective adiabatic-nuclei results, where cross sections at high energies have less of a dependence on R than low-energy cross sections.

Comparing the adiabatic-nuclei results in the low-energy region, the $v_i = 1$ results are between 20%–30% larger than the $v_i = 0$ results. Above the ionisation threshold the $v_i = 1$

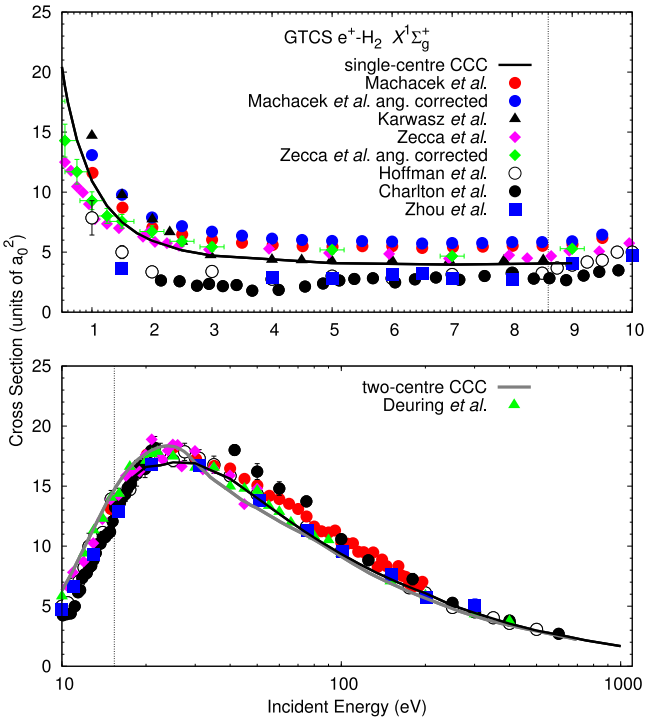

Figure 9. CCC results of the grand total cross section (GTCS) for positron scattering from the ground state of H_2. The mean internuclear distance $R_m = 1.448\ a_0$ fixed-nuclei single-centre CCC results (present) are compared with the $R_0 = 1.4\ a_0$ two-centre CCC calculations [109] and the measurements of Machacek *et al* [120], Karwasz *et al* [121], Zecca *et al* [49, 122], Hoffman *et al* [123], Charlton *et al* [124], Zhou *et al* [125], and Deuring *et al* [126]. The dashed–dotted vertical lines at 8.6 and 15.4 eV indicate the positronium-formation and ionisation thresholds of H_2 in the ground state.

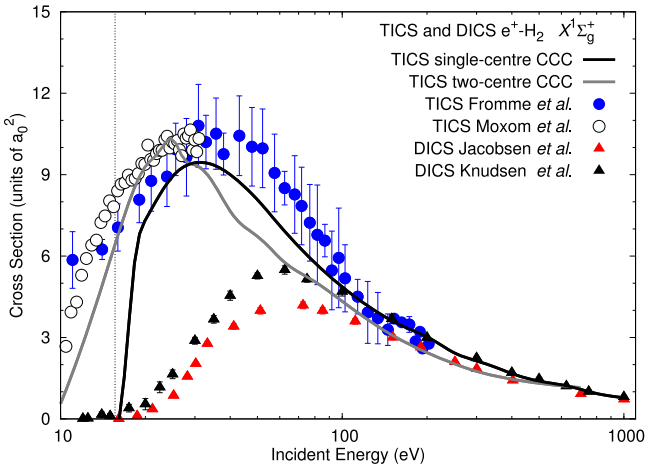

Figure 10. CCC results of the total (single) ionisation cross section (TICS) for positron scattering from the ground state of H_2. The mean internuclear distance $R_m = 1.448\ a_0$ single-centre CCC (present) TICS are compared with the $R_0 = 1.4\ a_0$ two-centre CCC TICS [109], the measurements of Fromme *et al* [128] and Moxom *et al* [129], and the direct ionisation cross section (DICS) measured by Jacobsen *et al* [130] and Knudsen *et al* [131]. The dashed–dotted vertical line at 15.4 eV indicates the ionisation threshold of H_2 in the ground state.

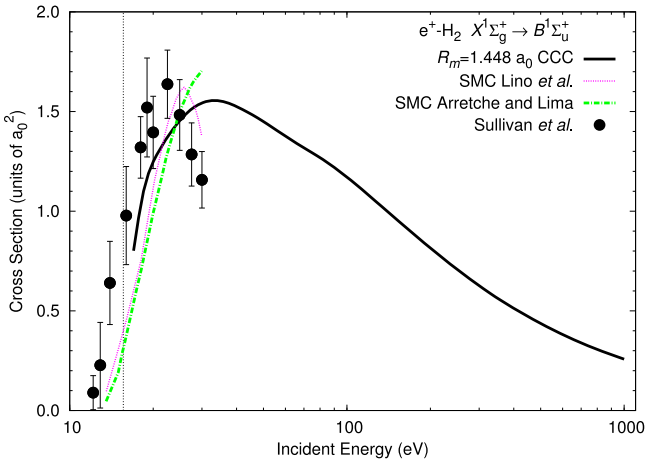

Figure 11. Positron scattering from the ground state of H_2 for the electronic $X^1\Sigma_g^+ \rightarrow B^1\Sigma_u^+$ excitation cross section (summed over all vibrational and rotational excitations). The mean internuclear distance $R_m = 1.448\ a_0$ fixed-nuclei CCC results are compared with the $R_0 = 1.4\ a_0$ fixed-nuclei Schwinger multichannel (SMC) calculations of Lino *et al* [134] and Arretche and Lima [135], and the measurements of Sullivan *et al* [132, 133]. The dashed–dotted vertical line at 15.4 eV indicates the ionisation threshold of H_2 in the ground state.

results are at most 10% larger than the $v_i = 0$ results. At high energies (above 100 eV) the $v_i = 0$ and $v_i = 1$ cross sections converge and by 250 eV the results are practically the same.

In figure 9 the CCC GTCS is compared with experiments for positron scattering from the ground state of H_2. The fixed-nuclei $R_m = 1.448\ a_0$ CCC results are compared with the measurements of Machacek *et al* [120], Karwasz *et al* [121], Zecca *et al* [122], Hoffman *et al* [123], Charlton *et al* [124], Zhou *et al* [125], and Deuring *et al* [126]. Machacek *et al* [120] and Zecca *et al* [49, 122] have also corrected their low-energy measurements to account for scattering to forward angles. It is important to note that the large variation in experimental results at low energies is likely due to different experimental resolution of scattering to forward angles [120, 122], where the resolution of Zecca *et al* [122], Karwasz *et al* [121], and Machacek *et al* [120] experiments are superior [122, 127]. In the low-energy region CCC results are in the best agreement with the measurements of Zecca *et al* [122] and Karwasz *et al* [121]. Below 2 eV the agreement with the measurements of Zecca *et al* [122] improved when the missed scattering to forward angles was accounted for [49].

Above the ionisation threshold (lower panel of figure 9) the single-centre CCC results are in good agreement with all experiments [120, 122–126]. The good agreement with experiment at the cross section maximum (25 eV) suggests that the single-centre CCC calculations are sufficiently large to (indirectly) model Ps-formation. Comparing the single- and two-centre CCC results, above 30 eV the two calculations are within reasonable agreement with each other and converge at higher energies. The two-centre CCC method [109] utilised an approximation in the rearrangement matrix elements, which approximated the positron–nuclei potential (49) as isotropic. This approximation is expected to break down in the low- and intermediate-energy range, hence testing internal consistency between the single- and two-centre CCC

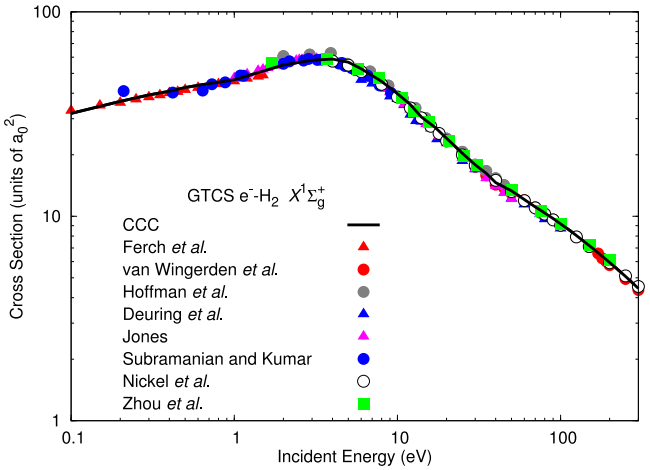

Figure 12. Grand total cross section (GTCS) of electron scattering from H_2. CCC results are compared with the measurements of Ferch *et al* [137], van Wingerden *et al* [138], Hoffman *et al* [123], Deuring *et al* [126], Jones [139], Subramanian and Kumar [140, Nickel *et al* [141], and Zhou *et al* [125].

calculations is not feasible in the low- and intermediate-energy regions.

In figure 10 the $R_m = 1.448\ a_0$ CCC TICS of the H_2 ground state are compared with the measurements of Fromme *et al* [128] and Moxom *et al* [129] and the $R_0 = 1.4\ a_0$ two-centre CCC TICS [109]. Just above the ionisation threshold the single-centre CCC TICS increases rapidly as more positive energy pseudostates become energetically open, which is the expected behaviour of a single-centre method. At the cross section maximum (30 eV), the good agreement between the single-centre CCC TICS and the TICS measurements of Fromme *et al* [128] and Moxom *et al* [129] is encouraging and further indicates that we have (indirectly) modelled Ps-formation accurately. As the projectile energy increases the Ps-formation cross section diminishes and becomes negligible by approximately 130 eV [120]. Above 130 eV the single-centre CCC results can be compared with the direct ionisation cross section (DICS) measurements of Jacobsen *et al* [130] and Knudsen *et al* [131] and are found to be in good agreement with both experiments. Comparing the single- and two-centre CCC results, results vary significantly in the intermediate energy-range (10–100 eV) while at higher energies there is good agreement between the two calculations. This difference is likely due to the two-centre CCC calculations approximating the positron–nuclei potential as isotropic.

For the ground state $X^1\Sigma_g^+ \rightarrow B^1\Sigma_u^+$ electronic excitation cross section of H_2, the fixed-nuclei $R_m = 1.448\ a_0$ CCC results are compared with the measurements of Sullivan *et al* [132, 133] and the fixed-nuclei $R_0 = 1.4\ a_0$ SMC calculations of Lino *et al* [134] and Arretche and Lima [135] in figure 11. The calculations of Lino *et al* [134] used Hartree–Fock target state wave functions, while the scattering calculation was just a two-state approximation. This type of calculation is not expected to yield physically accurate results but was simply used as a first attempt at a multichannel calculation. Arretche and Lima [135] have performed a 5-state SMC calculation, which is expected to be more accurate than the calculations of Lino *et al* [134]. The 1013-state CCC results are in good agreement with experiment below 25 eV, however above 25 eV CCC results do not follow the shape of the experimental measurements or the 2-state SMC results. Experiment shows a cross section peak at approximately 20 eV, while both the CCC and 5-state SMC [135] results show a cross section peak above 20 eV.

Referring to figure 11, CCC results show a cross section peak at approximately 30 eV. Although not shown in [80], the fixed-nuclei CCC results for this cross section have achieved convergence (and will be presented elsewhere). The good agreement with experiment for the GTCS, TICS and elastic cross section (refer [120]) in this energy region suggests that by the unitarity of the formalism CCC results for other processes should be sufficiently accurate, given the accuracy of our target states.

9. Electron scattering from H_2

Recently the CCC method was applied to electron scattering from H_2 within the fixed-nuclei approximation [48, 67]. In [67] the GTCS, TICS, elastic integrated cross section and 17.5 eV elastic and electronic excitation DCS were presented. In [48] we presented integrated and DCSs for excitation to the $b\ ^3\Sigma_u^+$, $a\ ^3\Sigma_g^+$, $c\ ^3\Pi_u$, $B\ ^1\Sigma_u^+$, E, $F\ ^1\Sigma_g^+$, $C\ ^1\Pi_u$, $e\ ^3\Sigma_u^+$, $h\ ^3\Sigma_g^+$, $d\ ^3\Pi_u$, $B'\ ^1\Sigma_u^+$, $D\ ^1\Pi_u$, $B''\ ^1\Sigma_u^+$, $D'\ ^1\Pi_u$ states and provide a detailed discussion of the CCC scattering calculations, results and explicitly demonstrate convergence of the total, ionisation, elastic scattering and electronic excitation integrated and DCSs. Though the scattering calculations demonstrated convergence in the scattering model to better than 5%, we believe that the structure model utilised contributes an additional uncertainty to the cross section of less than 10%. The total uncertainty in the fixed-nuclei elastic scattering integrated cross section, TICS, and GTCS is estimated to be better than 5%, and 11% for the electronic excitation cross sections. A recommended set of CCC data will be made available on the LXCat website [90]. Results presented in [67] have already been made available on the LXCat website [90].

The results presented here are based on the calculations performed in [48, 67]. Here we present selected fixed-nuclei results of electron scattering from the H_2 ground state: the GTCS, TICS, electronic $X^1\Sigma_g^+ \rightarrow B^1\Sigma_u^+$ excitation cross section, and the elastic scattering integrated and DCSs.

9.1. Scattering calculation details

Briefly, the electron–H_2 fixed-nuclei CCC calculations have been conducted from 0.1 to 300 eV, and were performed with a projectile partial-wave expansion up to the orbital angular momentum $L_{\max} = 8$ and the orientationally averaged ABS method was utilised (as described in section 5). All total orbital angular momentum projection $\mathcal{M}$, odd and even parity Π and total spin $\mathcal{S} = 1/2$ channels were included in the close-coupling calculations up to the maximum total orbital angular momentum projection $\mathcal{M}_{\max} = 8$. Calculations were performed within fixed-nuclei approximation at the mean

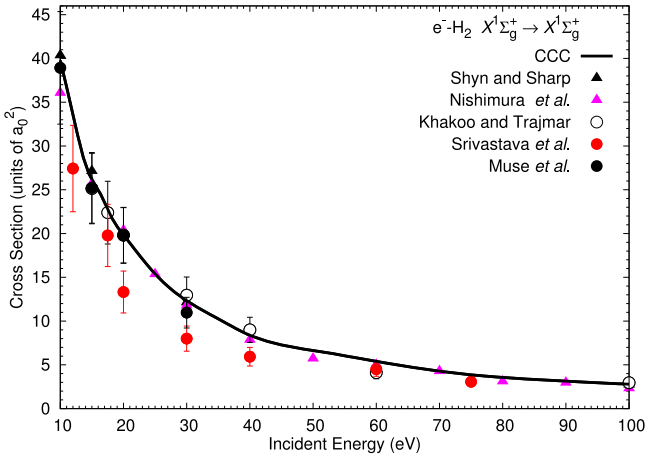

Figure 13. Elastic cross section of electron scattering from H_2. CCC results are compared with the measurements of Shyn and Sharp [142], Nishimura *et al* [143], Khakoo and Trajmar [144], Srivastava *et al* [145], and Muse *et al* [146].

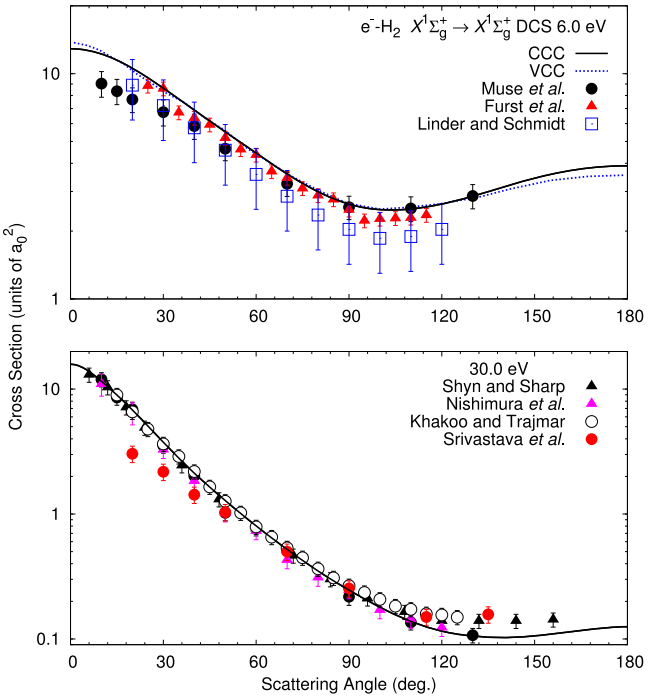

Figure 14. Electron scattering from the ground state of H_2 for the elastic differential cross section (DCS) at 6 and 30 eV. CCC results are compared with the vibrational close-coupling (VCC) calculations of Morrison *et al* [147] (private communication reported in [148]) and the measurements of Muse *et al* [146], Furst *et al* [148], Linder and Schmidt [149], Shyn and Sharp [142], Nishimura *et al* [143], Khakoo and Trajmar [144], and Srivastava *et al* [145].

internuclear distance of the H_2 vibrational ground state $R_m = 1.448\ a_0$.

The H_2 structure model allows for an expansion over the two electrons (nlm, $n'l'm'$). In the present model, one-electron orbitals in the two-electron configurations (58) were constructed from a Laguerre basis that had $N_l = 17 - l$, $l_{\max} = 3$ functions, with exponential fall offs $\alpha_l \approx 0.77$. For this model the 'inner' and 'outer' electrons were expanded by all $n, n' \leqslant 2$ one-electron orbitals that were constructed from short-ranged Laguerre functions with exponential-fall offs of $\alpha_l = 1.85$. The $1s\sigma_g$ orbital ($n = n' = 1$) is represented by a converged (at an internuclear distance of $R_m = 1.448\ a_0$) molecular-orbital of H_2^+ that was constructed from a Laguerre basis that had $N_l = 60 - l$, $\alpha_l = 0.9$ functions up to $l_{\max} = 8$.

Diagonalising the target Hamiltonian with two-electron configurations built from the above model generated $N = 491$ target states, with 91 states in the discrete spectrum. At the equilibrium distance of $R_0 = 1.4\ a_0$, the static dipole polarisability of the ground state is $\alpha_\parallel = 6.427\ a_0^3$ and $\alpha_\perp = 4.637\ a_0^3$, which compares well with the accurate calculations of Kolos and Wolniewicz [113] ($\alpha_\parallel = 6.380\ a_0^3$ and $\alpha_\perp = 4.578\ a_0^3$). At $R_0 = 1.4\ a_0$ the low-lying electronic excited states energies and oscillator strengths are presented in [48], and the $X^1\Sigma_g^+ \rightarrow B^1\Sigma_u^+$ transition length gauge oscillator strength is 0.277, which compares reasonably well with the accurate theoretical value of 0.301 [119, 136].

9.2. Results

We start the presentation of results with the GTCS of the H_2 ground state in figure 12. Fixed-nuclei $R_m = 1.448\ a_0$ CCC results are compared with the measurements of Ferch *et al* [137], van Wingerden *et al* [138], Hoffman *et al* [123], Deuring *et al* [126], Jones [139], Subramanian and Kumar [140], Nickel *et al* [141], and Zhou *et al* [125] from 0.1 to 300 eV. As far as we are aware these are the only *ab initio* calculations of the GTCS across the entire energy range and they are in excellent agreement with all measurements. This excellent agreement with experiment indicates that we have accurately taken into account elastic scattering, excitation and ionisation processes.

In figure 13 we compare the CCC elastic integrated cross section with the measurements of Shyn and Sharp [142], Nishimura *et al* [143], Khakoo and Trajmar [144], Srivastava *et al* [145], and Muse *et al* [146] from 10 to 100 eV. For energies below 10 eV see figure 12. CCC results are found to be in excellent agreement with all measurements except those of Srivastava *et al* [145], which are consistently lower than the CCC results and other measurements. The excellent agreement with experiment for the elastic scattering cross section indicates that we have accurately accounted for the polarisability of the target, where approximately 30% of the ground state polarisability of H_2 comes from the continuum.

Low-energy (6 eV) and intermediate-energy (30 eV) elastic DCS are presented in figure 14. The CCC results are compared with the VCC calculations of Morrison *et al* [147] (private communication reported in [148]) and the measurements of Muse *et al* [146], Furst *et al* [148], Linder and Schmidt [149], Shyn and Sharp [142], Nishimura *et al* [143], Khakoo and Trajmar [144], and Srivastava *et al* [145]. In general the CCC results are in excellent agreement with experiment, where the CCC results are within the uncertainty bars of almost all measurements. However a noticeable difference is seen at the 30 eV backward scattering angles, where our results seem to favour the trend of measurements performed by Muse *et al* [146]. At 6 eV our DCS are in excellent agreement with the VCC

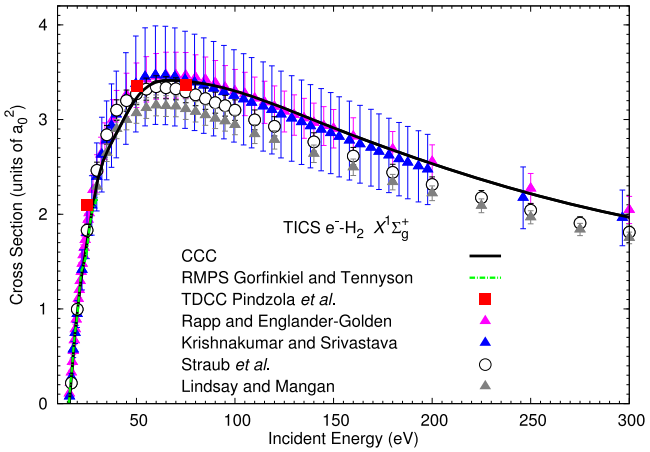

Figure 15. Ionisation cross sections of electron scattering from H_2. The CCC total (single) ionisation cross section (TICS) is compared with the H_2^+ production measurements of Krishnakumar and Srivastava [150] and Straub *et al* [151], the TICS measurements of Lindsay and Mangan [153], and the total (sum of single and double) ionisation cross section measurements of Rapp and Englander-Golden [152]. *R*-matrix with pseudostates (RMPS) [53] results end at 30 eV and are indistinguishable from CCC results. Time-dependent close-coupling (TDCC) [154] results are available only at 25, 50 and 75 eV.

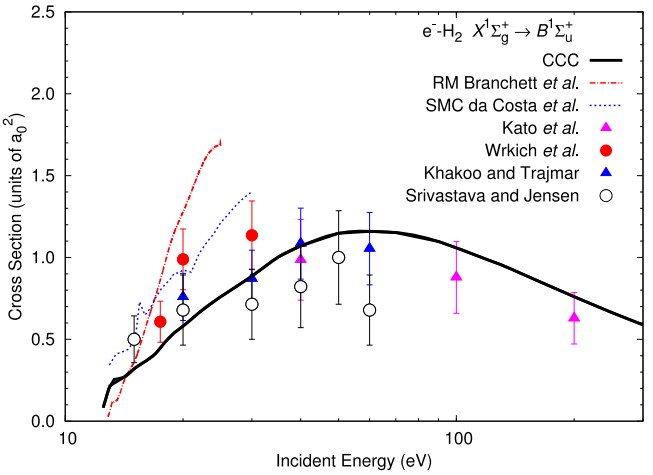

Figure 16. Electron scattering from the ground state of H_2 for the electronic $X^1\Sigma_g^+ \rightarrow B^1\Sigma_u^+$ excitation cross section (summed over all vibrational and rotational excitations). CCC results are compared with the *R*-matrix (RM) calculations of Branchett *et al* [155] and Schwinger multichannel (SMC) of da Costa *et al* [46], and the measurements of Kato *et al* [159], Wrkich *et al* [158], Khakoo and Trajmar [156], and Srivastava and Jensen [157].

calculations of Morrison *et al* [147]. Here the theoretical results are more forward peaked than the measurements of Muse *et al* [146] but seem to agree with the measurements of Furst *et al* [148]. Considering that in the present CCC structure model the electronic ground state has 0.33 eV error in energy (at $R_0 = 1.4$ a_0), this good agreement with experiment for the elastic integrated and DCSs over a broad range of energies indicates that the CCC ground electronic state is sufficiently accurate.

The CCC TICS is presented in figure 15. Firstly, the CCC results are indistinguishable from *ab initio* 41-state RMPS [53] calculations, which are only available from the ionisation threshold to 30 eV. However in the RMPS calculations only the ground and first excited state of H_2 were represented accurately and there was a problem with pseudoresonances. Final RMPS results were taken as an average of several RMPS calculations. The *ab initio* one-electron TDCC method utilised a local-exchange approximation and performed calculations (only available at 25, 50, and 75 eV) with a similar sized partial-wave expansion as the H_2^+ calculations ($L_{\max} = 5$, $\mathcal{M}_{\max} = 2$) [87] together with a polynomial extrapolation technique. Despite these differences (in the methods, the calculation models and approximations used in the TDCC calculations), the CCC results are surprisingly in excellent agreement with both the RMPS and TDCC results.

CCC TICS are also compared with the ionisation measurements of Krishnakumar and Srivastava [150], Straub *et al* [151], Rapp and Englander-Golden [152], and Lindsay and Mangan [153] in figure 15. From ionisation threshold up to the cross section maximum (at approximately 60 eV) CCC results are in excellent agreement all experiments. However at higher energies, CCC results are higher than the measurements of Straub *et al* [151] and Lindsay and Mangan [153], and favour the measurements of Rapp and Englander-Golden [152] and Krishnakumar and Srivastava [150]. The excellent agreement between the CCC results and measurements of the GTCS, elastic scattering cross section and TICS indicates that the electron scattering flux has been correctly distributed to the continuum and discrete spectrum. Hence by noting that the excited target states are accurate and the unitarity of the formalism, the CCC excitations cross sections should be accurate.

The electronic $X^1\Sigma_g^+ \rightarrow B^1\Sigma_u^+$ excitation cross section (summed over all vibrational and rotational excitations) is presented in figure 16. CCC results are compared with the 9-state RM calculations of Branchett *et al* [155] and 9-state SMC calculations of da Costa *et al* [46]. The 9-state *ab initio* RM and SMC results rise sharply from threshold and are in general, much larger than the CCC results. Our investigation [48] identified this difference as a lack of convergence in the RM and SMC calculations with respect to the number target states in the close-coupling calculation. As more states are included in the close-coupling calculations pseudoresonances effectively disappear and the results decrease and converge to the present CCC results [48].

The experiments of Khakoo and Trajmar [156], Srivastava and Jensen [157], Wrkich *et al* [158], and Kato *et al* [159] have measured the $X^1\Sigma_g^+ \rightarrow B^1\Sigma_u^+$ excitation cross section by analysing the energy-loss spectrum of the scattered electrons. Due to the overlapping electronic and vibrational manifolds of H_2 the analysis of the measurements is a difficult procedure that incurs a large uncertainty in the final cross sections (approximately 25%). Comparing CCC results to the measurements, the CCC results are within the error bars of the measurements performed by Kato *et al* [159], Khakoo and Trajmar [156], and the low-energy measurements of Srivastava and Jensen [157]. The measurements of Srivastava and Jensen [157] imply a mostly flat cross section, while the measurements of Wrkich *et al* [158] are too high compared to the CCC results. The high-energy measurements of Kato *et al* [159] derived the total (summed over vibrational and rotational transitions) optical

oscillator strength of this transition (0.241 ± 0.048), which compares well with the $R_m = 1.448\ a_0$ CCC oscillator strength of 0.288 and accurate theory 0.274 [160].

10. Summary and conclusions

10.1. Summary

In this tutorial the molecular CCC method was developed within the adiabatic-nuclei approximation. The CCC method was applied to electron scattering from vibrationally excited H_2^+, electron scattering from the ground state of H_2, and positron scattering from ground $v_i = 0$ and $v_i = 1$ vibrationally excited state of H_2 within the single-centre close-coupling method. Similarly to the atomic implementation of the method, the molecular CCC method has had success in calculating the elastic scattering, electronic excitation, ionisation and total cross sections, where comparison with accurate experiments ranges from good to excellent. The success of the method stems from the use of a near-complete (Laguerre basis) expansion of both the discrete spectrum and continuum of the target, the ability to efficiently couple all reaction channels including ionisation, and to represent the target states sufficiently accurately.

Electron– and positron–molecule scattering calculations demonstrated convergence in the fixed-nuclei close-coupling (target state) and projectile partial-wave expansions. As far as we are aware these are the only electron– and positron–molecule scattering calculations that have rigorously demonstrated convergence over a broad energy range. Hence by noting the accuracy of the target states, the results presented here are expected to be the most accurate in the literature. All of these and future data sets will be made available via the LXCat database [90] and should be useful in astrophysical, plasma, and transport modelling.

Electron scattering from H_2^+ and its isotopologues

Adiabatic-nuclei CCC calculations were performed for electron scattering from vibrationally excited H_2^+ and its isotopologues (D_2^+, T_2^+, HD^+, HT^+ and TD^+). Ionisation and electronic excitation cross sections were calculated from 10 to 1000 eV as a function of the initial vibrational state of the isotopologues. To compare with experiments, CCC vibrationally resolved cross sections were weighted according to the vibrational populations of experiment (FC factors). Adiabatic-nuclei CCC results were found to be in excellent agreement with experiment. The present results have been published in [89, 42], while convergence in the fixed-nuclei calculations was demonstrated here.

Positron scattering from H_2

Adiabatic-nuclei single-centre CCC calculations were performed for positron scattering from the ground and first vibrationally excited state of H_2. Here results were presented from threshold to 1000 eV for the electronic $X^1\Sigma_g^+ \rightarrow B^1\Sigma_u^+$ excitation cross section, GTCS and TICS. In general these results are in good agreement with experiment. Convergence of the present calculations was demonstrated in [80]. In [49] we give details of these calculations, the present results, and in addition present results for the elastic scattering DCS, elastic scattering integrated cross section, the $0 \rightarrow 1$ vibrational excitation cross section and the scattering length, which was found to be in excellent agreement with the accurate calculations of Zhang *et al* [63, 64]. Preliminary CCC results were published as rapid communications in [50]. Detailed manuscripts are currently in preparation on the electronic excitation, vibrational and rotational excitation cross sections.

Electron scattering from H_2

Fixed-nuclei CCC calculations have been performed for electron scattering from the ground state of H_2. Results of the GTCS, TICS, elastic scattering cross section and selected electronic excitation cross sections have been presented here and in [67]. A comprehensive set of convergence studies and recommended results for the GTCS, TICS and electronic excitation integrated and DCSs is given in [48]. In the near future we will investigate the elastic scattering, rotational and vibrational excitation cross sections. The molecular CCC method formulated in a spheroidal coordinate system will be used to perform adiabatic-nuclei calculations, and study scattering from electronic vibrationally excited states and the vibrational excitation cross sections.

10.2. Conclusions

As a first attempt at electron– and positron–molecule CCC calculations, the method has shown great promise. Integrated cross sections for the elastic, electronic excitation and single-ionisation processes are in good agreement with accurate experiment over a broad energy-range. The accurate structure models used in these calculations are calculated from a complete Laguerre basis. Achieving convergent results with respect to the size of the projectile partial-wave and target state (Laguerre basis) expansions indicate that scattering cross sections are accurate. With this solid foundation the CCC method is expected to be successful describing more complicated molecular collision systems.

The adiabatic-nuclei approximation (derived in section 2.2) is the foundation on which techniques are built to describe resonance, dissociative processes, vibrational and rotational excitations in molecules [32, 35, 37, 38]. This approximation as well as various corrections methods [32] (that satisfy the conservation of energy in nuclei excitation processes) will allow us to model such processes and address some long-standing problems, such as the controversy over the vibrational excitation cross sections for molecular hydrogen [161].

10.3. Future research directions

The atomic and molecular CCC methods are fundamentally the same, and are expected to have the same advantages and disadvantages. Future development of the molecular CCC code will be aligned with the interest of the scientific community and successful developments of the atomic CCC method [75–77, 162].

Like the atomic implementation for electron scattering, the molecular CCC formalism will be suited to dealing with molecules where the interaction is dominated by one or two-electron excitations above an inert Hartree–Fock frozen-core [43, 44, 73]. The single-centre expansion approach is particularly suited for modelling targets with a heavy centre, like molecular hydrides [163–165]. Electron scattering from the hydrides HeH^+, LiH^+, LiH and BeH^+ and He_2^+ are particularly important in the modelling of fusion plasmas [166] and hence will be investigated with the CCC method. It is worth noting that hydrides have a strong permanent dipole moment, which in scattering calculations require a large partial-wave expansion to achieve convergence [20]. This can be overcome by utilising the ABS technique described in section 5.

In addition, the molecular CCC method is being formulated in the prolate spheroidal coordinate system to take advantage of the physical configuration of diatomic molecules. Doing so improves the accuracy of the low-lying states and T-matrix elements calculated at intermediate and high R, where the molecule is highly non-spherical. However from our experience spheroidal coordinate calculations are computationally more expensive than the spherical coordinate calculations. This formulation is ideal for the study of diffuse and hot (vibrationally excited) diatomic molecules, which will be particularly useful for plasma modelling [1–4, 166, 167].

Currently the atomic CCC method is being extended to perform single-centre close-coupling calculations of positron scattering from arbitrary atomic targets. Similarly, we expect that by utilising these techniques the molecular CCC method will be able to perform single-centre calculations of positron scattering from arbitrary linear molecules, such as N_2, O_2, CO_2, CO, OH and HCl etc. N_2 and CF_4 (nonlinear) gasses are interesting targets because they are used as energy loss mechanisms to cool down positrons in beam line experiments [168].

A major development of the molecular CCC method worth considering is an an extension of the method to polyatomic hydrides such as H_3^+, CH_4 and H_2O. H_3^+ is one of the most common ions in the Universe and plays a key role in hydrogen plasmas [4, 8]. Electron scattering from this tightly bound two-electron target should be accurately modelled within the single-centre expansion CCC method. Positron scattering from CH_4 and H_2O is synonymous with positron scattering from isoelectronic Ne. Recently single-centre CCC calculations of positron–Ne scattering produced results in good agreement with experiment [169], and hence the same success is expected for these molecular scattering systems.

Acknowledgments

We thank Dr James Colgan for helpful discussions and reviewing this manuscript. This work was supported by the United States Air Force Office of Scientific Research (AOARD), Los Alamos National Laboratory (LANL) and Curtin University. MZ would like to specifically acknowledge LANL's ASC PEM Atomic Physics Project for its support. The LANL is operated by Los Alamos National Security, LLC for the National Nuclear Security Administration of the US Department of Energy under Contract No. DEAC52-06NA25396. Resources were provided by the Pawsey Supercomputing Centre with funding from the Australian Government and the Government of Western Australia.

Appendix A. Orientation averaged DCSs

Here we derive the orientationally averaged DCS and integrated cross section. Starting with the adiabatic-nuclei scattering amplitude (resolved for the transition $iv_iJ_im_{J_i} \rightarrow fv_fJ_fm_{J_f}$) (36) and substituting the rigid rotor rotational wave functions (32), the scattering amplitude has the form

$$F^{\mathcal{S}}_{fv_fJ_fm_{J_f},iv_iJ_im_{J_i}}(\boldsymbol{q}_f^{(\mathrm{lab})},\boldsymbol{q}_i^{(\mathrm{lab})}) = \sum_{\substack{L_f,L_i\\M_f,M_i}} \frac{\hat{L}_i}{\sqrt{4\pi}} \langle \nu_{fv_fJ_f}|A^{\mathcal{S}(\mathrm{b})}_{fL_fM_f,iL_iM_i}|\nu_{iv_iJ_i}\rangle_R \times \langle Y_{J_fm_{J_f}}|\sum_{\kappa} D^{L_f}_{\kappa,M_f} D^{L_i*}_{0,M_i}|Y_{J_im_{J_i}}\rangle_{\hat{\boldsymbol{R}}^{(\mathrm{lab})}} Y_{L_f\kappa}(\hat{\boldsymbol{q}}_f^{(\mathrm{lab})}), \quad (A.1)$$

where $\hat{L} = \sqrt{(2L+1)}$. Substituting the above scattering amplitude (A.1) into the DCS (18), the DCS resolved for the transition $iv_iJ_im_{J_i} \rightarrow fv_fJ_fm_{J_f}$ is

$$\frac{\mathrm{d}\sigma^{\mathcal{S}}_{fv_fJ_fm_{J_f},iv_iJ_im_{J_i}}}{\mathrm{d}\Omega^{(\mathrm{lab})}} = \frac{q_f}{q_i}\frac{1}{4\pi} \sum_{\substack{L_f,L_i\\M_f,M_i}} \sum_{\substack{L_f',L_i'\\M_f',M_i'}} \times \hat{L}_i\hat{L}_i' \langle \nu_{fv_fJ_f}|A^{\mathcal{S}(\mathrm{b})}_{fL_fM_f,iL_iM_i}|\nu_{iv_iJ_i}\rangle_R \times \langle \nu^*_{fv_fJ_f}|A^{\mathcal{S}(\mathrm{b})*}_{fL_f'M_f',iL_i'M_i'}|\nu^*_{iv_iJ_i}\rangle_{R'} \times \sum_{\kappa\kappa'} \langle Y_{J_fm_{J_f}}|D^{L_f}_{\kappa,M_f} D^{L_i*}_{0,M_i}|Y_{J_im_{J_i}}\rangle_{\hat{\boldsymbol{R}}^{(\mathrm{lab})}} \times \langle Y^*_{J_fm_{J_f}}|D^{L_f'*}_{\kappa',M_f'} D^{L_i'}_{0,M_i'}|Y^*_{J_im_{J_i}}\rangle_{\hat{\boldsymbol{R}}'^{(\mathrm{lab})}} Y_{L_f\kappa}(\hat{\boldsymbol{q}}_f^{(\mathrm{lab})}) Y^*_{L_f'\kappa'}(\hat{\boldsymbol{q}}_f^{(\mathrm{lab})}). \quad (A.2)$$

Summing the DCS over all final rotational states with the closure property (D.7) of the rotational wave functions

$$\sum_{J_fm_{J_f}} Y^*_{J_fm_{J_f}}(\hat{\boldsymbol{R}}^{(\mathrm{lab})}) Y_{J_fm_{J_f}}(\hat{\boldsymbol{R}}'^{(\mathrm{lab})}) = \delta(\hat{\boldsymbol{R}}^{(\mathrm{lab})} - \hat{\boldsymbol{R}}'^{(\mathrm{lab})}), \quad (A.3)$$

the DCS resolved for the transition $iv_iJ_im_{J_i} \rightarrow fv_f$ has the form

$$\frac{\mathrm{d}\sigma^{\mathcal{S}}_{fv_f,iv_iJ_im_{J_i}}}{\mathrm{d}\Omega^{(\mathrm{lab})}} = \frac{q_f}{q_i}\frac{1}{4\pi} \sum_{\substack{L_f,L_i\\M_f,M_i}} \sum_{\substack{L_f',L_i'\\M_f',M_i'}} \hat{L}_i\hat{L}_i' \langle \nu_{fv_f}| \times A^{\mathcal{S}(\mathrm{b})}_{fL_fM_f,iL_iM_i}|\nu_{iv_i}\rangle_R \langle \nu^*_{fv_f}|A^{\mathcal{S}(\mathrm{b})*}_{fL_f'M_f',iL_i'M_i'}|\nu^*_{iv_i}\rangle_{R'} \times \sum_{\kappa\kappa'} \left(\int D^{L_f}_{\kappa,M_f}(\hat{\boldsymbol{R}}^{(\mathrm{lab})}) D^{L_i*}_{0,M_i}(\hat{\boldsymbol{R}}^{(\mathrm{lab})}) D^{L_f'*}_{\kappa',M_f'}(\hat{\boldsymbol{R}}^{(\mathrm{lab})}) \times D^{L_i'}_{0,M_i'}(\hat{\boldsymbol{R}}^{(\mathrm{lab})}) |Y_{J_im_{J_i}}(\hat{\boldsymbol{R}}^{(\mathrm{lab})})|^2 \mathrm{d}\Omega_{\hat{\boldsymbol{R}}^{(\mathrm{lab})}} \right) \times Y_{L_f\kappa}(\hat{\boldsymbol{q}}_f^{(\mathrm{lab})}) Y^*_{L_f'\kappa'}(\hat{\boldsymbol{q}}_f^{(\mathrm{lab})}). \quad (A.4)$$

We note that vibrational wave functions $\nu_{nv_nJ_n}(R)$ have a very minor dependence on J and we assume that they are independent

of J and are taken for $J = 0$ here, i.e. ν_{nv_n}. Scattering from the ground state, i.e. $J_i = 0$, the DCS (A.4) becomes

$$\frac{\mathrm{d}\sigma^{\mathcal{S}}_{fv_f,iv_i}}{\mathrm{d}\Omega^{(\mathrm{lab})}} = \frac{q_f}{q_i}\frac{1}{4\pi}\sum_{\substack{L_f,L_i\\M_f,M_i}}\sum_{\substack{L_f',L_i'\\M_f',M_i'}}\hat{L}_i\hat{L}_i'\,\langle\nu_{fv_f}|A^{\mathcal{S}(\mathrm{b})}_{fL_fM_f,iL_iM_i}|\nu_{iv_i}\rangle_R \times \langle\nu^*_{fv_f}|A^{\mathcal{S}(\mathrm{b})*}_{fL_f'M_f',iL_i'M_i'}|\nu^*_{iv_i}\rangle_{R'} \times \sum_{\kappa\kappa'}\left(\frac{1}{4\pi}\int D^{L_f}_{\kappa,M_f}(\hat{\boldsymbol{R}}^{(\mathrm{lab})})D^{L_i*}_{0,M_i}(\hat{\boldsymbol{R}}^{(\mathrm{lab})})D^{L_f'*}_{\kappa',M_f'}(\hat{\boldsymbol{R}}^{(\mathrm{lab})}) \times D^{L_i'}_{0,M_i'}(\hat{\boldsymbol{R}}^{(\mathrm{lab})})\mathrm{d}\Omega_{\hat{\boldsymbol{R}}^{(\mathrm{lab})}}\right)Y_{L_f\kappa}(\hat{\boldsymbol{q}}_f^{(\mathrm{lab})})\,Y^*_{L_f'\kappa'}(\hat{\boldsymbol{q}}_f^{(\mathrm{lab})}). \tag{A.5}$$

This form of the DCS is equivalent to the orientation averaged DCS [47, 60–62] (for diatomic molecules), which is resolved for the transition $iv_i \to fv_f$ and can be expressed as

$$\frac{\mathrm{d}\sigma^{\mathcal{S}}_{fv_f,iv_i}}{\mathrm{d}\Omega^{(\mathrm{lab})}} = \frac{q_f}{q_i}\frac{1}{4\pi}\int_0^{2\pi}\int_0^{\pi}|F^{\mathcal{S}}_{fv_f,iv_i}(\boldsymbol{q}_f^{(\mathrm{lab})},\boldsymbol{q}_i^{(\mathrm{lab})},\hat{\boldsymbol{R}}^{(\mathrm{lab})})|^2 \times \mathrm{d}\phi_{\hat{\boldsymbol{R}}}\sin(\theta_{\hat{\boldsymbol{R}}})\mathrm{d}\theta_{\hat{\boldsymbol{R}}}, \tag{A.6}$$

where $F^{\mathcal{S}}_{fv_f,iv_i}$ is given in equation (37) and again here

$$F^{\mathcal{S}}_{fv_f,iv_i}(\boldsymbol{q}_f^{(\mathrm{lab})},\boldsymbol{q}_i^{(\mathrm{lab})},\hat{\boldsymbol{R}}^{(\mathrm{lab})}) = \sum_{\substack{L_f,L_i\\M_f,M_i}}\frac{\hat{L}_i}{\sqrt{4\pi}}\langle\nu_{fv_f}|A^{\mathcal{S}(\mathrm{b})}_{fL_fM_f,iL_iM_i}|\nu_{iv_i}\rangle_R \times \sum_{\kappa}D^{L_f}_{\kappa,M_f}(\hat{\boldsymbol{R}}^{(\mathrm{lab})})D^{L_i*}_{0,M_i}(\hat{\boldsymbol{R}}^{(\mathrm{lab})})\,Y_{L_f\kappa}(\hat{\boldsymbol{q}}_f^{(\mathrm{lab})}). \tag{A.7}$$

Hence, the orientation averaging procedure is equivalent to scattering from the $J_i = 0$ state of the molecule and summing the adiabatic-nuclei DCS over all final rotational states (within the rigid rotor approximation). Substituting the lab-frame scattering amplitude (A.7) into the DCS (A.6) and noting that the rotation matrices Euler angles are chosen such that $\boldsymbol{\beta} = (\phi_{\hat{\boldsymbol{R}}}, \theta_{\hat{\boldsymbol{R}}}, 0) = \hat{\boldsymbol{R}}^{(\mathrm{lab})}$, the orientation averaged DCS has the form

$$\frac{\mathrm{d}\sigma^{\mathcal{S}}_{fv_f,iv_i}}{\mathrm{d}\Omega^{(\mathrm{lab})}} = \frac{q_f}{q_i}\frac{1}{4\pi}\sum_{\substack{L_f,L_i\\M_f,M_i}}\sum_{\substack{L_f',L_i'\\M_f',M_i'}}\hat{L}_i\hat{L}_i'\,\langle\nu_{fv_f}|A^{\mathcal{S}(\mathrm{b})}_{fL_fM_f,iL_iM_i}|\nu_{iv_i}\rangle_R \times \langle\nu^*_{fv_f}|A^{\mathcal{S}(\mathrm{b})*}_{fL_f'M_f',iL_i'M_i'}|\nu^*_{iv_i}\rangle_{R'} \times \sum_{\kappa\kappa'}\left((4\pi)^{-1}\int_0^{2\pi}\int_0^{\pi}D^{L_f}_{\kappa,M_f}(\phi_{\hat{\boldsymbol{R}}},\theta_{\hat{\boldsymbol{R}}},0)D^{L_i*}_{0,M_i}(\phi_{\hat{\boldsymbol{R}}},\theta_{\hat{\boldsymbol{R}}},0) \times D^{L_f'*}_{\kappa',M_f'}(\phi_{\hat{\boldsymbol{R}}},\theta_{\hat{\boldsymbol{R}}},0) \times D^{L_i'}_{0,M_i'}(\phi_{\hat{\boldsymbol{R}}},\theta_{\hat{\boldsymbol{R}}},0)\mathrm{d}\phi_{\hat{\boldsymbol{R}}}\sin(\theta_{\hat{\boldsymbol{R}}})\mathrm{d}\theta_{\hat{\boldsymbol{R}}}\right)Y_{L_f\kappa}(\hat{\boldsymbol{q}}_f^{(\mathrm{lab})}) \times Y^*_{L_f'\kappa'}(\hat{\boldsymbol{q}}_f^{(\mathrm{lab})}), \tag{A.8}$$

which is the same form as equation (A.5). The symmetry property (D.9) is used to obtain $D^{L_f}_{\kappa,M_f}(\hat{\boldsymbol{R}}) = (-1)^{M_f-\kappa}D^{L_f*}_{-\kappa,-M_f}(\hat{\boldsymbol{R}})$, and the definitions (D.12) and (D.13) reduce the Wigner-D functions such that

$$D^{L_i*}_{0,M_i}(\hat{\boldsymbol{R}})D^{L_i'}_{0,M_i'}(\hat{\boldsymbol{R}}) = (-1)^{M_i'}\sum_j C^{j0}_{L_i0,L_i'0} \times C^{jM_i'-M_i}_{L_i-M_i,L_i'M_i'}D^{j*}_{0,M_i-M_i'}(\hat{\boldsymbol{R}}), \tag{A.9}$$

$$(-1)^{M_f-\kappa}D^{L_f*}_{-\kappa,-M_f}(\hat{\boldsymbol{R}})D^{L_f'*}_{\kappa',M_f'}(\hat{\boldsymbol{R}}) = (-1)^{M_f'-\kappa'} \times \sum_{j'}C^{j'\kappa-\kappa'}_{L_f\kappa,L_f'-\kappa'}C^{j'M_f-M_f'}_{L_fM_f,L_f'-M_f'}D^{j'}_{\kappa-\kappa',M_f-M_f'}(\hat{\boldsymbol{R}}), \tag{A.10}$$

where $C^{lm}_{l_1m_1,l_2m_2}$ denotes Clebsch–Gordan coefficients. Substituting the above into (A.8) and noting the conservation of orbital angular momentum projection ($m_i + M_i = m_f + M_f$ and $m_i + M_i' = m_f + M_f'$) of the diatomic molecule scattering system, which is enforced by the $\delta_{M_i-M_i',M_f-M_f'}$ term below

$$\frac{\mathrm{d}\sigma^{\mathcal{S}}_{fv_f,iv_i}}{\mathrm{d}\Omega^{(\mathrm{lab})}} = \frac{q_f}{q_i}\frac{1}{(4\pi)^2}\sum_{\substack{L_f,L_i\\M_f,M_i}}\sum_{\substack{L_f',L_i'\\M_f',M_i'}}(-1)^{M_i'+M_f'}\hat{L}_i\hat{L}_i' \times \langle\nu_{fv_f}|A^{\mathcal{S}(\mathrm{b})}_{fL_fM_f,iL_iM_i}|\nu_{iv_i}\rangle_R\,\langle\nu^*_{fv_f}|A^{\mathcal{S}(\mathrm{b})*}_{fL_f'M_f',iL_i'M_i'}|\nu^*_{iv_i}\rangle_{R'} \times \sum_{j'\kappa\kappa'}(-1)^{-\kappa'}C^{j0}_{L_i0,L_i'0}C^{jM_i'-M_i}_{L_i-M_i,L_i'M_i'}C^{j'\kappa-\kappa'}_{L_f\kappa,L_f'-\kappa'} \times C^{j'M_f-M_f'}_{L_fM_f,L_f'-M_f'}Y_{L_f\kappa}(\hat{\boldsymbol{q}}_f^{(\mathrm{lab})})Y^*_{L_f'\kappa'}(\hat{\boldsymbol{q}}_f^{(\mathrm{lab})}) \times \left(\delta_{M_i-M_i',M_f-M_f'}\int_0^{\pi}\int_0^{2\pi}D^{j*}_{0,M_i-M_i'}(\phi_{\hat{\boldsymbol{R}}},\theta_{\hat{\boldsymbol{R}}},0) \times D^{j'}_{\kappa-\kappa',M_f-M_f'}(\phi_{\hat{\boldsymbol{R}}},\theta_{\hat{\boldsymbol{R}}},0)\mathrm{d}\phi_{\hat{\boldsymbol{R}}}\sin(\theta_{\hat{\boldsymbol{R}}})\mathrm{d}\theta_{\hat{\boldsymbol{R}}}\right). \tag{A.11}$$

The spherical harmonic is transformed such that $Y^*_{L_f'\kappa'}(\hat{\boldsymbol{q}}_f^{(\mathrm{lab})}) = (-1)^{\kappa'}Y_{L_f'-\kappa'}(\hat{\boldsymbol{q}}_f^{(\mathrm{lab})})$, and definition (D.15) is used to evaluate the integration over $\hat{\boldsymbol{R}}$

$$\frac{\mathrm{d}\sigma^{\mathcal{S}}_{fv_f,iv_i}}{\mathrm{d}\Omega^{(\mathrm{lab})}} = \frac{q_f}{q_i}\frac{1}{(4\pi)^2}\sum_{\substack{L_f,L_i\\M_f,M_i}}\sum_{\substack{L_f',L_i'\\M_f',M_i'}}(-1)^{M_i'+M_f'}\hat{L}_i\hat{L}_i' \times \langle\nu_{fv_f}|A^{\mathcal{S}(\mathrm{b})}_{fL_fM_f,iL_iM_i}|\nu_{iv_i}\rangle_R\,\langle\nu^*_{fv_f}|A^{\mathcal{S}(\mathrm{b})*}_{fL_f'M_f',iL_i'M_i'}|\nu^*_{iv_i}\rangle_{R'} \times \sum_{j'j\kappa\kappa'}C^{j0}_{L_i0,L_i'0}C^{jM_i'-M_i}_{L_i-M_i,L_i'M_i'}C^{j'\kappa-\kappa'}_{L_f\kappa,L_f'-\kappa'}C^{j'M_f-M_f'}_{L_fM_f,L_f'-M_f'} \times \left(\frac{4\pi}{(2j+1)}\delta_{jj'}\delta_{0,\kappa-\kappa'}\delta_{M_i-M_i',M_f-M_f'}\right) \times Y_{L_f\kappa}(\hat{\boldsymbol{q}}_f^{(\mathrm{lab})})Y_{L_f'-\kappa'}(\hat{\boldsymbol{q}}_f^{(\mathrm{lab})}). \tag{A.12}$$

Now $\delta_{0,\kappa-\kappa'}$ implies $\kappa' = \kappa$, and the spherical harmonics are collapsed using (D.5)

$$\frac{\mathrm{d}\sigma^{\mathcal{S}}_{fv_f,iv_i}}{\mathrm{d}\Omega^{(\mathrm{lab})}} = \frac{q_f}{q_i}\frac{1}{4\pi}\sum_{\substack{L_f,L_i\\M_f,M_i}}\sum_{\substack{L_f',L_i'\\M_f',M_i'}}(-1)^{M_i'+M_f'}\hat{L}_i\hat{L}_i'$$
$$\times \langle \nu_{fv_f}|A^{\mathcal{S}(\mathrm{b})}_{fL_fM_f,iL_iM_i}|\nu_{iv_i}\rangle_R \langle \nu^*_{fv_f}|A^{\mathcal{S}(\mathrm{b})*}_{fL_f'M_f',iL_i'M_i'}|\nu^*_{iv_i}\rangle_{R'}$$
$$\times \sum_{j\kappa}(2j+1)^{-1}C^{j0}_{L_i0,L_i'0}C^{jM_i'-M_i}_{L_i-M_i,L_i'M_i'}C^{j0}_{L_f\kappa,L_f'-\kappa}C^{jM_f-M_f'}_{L_fM_f,L_f'-M_f'}$$
$$\times \left(\sum_{j'}\frac{\hat{L}_f\hat{L}_f'}{4\pi}C^{j'0}_{L_f0,L_f'0}C^{j'0}_{L_f\kappa,L_f'-\kappa}P_{j'}(\cos(\theta^{(\mathrm{lab})}))\right)\delta_{M_i-M_i',M_f-M_f'}$$
$$= \frac{q_f}{q_i}\frac{1}{(4\pi)^2}\sum_{\substack{L_f,L_i\\M_f,M_i}}\sum_{\substack{L_f',L_i'\\M_f',M_i'}}(-1)^{M_i'+M_f'}\hat{L}_i\hat{L}_i'\hat{L}_f\hat{L}_f'$$
$$\times \langle \nu_{fv_f}|A^{\mathcal{S}(\mathrm{b})}_{fL_fM_f,iL_iM_i}|\nu_{iv_i}\rangle_R \langle \nu^*_{fv_f}|A^{\mathcal{S}(\mathrm{b})*}_{fL_f'M_f',iL_i'M_i'}|\nu^*_{iv_i}\rangle_{R'}$$
$$\times \sum_{j'j}(2j+1)^{-1}C^{j0}_{L_i0,L_i'0}C^{jM_i'-M_i}_{L_i-M_i,L_i'M_i'}C^{jM_f-M_f'}_{L_fM_f,L_f'-M_f'}$$
$$\times C^{j'0}_{L_f0,L_f'0}P_{j'}(\cos(\theta^{(\mathrm{lab})}))\delta_{M_i-M_i',M_f-M_f'}$$
$$\times \sum_{\kappa}C^{j0}_{L_f\kappa,L_f'-\kappa}C^{j'0}_{L_f\kappa,L_f'-\kappa}. \tag{A.13}$$

Summing over κ with the Clebsch–Gordan orthogonality condition (D.24), the final form of the orientation averaged DCS is

$$\frac{\mathrm{d}\sigma^{\mathcal{S}}_{fv_f,iv_i}}{\mathrm{d}\Omega^{(\mathrm{lab})}} = \frac{q_f}{q_i}\frac{1}{(4\pi)^2}\sum_{\substack{L_f,L_i\\M_f,M_i}}\sum_{\substack{L_f',L_i'\\M_f',M_i'}}(-1)^{M_i'+M_f'}\hat{L}_i\hat{L}_i'\hat{L}_f\hat{L}_f'$$
$$\times \langle \nu_{fv_f}|A^{\mathcal{S}(\mathrm{b})}_{fL_fM_f,iL_iM_i}|\nu_{iv_i}\rangle_R \langle \nu^*_{fv_f}|A^{\mathcal{S}(\mathrm{b})*}_{fL_f'M_f',iL_i'M_i'}|\nu^*_{iv_i}\rangle_{R'}$$
$$\times \sum_{j}(2j+1)^{-1}C^{j0}_{L_i0,L_i'0}C^{jM_i'-M_i}_{L_i-M_i,L_i'M_i'}C^{jM_f-M_f'}_{L_fM_f,L_f'-M_f'}$$
$$\times C^{j0}_{L_f0,L_f'0}P_j(\cos(\theta^{(\mathrm{lab})}))\delta_{M_i-M_i',M_f-M_f'}. \tag{A.14}$$

The integrated cross section is calculated by integrating over all final angles of the scattered particle

$$\sigma^{\mathcal{S}}_{fv_f,iv_i} = \int_0^{2\pi}\mathrm{d}\phi_{q_f}\int_0^{\pi}\sin(\theta_{q_f})\frac{\mathrm{d}\sigma^{\mathcal{S}}_{fv_f,iv_i}}{\mathrm{d}\Omega^{(\mathrm{lab})}}\mathrm{d}\theta_{q_f}. \tag{A.15}$$

Noting that $P_0(x) = 1$, definition (D.6) is utilised to integrate over all final angles

$$\int_0^{2\pi}\mathrm{d}\phi_{q_f}\int_0^{\pi}P_j(\cos(\theta_{q_f}))\sin(\theta_{q_f})\mathrm{d}\theta_{q_f} = 4\pi\delta_{j,0}. \tag{A.16}$$

Utilising (A.16) to integrate over all final angles of the DCS and noting the Clebsch–Gordan coefficient $C^{lm}_{l_1m_1,l_2m_2}$ triangle rule $|m| \leqslant l$, the orientation averaged integrated cross section is calculated

$$\sigma^{\mathcal{S}}_{fv_f,iv_i} = \int \mathrm{d}\Omega_{q_f}\frac{\mathrm{d}\sigma^{\mathcal{S}}_{fv_f,iv_i}}{\mathrm{d}\Omega^{(\mathrm{lab})}}$$
$$= \frac{q_f}{q_i}\frac{1}{4\pi}\sum_{\substack{L_f,L_i\\M_f,M_i}}\sum_{\substack{L_f',L_i'\\M_f',M_i'}}(-1)^{M_i'+M_f'}\hat{L}_i\hat{L}_i'\hat{L}_f\hat{L}_f'$$
$$\times \langle \nu_{fv_f}|A^{\mathcal{S}(\mathrm{b})}_{fL_fM_f,iL_iM_i}|\nu_{iv_i}\rangle_R \langle \nu^*_{fv_f}|A^{\mathcal{S}(\mathrm{b})*}_{fL_f'M_f',iL_i'M_i'}|\nu^*_{iv_i}\rangle_{R'}$$
$$\times C^{00}_{L_i0,L_i'0}C^{00}_{L_i-M_i,L_i'M_i'}C^{00}_{L_fM_f,L_f'-M_f'}C^{00}_{L_f0,L_f'0}\delta_{M_i-M_i',M_f-M_f'}. \tag{A.17}$$

Using definition (D.27) to evaluate the Clebsch–Gordan coefficients

$$\sigma^{\mathcal{S}}_{fv_f,iv_i} = \frac{q_f}{q_i}\frac{1}{4\pi}\sum_{\substack{L_f,L_i\\M_f,M_i}}\sum_{\substack{L_f',L_i'\\M_f',M_i'}}(-1)^{M_i'+M_f'}\hat{L}_i\hat{L}_i'\hat{L}_f\hat{L}_f'$$
$$\times \langle \nu_{fv_f}|A^{\mathcal{S}(\mathrm{b})}_{fL_fM_f,iL_iM_i}|\nu_{iv_i}\rangle_R \langle \nu^*_{fv_f}|A^{\mathcal{S}(\mathrm{b})*}_{fL_f'M_f',iL_i'M_i'}|\nu^*_{iv_i}\rangle_{R'}$$
$$\times \left(\frac{(-1)^{L_i}}{\hat{L}_i}\delta_{L_i,L_i'}\right)\left(\frac{(-1)^{L_i+M_i}}{\hat{L}_i}\delta_{L_i,L_i'}\delta_{M_i',M_i}\right)$$
$$\times \left(\frac{(-1)^{L_f-M_f}}{\hat{L}_f}\delta_{L_f,L_f'}\delta_{-M_f',-M_f}\right)$$
$$\times \left(\frac{(-1)^{L_f}}{\hat{L}_f}\delta_{L_f,L_f'}\right)\delta_{M_i-M_i',M_f-M_f'}. \tag{A.18}$$

The final form of the integrated cross section is

$$\sigma^{\mathcal{S}}_{fv_f,iv_i} = \frac{q_f}{q_i}\frac{1}{4\pi}\sum_{\substack{L_f,L_i\\M_f,M_i}}|\langle \nu_{fv_f}|A^{\mathcal{S}(\mathrm{b})}_{fL_fM_f,iL_iM_i}|\nu_{iv_i}\rangle_R|^2. \tag{A.19}$$

Analytic Born cross section

Following from section 5.1, the analytic Born body-frame scattering amplitude for the transition $iv_i \to fv_f$ is given in equation (106). The analytic Born lab-frame scattering amplitude (112) is given as

$$F^{(\mathrm{AB})}_{fv_f,iv_i}(\Omega^{(\mathrm{lab})}, \hat{\boldsymbol{R}}^{(\mathrm{lab})})$$
$$= \sum_{\lambda\mu}\langle \nu_{fv_f}|A^{(\mathrm{AB})}_{\substack{f,i\\\lambda\mu}}(Q^{(\mathrm{b})})|\nu_{iv_i}\rangle_R \sum_{\rho}D^{\lambda*}_{\rho,\mu}(\hat{\boldsymbol{R}}^{(\mathrm{lab})})Y^*_{\lambda\rho}(\hat{\boldsymbol{Q}}^{(\mathrm{lab})}), \tag{A.20}$$

where the momentum transfer is $\boldsymbol{Q} = \boldsymbol{q}_i - \boldsymbol{q}_f$ and $A^{(\mathrm{AB})}_{\substack{f,i\\\lambda\mu}}(Q^{(\mathrm{b})})$ is defined by equation (108). Substituting $F^{(\mathrm{AB})}_{fv_f,iv_i}(\Omega^{(\mathrm{lab})}, \hat{\boldsymbol{R}}^{(\mathrm{lab})})$ into the orientation averaged DCS equation (A.6), the analytic Born DCS is

$$\frac{\mathrm{d}\sigma^{(\mathrm{AB})}_{fv_f,iv_i}}{\mathrm{d}\Omega^{(\mathrm{lab})}} = \frac{q_f}{q_i}\frac{1}{4\pi}\sum_{\lambda\mu}\sum_{\lambda'\mu'}\langle \nu_{fv_f}|A^{(\mathrm{AB})}_{\substack{f,i\\\lambda\mu}}(Q^{(\mathrm{b})})|\nu_{iv_i}\rangle_R$$
$$\times \langle \nu^*_{fv_f}|A^{(\mathrm{AB})*}_{\substack{f,i\\\lambda'\mu'}}(Q^{(\mathrm{b})})|\nu^*_{iv_i}\rangle_{R'}\delta_{\mu,\mu'}$$
$$\times \sum_{\rho\rho'}\left(\int_0^{\pi}\int_0^{2\pi}D^{\lambda*}_{\rho,\mu}(\phi_{\hat{\boldsymbol{R}}}, \theta_{\hat{\boldsymbol{R}}}, 0)D^{\lambda'}_{\rho',\mu'}(\phi_{\hat{\boldsymbol{R}}}, \theta_{\hat{\boldsymbol{R}}}, 0)\mathrm{d}\phi_{\hat{\boldsymbol{R}}}\right.$$
$$\left.\times \sin(\theta_{\hat{\boldsymbol{R}}})\mathrm{d}\theta_{\hat{\boldsymbol{R}}}\right)Y^*_{\lambda\rho}(\hat{\boldsymbol{Q}}^{(\mathrm{lab})})Y_{\lambda'\rho'}(\hat{\boldsymbol{Q}}^{(\mathrm{lab})}), \tag{A.21}$$

where the $\delta_{\mu,\mu'}$ term comes from the analytic Born matrix elements having $\mu = \mu' = m_f - m_i$ as discussed at the end of section 5. Utilising definition (D.15) to evaluate the

integration over $\hat{\boldsymbol{R}}$

$$\begin{aligned}\frac{\mathrm{d}\sigma^{(\mathrm{AB})}_{f_f,i_i}}{\mathrm{d}\Omega^{(\mathrm{lab})}} &= \frac{q_f}{q_i}\frac{1}{4\pi}\sum_{\lambda\mu}\sum_{\lambda'\mu'}\langle\nu_{f_f}|A^{(\mathrm{AB})}_{\substack{f,i\\ \lambda\mu}}(Q^{(\mathrm{b})})|\nu_{i_i}\rangle_R \\ &\times \langle\nu^*_{f_f}|A^{(\mathrm{AB})*}_{\substack{f,i\\ \lambda'\mu'}}(Q^{(\mathrm{b})})|\nu^*_{i_i}\rangle_{R'} \\ &\times \sum_{\rho\rho'}\left(\frac{4\pi}{(2\lambda+1)}\delta_{\lambda,\lambda'}\delta_{\rho,\rho'}\delta_{\mu,\mu'}\right) \\ &\times Y^*_{\lambda\rho}(\hat{\boldsymbol{Q}}^{(\mathrm{lab})})Y_{\lambda'\rho'}(\hat{\boldsymbol{Q}}^{(\mathrm{lab})}) \\ &= \frac{q_f}{q_i}\sum_{\lambda\mu}\frac{1}{(2\lambda+1)}|\langle\nu_{f_f}|A^{(\mathrm{AB})}_{\substack{f,i\\ \lambda\mu}}(Q^{(\mathrm{b})})|\nu_{i_i}\rangle_R|^2 \\ &\times \sum_{\rho}Y^*_{\lambda\rho}(\hat{\boldsymbol{Q}}^{(\mathrm{lab})})Y_{\lambda\rho}(\hat{\boldsymbol{Q}}^{(\mathrm{lab})}). \end{aligned} \tag{A.22}$$

Summing the spherical harmonics over ρ with definition (D.3), the final form of the analytic Born DCS is

$$\begin{aligned}\frac{\mathrm{d}\sigma^{(\mathrm{AB})}_{f_f,i_i}}{\mathrm{d}\Omega^{(\mathrm{lab})}} &= \frac{q_f}{q_i}\sum_{\lambda\mu}\frac{1}{(2\lambda+1)}|\langle\nu_{f_f}|A^{(\mathrm{AB})}_{\substack{f,i\\ \lambda\mu}}(Q^{(\mathrm{b})})|\nu_{i_i}\rangle_R|^2 \\ &\times\left(\frac{(2\lambda+1)}{4\pi}\right) \\ &= \frac{q_f}{q_i}\frac{1}{4\pi}\sum_{\lambda\mu}|\langle\nu_{f_f}|A^{(\mathrm{AB})}_{\substack{f,i\\ \lambda\mu}}(Q^{(\mathrm{b})})|\nu_{i_i}\rangle_R|^2. \end{aligned} \tag{A.23}$$

Appendix B. Laguerre basis functions analytic properties and target state matrix elements

Here we list some of the analytic properties of Laguerre basis functions of order $2l+1$ (55) and evaluate the one-electron (or positron) matrix elements. Laguerre functions of order $2l+1$ satisfy the following differential equation

$$\left(-\frac{1}{2}\frac{\mathrm{d}^2}{\mathrm{d}r^2}+\frac{l(l+1)}{2r^2}\right)\varphi_{kl}(r)=\left(\frac{\alpha_l(k+l)}{r}-\frac{\alpha_l^2}{2}\right)\varphi_{kl}(r), \tag{B.1}$$

where the first two terms on the left hand side have the same form as the kinetic energy operator $K(\boldsymbol{r})$ (48). Laguerre functions with the same exponential fall-offs α_l have the following properties

$$\int_0^\infty \mathrm{d}r\varphi_{kl}(r)\varphi_{kl}(r)=1, \tag{B.2}$$

$$\int_0^\infty \mathrm{d}r\varphi_{k'l}(r)\varphi_{kl}(r) = \begin{cases}0, & k>k'+1\\ -\frac{1}{2}\sqrt{1-\frac{l(l+1)}{(k'+l)(k'+l+1)}}, & k=k'+1\end{cases}, \tag{B.3}$$

$$\int_0^\infty \mathrm{d}r\varphi_{k'l}(r)\frac{1}{r}\varphi_{kl}(r)=\frac{\alpha_l}{(k+l)}\delta_{k',k}. \tag{B.4}$$

Utilising the above properties, the kinetic energy and Coulomb repulsion term matrix elements can be evaluated analytically, such that

$$\begin{aligned}\langle\phi_i|K|\phi_j\rangle &= \delta_{l_i,l_j}\delta_{m_i,m_j} \\ &\times\left(\alpha_{l_j}^2\delta_{k_i,k_j}-\frac{\alpha_{l_j}^2}{2}\int_0^\infty \mathrm{d}r\varphi_{k_il_i}(r)\varphi_{k_jl_j}(r)\right),\end{aligned} \tag{B.5}$$

$$\langle\phi_i|1/R|\phi_j\rangle = \delta_{l_i,l_j}\delta_{m_i,m_j}\frac{1}{R}\int_0^\infty \mathrm{d}r\varphi_{k_il_i}(r)\varphi_{k_jl_j}(r), \tag{B.6}$$

where $\phi(\mathbf{x})$ are the one-electron orbitals (54) and we have dropped the overlap of the spin eigenfunctions from here onwards for convenience.

The angular term in the electron–nuclei (or positron–nuclei) potential V (50) matrix element is evaluated analytically with equation (D.8). The electron–nuclei (or positron–nuclei) matrix element is then given by

$$\begin{aligned}\langle\phi_i|V|\phi_j\rangle &= 2zZ\delta_{m_i,m_j}\sum_{\lambda=0,2,4,..}^{\infty}(-1)^\lambda C^{l_j0}_{l_i0,\lambda0}C^{l_im_i}_{l_jm_j,\lambda0} \\ &\times\int_0^\infty \mathrm{d}r\varphi_{k_il_i}(r)v_\lambda(r,R/2)\varphi_{k_jl_j}(r),\end{aligned} \tag{B.7}$$

where $v_\lambda(r_i,r_j)$ is defined in equation (51).

The overlap of the one-electron orbitals

$$\langle\phi_\alpha|\phi_\gamma\rangle = \delta_{l_\alpha,l_\gamma}\delta_{m_\alpha,m_\gamma}\int_0^\infty \mathrm{d}r\varphi_{k_\alpha l_\alpha}(r)\varphi_{k_\gamma l_\gamma}(r), \tag{B.8}$$

is conveniently evaluated with the Laguerre basis properties (B.2) and (B.3). Integrations that are not evaluated analytically (i.e. (B.7), (C.5), (C.7), (C.9), (C.10) and (C.15)) are calculated numerically with Simpson's rule.

Appendix C. *V*-matrix elements

Here we give explicit forms of the V-matrix elements $V^{\mathcal{M}\Pi\mathcal{S}}_{fL_fM_f,iL_iM_i}(k_f,k_i)$, which are represented in equation (86). For electron scattering the V-matrix interaction terms are a sum of the direct V_U^D and exchange interaction V_U^{Exch} terms, where

$$V_U^{\mathrm{D}} = V_0+\sum_{j=1}^{N_e}V_{0j}-\frac{z_0Z_{\mathrm{Ion}}}{r_0}-U_0, \tag{C.1}$$

$$V^{\mathrm{Exch}} = (E-H)\sum_{j=1}^{N_e}P_{0j}. \tag{C.2}$$

Noting that the exchange-interaction is only present in electron scattering. For single-centre positron scattering the V-matrix interaction term is given by the direct interaction term (C.1).

All angular integrations are carried out analytically using equation (D.8). For convenience we have neglected the overlaps of the spin functions in the following matrix elements.

Electron scattering from H_2^+

The electron–H_2^+ V-matrix elements are given by

$$V^{\mathcal{M}\Pi\mathcal{S}}_{n'L'M',nLM}(k',k') = \langle k'L'M'(\boldsymbol{r}_0),n'm'\pi'(\boldsymbol{r}_1):\mathcal{M}'\Pi'\mathcal{S}'|V_U^D+V^{\mathrm{Exch}}|kLM(\boldsymbol{r}_0),nm\pi(\boldsymbol{r}_1):\mathcal{M}\Pi\mathcal{S}\rangle, \tag{C.3}$$

where $|kLM\rangle$ is from the projectile wave function (84) such that

$$|\boldsymbol{k}^{(\pm)}\rangle = \frac{1}{k}\sum_{L,M}^{\infty} i^L \mathrm{e}^{\pm \mathrm{i}(\sigma_L+\delta_L)}|kLM\rangle\, Y^*_{LM}(\hat{\boldsymbol{k}})$$

$$|kLM\rangle = \sqrt{\frac{2}{\pi}}\frac{1}{r}u_L(r;\, k;\, Z_{\mathrm{Ion}})\, Y_{LM}(\hat{\boldsymbol{r}}), \tag{C.4}$$

and for notational purposes the target states of H_2^+ $|nm\pi\rangle$ are represented by the form of equation (53). The direct part of the V-matrix element is given by

$$\begin{aligned}
&\langle k'L'M'(\boldsymbol{r}_0),\, n'm'\pi'(\boldsymbol{r}_1) : \mathcal{M}'\Pi'\mathcal{S}'|V_U^D|kLM(\boldsymbol{r}_0),\, nm\pi(\boldsymbol{r}_1) : \mathcal{M}\Pi\mathcal{S}\rangle \\
&= \frac{2}{\pi}\delta_{\mathcal{M}',\mathcal{M}}\delta_{\Pi',\Pi}\delta_{\mathcal{S}',\mathcal{S}}\sum_{\alpha\gamma}C_\alpha^{(n')}C_\gamma^{(n)}\sum_{\lambda\mu}(-1)^{\lambda+\mu}C^{L0}_{L'0,\lambda0}C^{L'M'}_{LM,\lambda-\mu} \\
&\times\Bigg[\delta_{\mu,0}\langle\phi_\alpha|\phi_\gamma\rangle\int_0^\infty \mathrm{d}r_0 u_{L'}(r_0;\, k';\, Z_{\mathrm{Ion}})\Bigg[z_0(1+(-1)^\lambda)v_\lambda(r_0,\, R/2) - \delta_{\lambda,0}\left(U(r_0)+\frac{z_0 Z_{\mathrm{Ion}}}{r_0}\right)\Bigg]u_L(r_0;\, k;\, Z_{\mathrm{Ion}}) \\
&- z_0(-1)^\lambda C^{l_\gamma 0}_{l_\alpha 0,\lambda 0}C^{l_\alpha m_\alpha}_{l_\gamma m_\gamma,\lambda\mu}\int \mathrm{d}r_0\mathrm{d}r_1 u_{L'}(r_0;\, k';\, Z_{\mathrm{Ion}})\varphi_\alpha(r_1)v_\lambda(r_0,\, r_1)u_L(r_0;\, k;\, Z_{\mathrm{Ion}})\varphi_\gamma(r_1)\Bigg],
\end{aligned} \tag{C.5}$$

where the overlap of the one-electron orbitals $\langle\phi_\alpha|\phi_\gamma\rangle$ is given in equation (B.8). For electron scattering from H_2^+ the exchange potential (C.2) can have the form

$$\begin{aligned}
V^{\mathrm{Exch}} = &-(-1)^{\mathcal{S}}[E(1-\theta) - (H_0 + H_{\mathrm{T}} + V_{01})]P_{\boldsymbol{r}_0\boldsymbol{r}_1} \\
&- E\theta I_0^N,
\end{aligned} \tag{C.6}$$

where we have included the non-uniqueness matrix elements that enforce the antisymmetrisation property of $\psi_i^{\mathcal{S}N(+)}(\boldsymbol{r}_0,\, \boldsymbol{r}_1;\, R)$ (76), and I_0^N is given in equation (75). The above exchange term can be split into one-electron terms and the electron–electron term. Firstly evaluating the exchange electron–electron term

$$\begin{aligned}
&\langle k'L'M'(\boldsymbol{r}_0),\, n'm'\pi'(\boldsymbol{r}_1) : \mathcal{M}'\Pi'\mathcal{S}'|(-1)^{\mathcal{S}}V_{01}P_{\boldsymbol{r}_0\boldsymbol{r}_1}|\, kLM(\boldsymbol{r}_0),\, nm\pi(\boldsymbol{r}_1) : \mathcal{M}\Pi\mathcal{S}\rangle \\
&= \frac{2}{\pi}(-1)^{\mathcal{S}}\delta_{\mathcal{M}',\mathcal{M}}\delta_{\Pi',\Pi}\delta_{\mathcal{S}',\mathcal{S}}\sum_{\alpha\gamma}C_\alpha^{(n')}C_\gamma^{(n)}\sum_{\lambda\mu}(-1)^\mu C^{l_\gamma 0}_{L'0,\lambda0}C^{L'M'}_{l_\gamma m_\gamma,\lambda-\mu}C^{L0}_{l_\alpha 0,\lambda0}C^{l_\alpha m_\alpha}_{LM,\lambda\mu} \\
&\times\int \mathrm{d}r_0\mathrm{d}r_1 u_{L'}(r_0;\, k';\, Z_{\mathrm{Ion}})\varphi_\alpha(r_1)v_\lambda(r_0,\, r_1)\, u_L(r_1;\, k;\, Z_{\mathrm{Ion}})\varphi_\gamma(r_0).
\end{aligned} \tag{C.7}$$

The one-electron terms are given by

$$\begin{aligned}
&\langle k'L'M'(\boldsymbol{r}_0),\, n'm'\pi'(\boldsymbol{r}_1) : \mathcal{M}'\Pi'\mathcal{S}'|(-E\theta I_0^N - (-1)^{\mathcal{S}}\,[E(1-\theta) - (H_0+H_T)]P_{\boldsymbol{r}_0\boldsymbol{r}_1})|\, kLM(\boldsymbol{r}_0),\, nm\pi(\boldsymbol{r}_1) : \mathcal{M}\Pi\mathcal{S}\rangle \\
&= -(-1)^{\mathcal{S}}\delta_{\mathcal{M}',\mathcal{M}}\delta_{\Pi',\Pi}\delta_{\mathcal{S}',\mathcal{S}}[\langle k'L'M'|nm\pi\rangle\langle n'm'\pi'|kLM\rangle(E(1-\theta) - \varepsilon_{k'} - \varepsilon_k - 1/R) \\
&- \langle k'L'M'|V_0 + Z_{\mathrm{Ion}}/r_0 - U_0|nm\pi\rangle - \langle n'm'\pi'|V_1 + Z_{\mathrm{Ion}}/r_1 - U_1|kLM\rangle] \\
&- \delta_{n',n}\delta_{\mathcal{M}',\mathcal{M}}\delta_{\Pi',\Pi}\delta_{\mathcal{S}',\mathcal{S}}E\theta\,\langle k'L'M'|I_0^N|kLM\rangle,
\end{aligned} \tag{C.8}$$

where the one-electron matrix elements for H_0 and H_1 are evaluated by rearranging equation (67) such that $K|kLM\rangle = (\varepsilon_k - U + Z_{\mathrm{Ion}}/r)|kLM\rangle$. The one-electron matrix elements are evaluated by

$$\begin{aligned}
\langle k'L'M'|nm\pi\rangle = &\sqrt{\frac{2}{\pi}}\sum_\gamma C_\gamma^{(n)}\delta_{L',l_\gamma}\delta_{M',m_\gamma} \\
&\times\int_0^\infty \mathrm{d}r u_{L'}(r;\, k';\, Z_{\mathrm{Ion}})\varphi_\gamma(r),
\end{aligned} \tag{C.9}$$

$$\begin{aligned}
&\langle k'L'M'|V + Z_{\mathrm{Ion}}/r - U|nm\pi\rangle \\
&= \sqrt{\frac{2}{\pi}}\sum_\gamma C_\gamma^{(n)}\sum_{\lambda=0,2,4,..}(-1)^\lambda C^{l_\gamma 0}_{L'0,\lambda0}C^{L'M'}_{l_\gamma m_\gamma,\lambda0} \\
&\times\int_0^\infty \mathrm{d}r u_{L'}(r;\, k';\, Z_{\mathrm{Ion}})[-2v_\lambda(r,\, R/2) \\
&+ \delta_{\lambda,0}\left(\frac{Z_{\mathrm{Ion}}}{r} - U(r)\right)\Bigg]\varphi_\gamma(r).
\end{aligned} \tag{C.10}$$

The V-matrix element $V^{\mathcal{M}\Pi\mathcal{S}}_{fL_fM_f,iL_iM_i}(k_f,\, k_i)$ in (86) is the sum of (C.5), (C.7) and (C.8).

Electron scattering from H_2

Applying the CCC method to electron or positron scattering from H_2, the the V-matrix elements $V^{\mathcal{M}\Pi\mathcal{S}}_{fL_fM_f,iL_iM_i}(k_f, k_i)$ in the corresponding equations in section 4 are calculated with the direct part of the interaction potential

$$V_U^D = V_0 + 2V_{01} - U_0. \tag{C.11}$$

and in the case of electron scattering, the exchange part of the interaction potential is

$$V^{\text{Exch}} = 2(E(1 - \theta\Delta) - H)P_{01} - 2E\theta I_0^N \Delta, \tag{C.12}$$

where

$$H = H_0^{\text{Elec}} + H_1^{\text{Elec}} + H_2^{\text{Elec}} + V_{12} + 1/R + V_{01} + V_{02}, \tag{C.13}$$

Δ is a logical operator that is defined below, the projection operator

$$I_0^N = \sum_{n=1}^{N} |\phi_n\rangle\langle\phi_n|, \tag{C.14}$$

and N is the total number of one-electron orbitals in the basis. Note in the case of electron scattering, the one-electron orbitals in the target states and projection operator are made orthogonal via the Gram–Schmidt process.

The direct part of the V-matrix elements are relatively straightforward and are given by

$$\begin{aligned}
&\langle k'L'M'(\boldsymbol{r}_0),\, n'm'\pi's'(\boldsymbol{r}_1,\boldsymbol{r}_2):\, \mathcal{M}'\Pi'\mathcal{S}'|V_U^D|\, kLM(\boldsymbol{r}_0),\, nm\pi s(\boldsymbol{r}_1,\boldsymbol{r}_2):\, \mathcal{M}\Pi\mathcal{S}\rangle \\
&= \frac{2}{\pi}\delta_{\mathcal{M}',\mathcal{M}}\delta_{\Pi',\Pi}\delta_{\mathcal{S}',\mathcal{S}}\delta_{s',s}\sum_{\alpha\beta\gamma\delta} C^{(n')}_{\alpha,\beta}C^{(n)}_{\gamma,\delta}\langle\phi_\beta|\phi_\delta\rangle\sum_{\lambda\mu}(-1)^{\lambda+\mu}C^{L0}_{L'0,\lambda0}C^{L'M'}_{LM,\lambda-\mu} \\
&\quad\times\Bigg[\delta_{\mu,0}\langle\phi_\alpha|\phi_\gamma\rangle\int_0^\infty \mathrm{d}r_0 u_{L'}(r_0;\,k')[z_0(1+(-1)^\lambda)v_\lambda(r_0,\,R/2) - \delta_{\lambda,0}U(r_0)]u_L(r_0;\,k) \\
&\quad - 2z_0(-1)^\lambda C^{l_\gamma 0}_{l_\alpha 0,\lambda 0}C^{l_\alpha m_\alpha}_{l_\gamma m_\gamma,\lambda\mu}\int \mathrm{d}r_0\mathrm{d}r_1 u_{L'}(r_0;\,k')\,\varphi_\alpha(r_1)v_\lambda(r_0,\,r_1)u_L(r_0;\,k)\varphi_\gamma(r_1)\Bigg].
\end{aligned} \tag{C.15}$$

Here the target states of H_2 are represented by the form of equation (59).

The exchange matrix element that includes the solution to non-uniqueness is given by

$$\begin{aligned}
&\langle k'L'M'(\mathbf{x}_0),\, n'm'\pi's'(\mathbf{x}_1,\mathbf{x}_2):\, \mathcal{M}'\Pi'\mathcal{S}'|V^{\text{Exch}}|\, kLM(\mathbf{x}_0),\, nm\pi s(\mathbf{x}_1,\mathbf{x}_2):\, \mathcal{M}\Pi\mathcal{S}\rangle \\
&= \delta_{\mathcal{M}',\mathcal{M}}\delta_{\Pi',\Pi}\delta_{\mathcal{S}',\mathcal{S}}\sum_{\alpha\beta\gamma\delta} C^{(n')}_{\alpha,\beta}C^{(n)}_{\gamma,\delta}\Bigg\{\hat{s}'\hat{s}(-1)^{s'+s+1}\begin{Bmatrix}1/2 & 1/2 & s'\\ 1/2 & \mathcal{S} & s\end{Bmatrix} \\
&\quad\times\langle k'L'M'(\boldsymbol{r}_0),\, \phi_\alpha(\boldsymbol{r}_1)\phi_\beta(\boldsymbol{r}_2)(m'\pi')|2(E(1-\theta\Delta)-H)|\,\phi_\gamma(\boldsymbol{r}_0),\, kLM(\boldsymbol{r}_1)\phi_\delta(\boldsymbol{r}_2)(m\pi)\rangle \\
&\quad - \delta_{s',s}\langle k'L'M'(\boldsymbol{r}_0),\, \phi_\alpha(\boldsymbol{r}_1)\phi_\beta(\boldsymbol{r}_2)(m'\pi')|2E\theta I_0^N\Delta|\, kLM(\boldsymbol{r}_0),\, \phi_\gamma(\boldsymbol{r}_1)\phi_\delta(\boldsymbol{r}_2)(m\pi)\rangle\Bigg\} \\
&= 2\delta_{\mathcal{M}',\mathcal{M}}\delta_{\Pi',\Pi}\delta_{\mathcal{S}',\mathcal{S}}\sum_{\alpha\beta\gamma\delta} C^{(n')}_{\alpha,\beta}C^{(n)}_{\gamma,\delta}\Bigg\{\hat{s}'\hat{s}(-1)^{s'+s+1}\begin{Bmatrix}1/2 & 1/2 & s'\\ 1/2 & \mathcal{S} & s\end{Bmatrix}[(E(1-\theta\Delta) - \varepsilon_k - \varepsilon_{k'} - 1/R)\langle k'L'M'|\phi_\gamma\rangle \\
&\quad\times\langle\phi_\alpha|kLM\rangle\langle\phi_\beta|\phi_\delta\rangle - \langle k'L'M'|V_0 - U_0|\phi_\gamma\rangle\langle\phi_\alpha|kLM\rangle\langle\phi_\beta|\phi_\delta\rangle - \langle k'L'M'|\phi_\gamma\rangle\langle\phi_\alpha|V_1 - U_1|kLM\rangle\langle\phi_\beta|\phi_\delta\rangle \\
&\quad - \langle k'L'M'|\phi_\gamma\rangle\langle\phi_\alpha|kLM\rangle\langle\phi_\beta|H_2|\phi_\delta\rangle - \langle k'L'M',\, \phi_\alpha|V_{01}|\phi_\gamma,\, kLM\rangle\langle\phi_\beta|\phi_\delta\rangle - \langle k'L'M',\, \phi_\beta|V_{02}|\phi_\gamma,\, \phi_\delta\rangle\langle\phi_\alpha|kLM\rangle \\
&\quad - \langle\phi_\alpha,\, \phi_\beta|V_{12}|kLM,\, \phi_\delta\rangle\langle k'L'M'|\phi_\gamma\rangle] - \delta_{s',s}\langle\phi_\alpha|\phi_\gamma\rangle\langle\phi_\beta|\phi_\delta\rangle E\theta\Delta\langle k'L'M'|I_0^N|kLM\rangle\Bigg\}.
\end{aligned} \tag{C.16}$$

The one-electron matrix elements $\langle\phi|kLM\rangle$, $\langle\phi|V - U|kLM\rangle$, and $\langle\phi_{n'}|\phi_n\rangle$ have similar forms to the matrix elements given in (C.9), (C.10) and (B.8) respectively. $\langle\phi_{n'}|H_i^{\text{Elec}}|\phi_n\rangle$ terms are evaluated in appendix B. The electron–electron terms can be evaluated in a similar fashion to the direct matrix element electron–electron term, which is given in the last term of equation (C.15).

The logical operator Δ is used to solve the non-uniqueness problem. To do this we need to identify the space where the projectile and two target electrons are spanned by the same set of one-electron orbitals. In order to identify this space we separate the set of two-electron configurations in to two categories. The first category is the configurations that represent both target electrons in a symmetric manner $(n'l'm', nlm)$ with $n, n' \leqslant \tilde{n}$, where in the present e^-–H_2 structure model $n, n' \leqslant 2$ (as described in section 9.1). The second category is for frozen-core type configurations $(n'l'm', n_cl_cm_c)$, where $(n'l'm')$ span all possible one-electron functions while $(n_cl_cm_c)$ span only a few low lying orbitals. Note that in the present structure model $n_c = 1$. The Δ operator is applied, i.e. $\Delta = 1$ if: $|\varphi_\delta\rangle$ is a core orbital $(n_cl_cm_c)$, or when $|\varphi_\delta\rangle$ forms a symmetric configuration and $|\varphi_\alpha\rangle$ is either a core orbital or forms a symmetric configuration. If these conditions are not satisfied $\Delta = 0$.

Appendix D. Useful definitions

The following definitions have been taken from Varshalovich *et al* [59] unless explicitly stated. In some

explicitly noted cases, additional definitions are derived. These definitions assume integer value quantum numbers.

Spherical harmonics

The spherical harmonics have the following properties

$$Y_{lm}(\pm\pi n,\,\phi) = (-1)^{nl}\sqrt{\frac{(2l+1)}{4\pi}}\,\delta_{m,0}, \tag{D.1}$$

$$Y^*_{lm}(\Omega) = (-1)^m Y_{l-m}(\Omega), \tag{D.2}$$

$$\sum_{m=-l}^{l} Y_{lm}(\Omega)\,Y^*_{lm}(\Omega) = \frac{(2l+1)}{4\pi}, \tag{D.3}$$

$$Y_{l_1m_1}(\Omega)\,Y_{l_2m_2}(\Omega) = \sum_{l_3m_3}\frac{\hat{l}_1\hat{l}_2}{\sqrt{4\pi}\,\hat{l}_3} \times C^{l_30}_{l_10,l_20}C^{l_3m_3}_{l_1m_1,l_2m_2}\,Y_{l_3m_3}(\Omega), \tag{D.4}$$

where $\hat{l} = \sqrt{2l+1}$ and $C^{lm}_{l_1m_1,l_2m_2}$ denotes Clebsch–Gordan coefficients. From the above definition, the following is also true

$$Y_{l_1m_1}(\Omega)\,Y_{l_2-m_1}(\Omega) = \sum_{l_3}\frac{\hat{l}_1\hat{l}_2}{4\pi} \times C^{l_30}_{l_10,l_20}C^{l_30}_{l_1m_1,l_2-m_1}P_{l_3}(\cos(\theta)). \tag{D.5}$$

The Legendre orthogonality property, assuming $0 \leqslant m \leqslant j$

$$\int_0^\pi P^m_j(\cos(\theta))P^m_{j'}(\cos(\theta))\sin(\theta)\mathrm{d}\theta = \frac{2(j+m)!}{(2j+1)(j-m)!}\delta_{j,j'}. \tag{D.6}$$

The spherical harmonics satisfy the closure property

$$\sum_{lm}Y_{lm}(\hat{r}_1)\,Y_{lm}(\hat{r}_2) = \delta(\phi_1-\phi_2)\,\delta(\cos(\theta_1)-\cos(\theta_2)) = \delta(\hat{\boldsymbol{r}}_1-\hat{\boldsymbol{r}}_2). \tag{D.7}$$

The following is used to integrate over spherical harmonics analytically

$$\begin{aligned}
&\sqrt{\frac{4\pi}{2l_2+1}}\,\langle Y_{l_1m_1}|Y_{l_2m_2}|Y_{l_3m_3}\rangle_{\hat{\boldsymbol{r}}} \\
&= (-1)^{m_1}\hat{l}_1\hat{l}_3\begin{pmatrix} l_1 & l_2 & l_3\\ 0 & 0 & 0\end{pmatrix}\begin{pmatrix} l_1 & l_2 & l_3\\ -m_1 & m_2 & m_3\end{pmatrix} \\
&= (-1)^{m_1}\hat{l}_1\hat{l}_3\begin{pmatrix} l_1 & l_2 & l_3\\ 0 & 0 & 0\end{pmatrix} \\
&\quad\times\left[(-1)^{l_1+l_2+l_3}\begin{pmatrix} l_3 & l_2 & l_1\\ m_3 & m_2 & -m_1\end{pmatrix}\right] \\
&= (-1)^{m_1+l_1+l_2+l_3}\hat{l}_1\hat{l}_3\left(\frac{(-1)^{3l_1+l_2}}{\hat{l}_3}C^{l_30}_{l_10,l_20}\right) \\
&\quad\times\left(\frac{(-1)^{3l_3+l_2-m_1}}{\hat{l}_1}C^{l_1m_1}_{l_3m_3,l_2m_2}\right) \\
&= (-1)^{l_2}C^{l_30}_{l_10,l_20}C^{l_1m_1}_{l_3m_3,l_2m_2},
\end{aligned} \tag{D.8}$$

where $\begin{pmatrix} l_1 & l_2 & l_3\\ m_1 & m_2 & m_3\end{pmatrix}$ are the Wigner 3-*j* symbols and we have assumed integer quantum numbers in the last step. In this derivation definitions (D.2), (D.21) and (D.23) are utilised.

Wigner-D functions

The Wigner-D functions satisfy the following properties

$$D^J_{m_1,m_1'}(\boldsymbol{\beta}) = (-1)^{m_1'-m_1}D^{J*}_{-m_1,-m_1'}(\boldsymbol{\beta}). \tag{D.9}$$

$$D^{J_1}_{m_1,m_1'}(\boldsymbol{\beta})D^{J_2}_{m_2,m_2'}(\boldsymbol{\beta}) = \sum_{J=|J_1-J_2|}^{J_1+J_2}C^{Jm_1+m_2}_{J_1m_1,J_2m_2}\,C^{Jm_1'+m_2'}_{J_1m_1',J_2m_2'} \times D^J_{m_1+m_2,m_1'+m_2'}(\boldsymbol{\beta}). \tag{D.10}$$

The above definition implies

$$D^{J*}_{m_1,m_1'}(\boldsymbol{\beta}) = (-1)^{m_1'-m_1}D^J_{-m_1,-m_1'}(\boldsymbol{\beta}). \tag{D.11}$$

Definition (D.10) can be transformed with (D.9) and (D.11) to obtain

$$D^{J_1*}_{m_1,m_1'}(\boldsymbol{\beta})D^{J_2}_{m_2,m_2'}(\boldsymbol{\beta}) = (-1)^{m_2'-m_2}\sum_{J=|J_1-J_2|}^{J_1+J_2}C^{J-m_1+m_2}_{J_1-m_1,J_2m_2}\,C^{J-m_1'+m_2'}_{J_1-m_1',J_2m_2'}D^{J*}_{m_1-m_2,m_1'-m_2'}(\boldsymbol{\beta}), \tag{D.12}$$

$$D^{J_1*}_{m_1,m_1'}(\boldsymbol{\beta})D^{J_2*}_{m_2,m_2'}(\boldsymbol{\beta}) = (-1)^{m_1'-m_1+m_2'-m_2}\sum_{J=|J_1-J_2|}^{J_1+J_2}C^{J-m_1-m_2}_{J_1-m_1,J_2-m_2}\,C^{J-m_1'-m_2'}_{J_1-m_1',J_2-m_2'}D^J_{-m_1-m_2,-m_1'-m_2'}(\boldsymbol{\beta}). \tag{D.13}$$

From Varshalovich *et al* [59] we have the definition

$$\int_0^{2\pi}\int_0^{\pi}\int_0^{2\pi}D^{J'*}_{m_1',m_2'}(\alpha,\,\beta,\,\gamma)D^J_{m_1,m_2}(\alpha,\,\beta,\,\gamma)\mathrm{d}\alpha\sin(\beta)\mathrm{d}\beta\mathrm{d}\gamma = \frac{8\pi^2}{(2J+1)}\delta_{J',J}\,\delta_{m_1',m_1}\,\delta_{m_2',m_2}, \tag{D.14}$$

which is derived explicitly in Zare [170]. Utilising the same steps taken in Zare [170], it can be shown that

$$\delta_{m_2',m_2}\int_0^{2\pi}\int_0^{\pi}D^{J'*}_{m_1',m_2'}(\alpha,\,\beta,\,0)D^J_{m_1,m_2}(\alpha,\,\beta,\,0)\mathrm{d}\alpha\sin(\beta)\mathrm{d}\beta = \frac{4\pi}{(2J+1)}\delta_{J',J}\,\delta_{m_1',m_1}\,\delta_{m_2',m_2}. \tag{D.15}$$

Clebsch–Gordan coefficients and Wigner 3-j symbols

$$C^{l_3m_3}_{l_1m_1,l_2m_2} = (-1)^{l_1+l_2-l_3}C^{l_3-m_3}_{l_1-m_1,l_2-m_2} \tag{D.16}$$

$$= (-1)^{l_1+l_2-l_3}C^{l_3m_3}_{l_2m_2,l_1m_1}, \tag{D.17}$$

$$C^{l_3m_3}_{l_1m_1,l_2m_2} = (-1)^{l_1-m_1}\frac{\hat{l}_3}{\hat{l}_2}C^{l_2-m_2}_{l_1m_1,l_3-m_3}. \tag{D.18}$$

The Wigner 3-*j* symbol has the following properties and can be related to the Clebsch–Gordan coefficients such that

$$\begin{pmatrix} l_1 & l_2 & l_3\\ m_1 & m_2 & m_3\end{pmatrix} = (-1)^{l_1+l_2+l_3} \times\begin{pmatrix} l_1 & l_2 & l_3\\ -m_1 & -m_2 & -m_3\end{pmatrix} \tag{D.19}$$

$$= (-1)^{l_1+l_2+l_3}\begin{pmatrix} l_2 & l_1 & l_3 \\ m_2 & m_1 & m_3 \end{pmatrix} \tag{D.20}$$

$$= (-1)^{l_1+l_2+l_3}\begin{pmatrix} l_3 & l_2 & l_1 \\ m_3 & m_2 & m_1 \end{pmatrix} \tag{D.21}$$

$$= \frac{(-1)^{l_3+m_3+2l_1}}{\hat{l}_3} C^{l_3 m_3}_{l_1-m_1,l_2-m_2}. \tag{D.22}$$

Substituting (D.16) into (D.22)

$$\begin{pmatrix} l_1 & l_2 & l_3 \\ m_1 & m_2 & m_3 \end{pmatrix} = \frac{(-1)^{3l_1+l_2+m_3}}{\hat{l}_3} C^{l_3-m_3}_{l_1 m_1,l_2 m_2}. \tag{D.23}$$

The Clebsch–Gordan coefficients have the orthogonality conditions

$$\sum_{m_1 m_2} C^{l_3 m_3}_{l_1 m_1,l_2 m_2} C^{l_3' m_3'}_{l_1 m_1,l_2 m_2} = \delta_{l_3,l_3'}\delta_{m_3,m_3'}, \tag{D.24}$$

$$\sum_{m_1 m_3} C^{l_3 m_3}_{l_1 m_1,l_2 m_2} C^{l_3 m_3}_{l_1 m_1,l_2' m_2'} = \frac{(2l_3+1)}{(2l_2+1)}\delta_{l_2,l_2'}\delta_{m_2,m_2'}, \tag{D.25}$$

$$\sum_{l_3 m_3} C^{l_3 m_3}_{l_1 m_1,l_2 m_2} C^{l_3 m_3}_{l_1 m_1',l_2 m_2'} = \sum_{l_3} C^{l_3 m_1+m_2}_{l_1 m_1,l_2 m_2} C^{l_3 m_1'+m_2'}_{l_1 m_1',l_2 m_2'} = \delta_{m_1,m_1'}\delta_{m_2,m_2'}. \tag{D.26}$$

Evaluating select Clebsch–Gordan coefficients

$$C^{00}_{l_1 m_1,l_2 m_2} = \frac{(-1)^{l_1-m_1}}{\hat{l}_1}\delta_{l_1,l_2}\delta_{m_2,-m_1} \tag{D.27}$$

$$C^{l_3 m_3}_{l_1 m_1,00} = \delta_{l_1,l_3}\delta_{m_1,m_3}, \tag{D.28}$$

$$C^{l_3 m_3}_{00,l_2 m_2} = \delta_{l_2,l_3}\delta_{m_2,m_3}. \tag{D.29}$$

References

[1] Janev R K 2001 *At. Plasma–Mater. Interact. Data Fusion* **9** 1
[2] Matt S, Fiegele T, Senn G, Becker K, Deutsch H, Echt O, Stamatovic A, Scheier P and Märk T D 2001 *At. Plasma–Mater. Interact. Data Fusion* **9** 11
[3] Celiberto R, Capitelli M and Laricchiuta A 2002 *Phys. Scr.* **2002** 32
[4] Janev R, Reiter D and Samm U 2003 http://eirene.de/reports/report_4105.pdf
[5] Meyer J *et al* 2012 *Phys. Rev. Lett.* **108** 196102
[6] Lu Q-B 2010 *Phys. Rep.* **487** 141
[7] Fox J L, Galand M I and Johnson R E 2008 *Space Sci. Rev.* **139** 3
[8] Huestis D L, Bougher S W, Fox J L, Galand M, Johnson R E, Moses J I and Pickering J C 2008 *Space Sci. Rev.* **139** 63
[9] Bougher S W, Blelly P-L, Combi M, Fox J L, Mueller-Wodarg I, Ridley A and Roble R G 2008 *Space Sci. Rev.* **139** 107
[10] Inokuti M and Berger M J 1987 *Nucl. Instrum. Methods* B **27** 249
[11] Inokuti M, Dillon M A and Kimura M 1987 *Int. J. Quantum Chem.* **32** 251
[12] Berger M J and Paul L 1995 *Atomic and Molecular Data For Radiotherapy And Radiation Research* (Vienna: IAEA) ch 7
[13] Sanche L 2005 *Eur. Phys. J.* D **35** 367
[14] Boudaïffa B, Cloutier P, Hunting D, Huels M A and Sanche L 2000 *Science* **287** 1658
[15] Baccarelli I, Bald I, Gianturco F A, Illenberger E and Kopyra J 2011 *Phys. Rep.* **508** 1
[16] White R *et al* 2014 *Appl. Radiat. Isotopes* **83, Part B** 77
[17] Boyle G J, Tattersall W J, Cocks D G, Dujko S and White R D 2015 *Phys. Rev.* A **91** 052710
[18] Schulz G J 1973 *Rev. Mod. Phys.* **45** 423
[19] Stroe M and Fifirig M 2009 *J. Phys. B: At. Mol. Opt. Phys.* **42** 205203
[20] Tennyson J 2010 *Phys. Rep.* **491** 29
[21] Gao J, Peacher J L and Madison D H 2005 *J. Chem. Phys.* **123** 204302
[22] Madison D H and Al-Hagan O 2010 *J. At. Mol. Opt. Phys.* **2010** 367180
[23] Zecca A, Chiari L, García G, Blanco F, Trainotti E and Brunger M J 2010 *J. Phys. B: At. Mol. Opt. Phys.* **43** 215204
[24] Sanz A G, Fuss M C, Blanco F, Sebastianelli F, Gianturco F A and García G 2012 *J. Chem. Phys.* **137** 124103
[25] Fuss M C, Sanz A G, Blanco F, Limão Vieira P, Brunger M J and García G 2014 *Eur. Phys. J.* D **68** 161
[26] Kim Y-K 2001 *Phys. Rev.* A **64** 032713
[27] Kim Y-K 2007 *J. Chem. Phys.* **126** 064305
[28] Kim Y-K and Rudd M E 1994 *Phys. Rev.* A **50** 3954
[29] Kim Y-K 2002 *Phys. Rev.* A **65** 022705
[30] Kim Y-K, Irikura K K and Ali M A 2000 *J. Res. Natl Inst. Stand. Technol.* **105** 285
[31] Itikawa Y and Mason N 2005 *Phys. Rep.* **414** 1
[32] Mazevet S, Morrison M A, Boydstun O and Nesbet R K 1999 *J. Phys. B: At. Mol. Opt. Phys.* **32** 1269
[33] Morrison M, Crompton R, Saha B and Petrovic Z 1987 *Aust. J. Phys.* **40** 239
[34] Morrison M A and Sun W 1995 *Computational Methods for Electron–Molecule Collisions* ed W M Huo and F A Gianturco (New York: Plenum) pp 131–90
[35] Lane N F 1980 *Rev. Mod. Phys.* **52** 29
[36] Florescu-Mitchell A and Mitchell J 2006 *Phys. Rep.* **430** 277
[37] Stibbe D T and Tennyson J 1997 *Phys. Rev. Lett.* **79** 4116
[38] Trevisan C S and Tennyson J 2001 *J. Phys. B: At. Mol. Opt. Phys.* **34** 2935
[39] Takatsuka K and McKoy V 1984 *Phys. Rev.* A **30** 1734
[40] Rescigno T N, McCurdy C W, Orel A E and Lengsfield III B H 1995 *Computational Methods for Electron–Molecule Collisions* ed W M Huo and F A Gianturco (New York: Plenum) pp 1–44
[41] Pindzola M S *et al* 2007 *J. Phys. B: At. Mol. Opt. Phys.* **40** R39
[42] Zammit M C, Fursa D V and Bray I 2014 *Phys. Rev.* A **90** 022711
[43] Bray I, Fursa D V, Kheifets A S and Stelbovics A T 2002 *J. Phys. B: At. Mol. Opt. Phys.* **35** R117
[44] Bray I, Fursa D V, Kadyrov A S, Stelbovics A T, Kheifets A S and Mukhamedzhanov A M 2012 *Phys. Rep.* **520** 135
[45] Chung H-K, Braams B J, Bartschat K, Császár A G, Drake G W F, Kirchner T, Kokoouline V and Tennyson J 2016 *J. Phys. D: Appl. Phys.* **49** 363002
[46] da Costa R F, da Paixão F J and Lima M A P 2005 *J. Phys. B: At. Mol. Opt. Phys.* **38** 4363
[47] da Costa R F and Lima M A P 2007 *Phys. Rev.* A **75** 022705
[48] Zammit M C, Savage J S, Fursa D V and Bray I 2017 *Phys. Rev.* A **95** 022708
[49] Zammit M C, Fursa D V, Savage J S, Bray I, Chiari L, Zecca A and Brunger M J 2017 *Phys. Rev.* A **95** 022707
[50] Zammit M C, Fursa D V and Bray I 2013 *Phys. Rev.* A **87** 020701
[51] Halmová G and Tennyson J 2008 *Phys. Rev. Lett.* **100** 213202

[52] Halmová G, Gorfinkiel J D and Tennyson J 2008 *J. Phys. B: At. Mol. Opt. Phys.* **41** 155201
[53] Gorfinkiel J D and Tennyson J 2005 *J. Phys. B: At. Mol. Opt. Phys.* **38** 1607
[54] Bray I and Stelbovics A T 1992 *Phys. Rev.* A **46** 6995
[55] Fursa D V and Bray I 1995 *Phys. Rev.* A **52** 1279
[56] Brown J M and Carrington A 2003 *Rotational Spectroscopy of Diatomic Molecules* (Cambridge: Cambridge University Press)
[57] Bishop D M and Cheung L M 1977 *Phys. Rev.* A **16** 640
[58] Itikawa Y 2000 *Theor. Chem. Acc.* **105** 123
[59] Varshalovich D A, Moskalev A N and Khersonskii V K 1988 *Quantum Theory of Angular Momentum* 1st edn (Philadelphia, PA: World Scientific)
[60] Gallup G A 1993 *J. Phys. B: At. Mol. Opt. Phys.* **26** 759
[61] Isaacs W A and Morrison M A 1996 *Phys. Rev.* A **53** 4215
[62] Feldt A N and Morrison M A 2008 *Phys. Rev.* A **77** 012726
[63] Zhang J-Y, Mitroy J and Varga K 2009 *Phys. Rev. Lett.* **103** 223202
[64] Zhang J Y and Mitroy J 2011 *Phys. Rev.* A **83** 022711
[65] Broad J T and Reinhardt W P 1976 *J. Phys. B: At. Mol. Phys.* **9** 1491
[66] Yamani H A and Fishman L 1975 *J. Math. Phys.* **16** 410
[67] Zammit M C, Savage J S, Fursa D V and Bray I 2016 *Phys. Rev. Lett.* **116** 233201
[68] Wolniewicz L and Poll J 1978 *J. Mol. Spectrosc.* **72** 264
[69] Kolos W, Szalewicz K and Monkhorst H J 1986 *J. Chem. Phys.* **84** 3278
[70] Wünderlich D and Fantz U 2011 *At. Data Nucl. Data Tables* **97** 152
[71] Kolos W and Wolniewicz L 1968 *J. Chem. Phys.* **49** 404
[72] Bray I 2013 *Computational Quantum Mechanics Lecture Notes,* ch 7 (Perth: Curtin University)
[73] Bray I 1994 *Phys. Rev.* A **49** 1066
[74] Bostock C J 2011 *J. Phys. B: At. Mol. Opt. Phys.* **44** 083001
[75] Bray A W, Abdurakhmanov I B, Kadyrov A S, Fursa D V and Bray I 2015 *Comput. Phys. Commun.* **196** 276
[76] Bray A W, Abdurakhmanov I B, Kadyrov A S, Fursa D V and Bray I 2016 *Comput. Phys. Commun.* **203** 147
[77] Bray A W, Abdurakhmanov I B, Kadyrov A S, Fursa D V and Bray I 2017 *Comput. Phys. Commun.* **212** 55
[78] Inokuti M 1971 *Rev. Mod. Phys.* **43** 297
[79] Bray I and Stelbovics A T 1995 *Adv. At. Mol. Phys.* **35** 209
[80] Zammit M C, Fursa D V and Bray I 2015 *J. Phys.: Conf. Ser.* **635** 012009
[81] Bray I, McCarthy I E, Wigley J and Stelbovics A T 1993 *J. Phys. B: At. Mol. Opt. Phys.* **26** L831
[82] Peart B, Walton D S and Dolder K T 1969 *J. Phys. B: At. Mol. Phys.* **2** 1347
[83] Dance D F, Harrison M F A, Rundel R D and Smith A C H 1967 *Proc. Phys. Soc.* **92** 577
[84] Dunn G H and Van Zyl B 1967 *Phys. Rev.* **154** 40
[85] Peek J M 1974 *Phys. Rev.* A **10** 539
[86] Fifirig M and Stroe M 2011 *J. Phys. B: At. Mol. Opt. Phys.* **44** 085202
[87] Pindzola M S, Robicheaux F and Colgan J 2005 *J. Phys. B: At. Mol. Opt. Phys.* **38** L285
[88] von Busch F and Dunn G H 1972 *Phys. Rev.* A **5** 1726
[89] Zammit M C, Fursa D V and Bray I 2013 *Phys. Rev.* A **88** 062709
[90] Pitchford L C *et al* 2016 *Plasma Process. Polym.* **14** 1600098
[91] Peart B and Dolder K T 1971 *J. Phys. B: At. Mol. Phys.* **4** 1496
[92] Ghazaly M O A E, Jureta J, Urbain X and Defrance P 2004 *J. Phys. B: At. Mol. Opt. Phys.* **37** 2467
[93] Dunn G H, Van Zyl B and Zare R N 1965 *Phys. Rev. Lett.* **15** 610
[94] Peart B and Dolder K T 1972 *J. Phys. B: At. Mol. Phys.* **5** 1554
[95] Peart B and Dolder K T 1972 *J. Phys. B: At. Mol. Phys.* **5** 860
[96] Peart B and Dolder K T 1973 *J. Phys. B: At. Mol. Phys.* **6** 2409
[97] Bahati E M, Jureta J J, Belic D S, Cherkani-Hassani H, Abdellahi M O and Defrance P 2001 *J. Phys. B: At. Mol. Opt. Phys.* **34** 2963
[98] Chapman F M 1975 *J. Chem. Phys.* **63** 2101
[99] Andersen L H, Johnson P J, Kella D, Pedersen H B and Vejby-Christensen L 1997 *Phys. Rev.* A **55** 2799
[100] Duca M and Fifirig M 2010 *Cent. Eur. J. Phys.* **8** 87
[101] Kadyrov A S and Bray I 2002 *Phys. Rev.* A **66** 012710
[102] Utamuratov R, Kadyrov A S, Fursa D V, Bray I and Stelbovics A T 2010 *J. Phys. B: At. Mol. Opt. Phys.* **43** 125203
[103] Hewitt N R, Noble C J and Bransden B H 1990 *J. Phys. B: At. Mol. Opt. Phys.* **23** 4185
[104] Hewitt N R, Noble C J and Bransden B H 1992 *J. Phys. B: At. Mol. Opt. Phys.* **25** 557
[105] Higgins K and Burke P G 1991 *J. Phys. B: At. Mol. Opt. Phys.* **24** L343
[106] Mitroy J 1993 *Aust. J. Phys.* **46** 751
[107] Walters H R J, Kernoghan A A, McAlinden M T and Campbell C P 1997 *Photon and Electron Collisions with Atoms and Molecules* ed P G Burke and C J Joachain (New York: Plenum) pp 313–45
[108] Lugovskoy A V, Kadyrov A S, Bray I and Stelbovics A T 2010 *Phys. Rev.* A **82** 062708
[109] Utamuratov R, Kadyrov A S, Fursa D V, Zammit M C and Bray I 2015 *Phys. Rev.* A **92** 032707
[110] Kadyrov A S and Bray I 2016 *J. Phys. B: At. Mol. Opt. Phys.* **49** 222002
[111] Biswas P K, Germano J S E and Frederico T 2002 *J. Phys. B: At. Mol. Opt. Phys.* **35** L409
[112] Bray I, Bailey J J, Fursa D V, Kadyrov A S and Utamuratov R 2016 *Eur. Phys. J.* D **70** 1
[113] Kolos W and Wolniewicz L 1967 *J. Chem. Phys.* **46** 1426
[114] Liu J W and Hagstrom S 1993 *Phys. Rev.* A **48** 166
[115] Wolniewicz L and Dressler K 1988 *J. Chem. Phys.* **88** 3861
[116] Wolniewicz L and Dressler K 1994 *J. Chem. Phys.* **100** 444
[117] Wolniewicz L 1995 *J. Mol. Spectrosc.* **174** 132
[118] Wolniewicz L 1995 *J. Mol. Spectrosc.* **169** 329
[119] Wolniewiczi L Wolniewiczi molecular hydrogen database http://fizyka.umk.pl/ftp/pub/publications/ifiz/luwo/
[120] Machacek J R, Anderson E K, Makochekanwa C, Buckman S J and Sullivan J P 2013 *Phys. Rev.* A **88** 042715
[121] Karwasz G P, Pliszka D and Brusa R S 2006 *Nucl. Instrum. Methods* B **247** 68
[122] Zecca A, Chiari L, Sarkar A, Nixon K L and Brunger M J 2009 *Phys. Rev.* A **80** 032702
[123] Hoffman K R, Dababneh M S, Hsieh Y F, Kauppila W E, Pol V, Smart J H and Stein T S 1982 *Phys. Rev.* A **25** 1393
[124] Charlton M, Griffith T C, Heyland G R and Wright G L 1980 *J. Phys. B: At. Mol. Phys.* **13** L353
[125] Zhou S, Li H, Kauppila W E, Kwan C K and Stein T S 1997 *Phys. Rev.* A **55** 361
[126] Deuring A, Floeder K, Fromme D, Raith W, Schwab A, Sinapius G, Zitzewitz P W and Krug J 1983 *J. Phys. B: At. Mol. Phys.* **16** 1633
[127] Fedus K, Franz J and Karwasz G P 2015 *Phys. Rev.* A **91** 062701
[128] Fromme D, Kruse G, Raith W and Sinapius G 1988 *J. Phys. B: At. Mol. Opt. Phys.* **21** L261
[129] Moxom J, Laricchia G and Charlton M 1993 *J. Phys. B: At. Mol. Opt. Phys.* **26** L367
[130] Jacobsen F M, Frandsen N P, Knudsen H and Mikkelsen U 1995 *J. Phys. B: At. Mol. Opt. Phys.* **28** 4675

[131] Knudsen H, Brun-Nielsen L, Charlton M and Poulsen M R 1990 *J. Phys. B: At. Mol. Opt. Phys.* **23** 3955
[132] Sullivan J P, Marler J P, Gilbert S J, Buckman S J and Surko C M 2001 *Phys. Rev. Lett.* **87** 073201
[133] Sullivan J P, Gilbert S J, Marler J P, Barnes L D, Buckman S J and Surko C M 2002 *Nucl. Instrum. Methods* B **192** 3
[134] Lino J L S, Germano J S E and Lima M A P 1994 *J. Phys. B: At. Mol. Opt. Phys.* **27** 1881
[135] Arretche F and Lima M A P 2006 *Phys. Rev.* A **74** 042713
[136] Wolniewicz L and Staszewska G 2003 *J. Mol. Spectrosc.* **217** 181
[137] Ferch J, Raith W and Schroder K 1980 *J. Phys. B: At. Mol. Phys.* **13** 1481
[138] van Wingerden B, Wagenaar R W and de Heer F J 1980 *J. Phys. B: At. Mol. Phys.* **13** 3481
[139] Jones R K 1985 *Phys. Rev.* A **31** 2898
[140] Subramanian K P and Kumar V 1989 *J. Phys. B: At. Mol. Opt. Phys.* **22** 2387
[141] Nickel J C, Kanik I, Trajmar S and Imre K 1992 *J. Phys. B: At. Mol. Opt. Phys.* **25** 2427
[142] Shyn T W and Sharp W E 1981 *Phys. Rev.* A **24** 1734
[143] Nishimura H, Danjo A and Sugahara H 1985 *J. Phys. Soc. Japan* **54** 1757
[144] Khakoo M A and Trajmar S 1986 *Phys. Rev.* A **34** 138
[145] Srivastava S K, Chutjian A and Trajmar S 1975 *J. Chem. Phys.* **63** 2659
[146] Muse J, Silva H, Lopes M C A and Khakoo M A 2008 *J. Phys. B: At. Mol. Opt. Phys.* **41** 095203
[147] Morrison M, Feldt A and Saha B 1984 private communication
[148] Furst J, Mahgerefteh M and Golden D E 1984 *Phys. Rev.* A **30** 2256
[149] Linder F and Schmidt H 1971 *Z. Naturforsch.* **26A** 1603
[150] Krishnakumar E and Srivastava S K 1994 *J. Phys. B: At. Mol. Opt. Phys.* **27** L251
[151] Straub H C, Renault P, Lindsay B G, Smith K A and Stebbings R F 1996 *Phys. Rev.* A **54** 2146
[152] Rapp D and Englander-Golden P 1965 *J. Chem. Phys.* **43** 1464
[153] Lindsay B G and Mangan M A 2003 *Photon and Electron Interactions with Atoms, Molecules and Ions* (*Numerical Data And Functional Relationships In Science And Technology: New Series*) vol 7 (Berlin: Springer)
[154] Pindzola M S, Robicheaux F, Loch S D and Colgan J P 2006 *Phys. Rev.* A **73** 052706
[155] Branchett S E, Tennyson J and Morgan L A 1991 *J. Phys. B: At. Mol. Opt. Phys.* **24** 3479
[156] Khakoo M A and Trajmar S 1986 *Phys. Rev.* A **34** 146
[157] Srivastava S K and Jensen S 1977 *J. Phys. B: At. Mol. Phys.* **10** 3341
[158] Wrkich J, Mathews D, Kanik I, Trajmar S and Khakoo M A 2002 *J. Phys. B: At. Mol. Opt. Phys.* **35** 4695
[159] Kato H, Kawahara H, Hoshino M, Tanaka H, Campbell L and Brunger M J 2008 *Phys. Rev.* A **77** 062708
[160] Borges I and Bielschowsky C E 1999 *Phys. Rev.* A **60** 1226
[161] Brunger M J and Buckman S J 2002 *Phys. Rep.* **357** 215
[162] Bray A W, Abdurakhmanov I B, Kadyrov A S, Fursa D V and Bray I 2016 *Comput. Phys. Commun.* **203** 147–51
[163] Moccia R 1964 *J. Chem. Phys.* **40** 2164
[164] Moccia R 1964 *J. Chem. Phys.* **40** 2176
[165] Moccia R 1964 *J. Chem. Phys.* **40** 2186
[166] Chung H-K and Braams B J 2013 https://amdis.iaea.org/publications/INDC/INDC_NDS-636.pdf
[167] Celiberto R, Janev R, Laricchiuta A, Capitelli M, Wadehra J and Atems D 2001 *At. Data Nucl. Data Tables* **77** 161
[168] Sullivan J P, Jones A, Caradonna P, Makochekanwa C and Buckman S J 2008 *Rev. Sci. Instrum* **79** 113105
[169] Fursa D V and Bray I 2012 *New J. Phys.* **14** 035002
[170] Zare R N 1988 *Angular Momentum* (New York: Wiley)